Alma Mater Studiorum · Università di Bologna

Scuola di Scienze
Dipartimento di Fisica e Astronomia
Corso di Laurea Magistrale in Fisica

Prospects for the Higgs boson self-coupling measurement with the Phase-II CMS detector upgrade using simulated pp collisions at $\sqrt{s} = 27$ TeV (High Energy LHC)

Relatore:

Prof.ssa Sylvie Braibant

Correlatore:

Dott.ssa Lisa Borgonovi

Presentata da:

Devis Comandini

Sessione I
Anno Accademico 2018/2019

Sommario

Le performance dell'analisi del canale HH$\rightarrow$ b$\bar{\text{b}}$ZZ(4ℓ) ($\ell = e$, μ) sono presentate considerando il possibile upgrade ad alta energia dell'acceleratore LHC, il cosiddetto High Energy LHC, a un'energia nel centro di massa di 27 TeV e con una luminosità integrata di 15000 fb^{-1}; è inoltre presentato un confronto con lo stesso studio effettuato nel contesto di High Luminosity LHC, a un'energia nel centro di massa di 14 TeV e con una luminosità integrata di 3000 fb^{-1}. In entrambi gli scenari si considera il rivelatore CMS dopo la Fase-II dell'upgrade previsto per il 2024. L'analisi si basa interamente su simulazioni Monte Carlo: la generazione a livello partonico del segnale e dei fondi è effettuata con MadGraph5_aMC@NLO, mentre *parton showering* e adronizzazione sono ottenute con Pythia8; la risposta del rivelatore è infine ottenuta con il software di simulazione parametrizzata Delphes. Viene stimato un limite al 95% CL sulla *signal strength* della coppia di bosoni di Higgs pari a $r = 1.45$ nel canale inclusivo $b\bar{b}4\ell$, con una significanza del segnale corrispondente di $1.43\,\sigma$. Viene anche presentato uno studio sulle prospettive per la misura della costante di auto-accoppiamento dell'Higgs (λ_3): l'intervallo di confidenza al 95% CL stimato per $\kappa_\lambda = \lambda_3/\lambda_3^{\mathrm{SM}}$ è pari a [-0.7,7.2].

Abstract

The performance of the HH→ b$\bar{\text{b}}$ZZ(4ℓ) ($\ell = e$, μ) analysis is presented considering the possible High Energy upgrade of the LHC collider, at a center-of-mass energy of 27 TeV and with an integrated luminosity of 15000 fb^{-1}; a comparison of the results with the same study performed in the context of the High Luminosity LHC, at a center-of-mass energy of 14 TeV and with an integrated luminosity of 3000 fb^{-1}, is also reported. The Phase-II upgraded CMS detector, expected in 2024, is assumed in both the scenarios. The analysis is fully based on Monte Carlo simulations: the parton-level generation of signal and backgrounds is performed with MadGraph5_aMC@NLO, while parton showering and hadronization are achieved with Pythia8; the detector response is then obtained in the parametric framework provided by Delphes. A limit on the di-Higgs signal strength of $r = 1.45$ is estimated at 95% CL in the inclusive $b\bar{b}4\ell$ channel, with a corresponding signal significance of $1.43\,\sigma$. A study on the prospects for the measurements of the Higgs self-coupling (λ_3) is also performed: the projected confidence interval on $\kappa_\lambda = \lambda_3/\lambda_3^{\text{SM}}$ is found to be [-0.7,7.2] at the 95% CL.

Contents

Introduction

The discovery of the Higgs boson announced by the ATLAS and CMS experiments at the Large Hadron Collider (LHC) in 2012 was a fundamental experimental confirmation of the Brout-Englert-Higgs (BEH) mechanism. Since then, one of the main goals of the LHC experiments was to focus on precise measurements of the Higgs boson properties in order to investigate the Standard Model (SM) predictions. The discovery of the Higgs boson, however, was only the first step in the study of the ElectroWeak Symmetry Breaking (EWSB) sector, including searches for Beyond Standard Model (BSM) effects.

In order to more deeply study SM predictions as well as to explore the possibility of new physics BSM, an upgrade of the LHC accelerator is planned for the next decade; a setup capable of working in different and more challenging experimental conditions will be achieved.

In particular, a new LHC regime, working at a center-of-mass energy of $\sqrt{s} = 14$ TeV and istantaneous luminosity $\mathcal{L} = 5 \times 10^{34}$ cm^{-2}s^{-1}, the so-called High Luminosity LHC (HL-LHC), is scheduled to start from 2026. Moreover, another LHC possible upgrade is under study, the so-called High Energy LHC (HE-LHC), which could follow the HL-LHC era. The accelerating system will provide proton-proton collisions at a center-of-mass energy of $\sqrt{s} = 27$ TeV, increasing the potential of direct observation of new particles and allowing a deeper study of the Higgs potential.

In order to cope with these new experimental conditions, a two-phase upgrade of the CMS detector is planned: the Phase-I upgrade, ongoing until 2020, and the Phase-II, scheduled to start in 2024.

The production of a pair of Higgs bosons (HH) is an exclusive probe to study the BEH potential as well as to look for deviations from the SM predictions since it gives experimental acces to the Higgs boson self-coupling (λ_3). However, due to the small cross section, searches of HH productions based on current Run 2 data are not sensitive to SM HH productions; instead, with HL-LHC and HE-LHC, the integrated luminosity and production cross sections will increase providing the opportunity to study the HH production.

My research is focused on the HH→ $b\bar{b}ZZ(4\ell)$ ($\ell = e, \mu$) channel, considering the HE-LHC scenario and the CMS Phase-II detector. This channel provides a clear final state composed of two b-tagged jets associated with two pairs of opposite charge and same flavour leptons.

The aim of this study is to give a measurement of the sensitivity to the HH production in this particular channel. Furthermore, prospects for the measurement of the HH self coupling are studied, in order to compute the projected confidence interval on the coupling.

The analysis performed in this thesis is based on Monte Carlo simulations of SM signal, the main backgrounds, and the BSM samples using MadGraph5_aMC@NLO for event generation, Pythia8 for parton shower and hadronization, and the Delphes software to parametrize the CMS detector response in the HE-LHC configuration.

In Chapter 1 the theory of the SM is introduced, focusing on the electroweak sector and the Higgs mechanism. A brief discussion of the Higgs discovery is also presented, followed by an introduction to the di-Higgs theory.

In Chapter 2 the LHC accelerator and CMS detector are described; the HE-LHC and HL-LHC scenarios are also illustrated, including the CMS upgrades needed.

In Chapter 3 the software used for the data simulations are described.

In Chapter 4 the analysis of the HH→ $b\bar{b}ZZ(4\ell)$ ($\ell = e, \mu,$) channel performed with the Phase-II CMS detector configuration in the HE-LHC scenario is described, including a comparison of the perfomance between the HE-LHC and the HL-LHC scenarios.

Chapter 1

Standard Model and Higgs mechanism

The Standard Model of particles and forces (SM) [1–3] is a Quantum Field Theory (QFT) used in particle physics in order to classify particles as well as to describe the fundamental interactions in the subnuclear domain. It has been theorized since the second half of the 20th century and, over the years, it became a well-tested theory thanks to many experimental results. In the SM, three of the four fundamental forces are described: the electromagnetic, the weak and the strong interactions, not including gravitation which gives neglecting contributions. Moreover, matter is described to be made of *elementary particles* which interact exchanging force mediators.

1.1 Elementary particle and interactions

An elementary particle is commonly considered as the *ultimate constituent* of matter; more precisely, it can be defined as a physical system with no substructure, up to the present experimental limit of $\lambda \simeq \mathcal{O}(10^{-19})$ cm. According to the SM, matter is made of *fermions*: twelve particles (and their respective antiparticles) with spin $\frac{1}{2}$ following the Fermi-Dirac statistics.

Fermions are splitted into two groups, *leptons* and *quarks*, each divided in three generations (or families). Leptons are classified into three isospin doublets: the upper component carries a negative unite of charge (so it is sensitive to electromagnetic and weak interactions) whereas the lower component is represented by the associated neutrino (which is sensitive to the weak force only):

$$\begin{pmatrix} e \\ \nu_e \end{pmatrix} \quad \begin{pmatrix} \mu \\ \nu_\mu \end{pmatrix} \quad \begin{pmatrix} \tau \\ \nu_\tau \end{pmatrix}$$

Quarks are similarly grouped in three weak isospin doublets:

$$\begin{pmatrix} u \\ d \end{pmatrix} \quad \begin{pmatrix} c \\ s \end{pmatrix} \quad \begin{pmatrix} t \\ b \end{pmatrix}$$

The upper component (quark *up (u), charm (c) and top (t)*) carries an elecric charge $q = +\frac{2}{3}e$ whereas the lower one (quark *down (d), strange (s), and bottom (b)*) is negatively charged with value $q = -\frac{1}{3}e$. Besides being sensitive to electromagnetic and weak interaction, quarks are the only elementary particles subjected to the strong interaction: they have an additional quantum number with respect to leptons, the *colour* charge, with three possible values, identified as *red (R), green (G), blue (B).*

A fundamental difference between leptons and quarks is that quarks cannot be observed as free particles: they are confined in composite particles called *hadrons*, which have no colour charge and can be divided in two categories:

- *mesons*, a pair of quark and antiquark, with integer spin;

- *baryons (antibaryons)*, composed of three quarks (antiquarks), with half-integer spin.

To complete the description we need to introduce the fundamental forces: *electromagnetic, weak, strong and gravitational* interactions. According to QFT, each interaction involves matter particles (that is, fermions) obeying the Fermi-Dirac statistic, and interaction particles, called *bosons* with integer spin and obeying the Bose-Einstein statistics. The *photon* (γ) mediates the electromagnetic interaction, $W^{\pm}$ and Z^0 bosons are the mediators of the weak interaction, eight *gluons* (g) mediate the strong interaction. For the sake of completeness, the gravitational interaction is supposed to be mediated by a particle called *graviton* (G); however, the SM does not describe this force due to the negligible effect of gravitational interaction in the particle physics realm.

The other fundamental concept of the SM is symmetry. Using Steven Weinberg's words:

> *At the deepest level, all we find are symmetries and responses to symmetries.*

A symmetry is a property of a system which is preserved under some transformation. *Noether's theorem* links this mathematical feature with the concept of *conservation*: a continuous invariance of the Lagrangian which describes a system implies the existence of a conserved quantity.

In the realm of QFT a deeper link between symmetry and the understanding of Nature arises; the requirement of *gauge invariance* of the Lagrangian under a continuous group of local transformations as suggested by C. N. Yang and R. Mills [4], needs the introduction of N gauge fields (with $N = d^2 - 1$ where d represents the dimension of the group) interacting with particle fields.

Each interaction can be introduced defining a particular symmetry group; the SM is therefore described by the composition:

$$\mathrm{SU}(3)_C \otimes \Big[\mathrm{SU}(2)_L \otimes \mathrm{U}(1)_Y\Big]$$

where

- $\mathrm{SU}(3)_C$ describes the strong interaction between quarks. C stands for *colour*, the charge generating the interaction, and 3 denotes the number of its possible values;

- $\mathrm{SU}(2)_L$ is the symmetry associated to the weak interaction. L stands for *Left* because this interaction applies only to left-handed fermions;

- $\mathrm{U}(1)_Y$ governs electrodynamics. Y stands for *hypercharge* and it is related to the electric charge Q and the third component of the weak isospin I_3 by the Gell-Mann and Nishijima relation:

$$Q = I_3 + \frac{Y}{2} \tag{1.1}$$

1.2 The electroweak theory and the Higgs mechanism

Using local gauge invariance as a guiding principle, Glashow firstly proposed the idea of a unified electroweak theory, based on the symmetry group $\mathrm{SU}(2)_L \otimes \mathrm{U}(1)_Y$ [5]. Considering a fermion field described by the Dirac spinor ψ, the corresponding Lagrangian density $\mathcal{L}$ for the free particle is given by:

$$\mathcal{L} = \bar{\psi}(x)(i\gamma^\mu \partial_\mu - m)\psi(x) \tag{1.2}$$

The local gauge invariance requirement implies the substitution of the partial derivative ∂_μ with a gauge covariant derivative $\mathcal{D}_\mu$ of the $\mathrm{SU}(2)_L \otimes \mathrm{U}(1)_Y$ symmetry group:

$$\mathcal{D}_\mu = \partial_\mu + \frac{ig'}{2} B_\mu \mathbb{1} + \frac{ig}{2} \vec{W}^a_\mu \sigma_a \tag{1.3}$$

where:

- g and $\frac{g'}{2}$ correspond to the coupling of the $\mathrm{SU}(2)_L$ and $\mathrm{U}(1)_Y$ group respectively;
- σ_a are the three Pauli matrices;
- B_μ represents the massles mediator of the $\mathrm{U}(1)_Y$ group;
- W^a_μ are the three mediators associated with the $\mathrm{SU}(2)_L$ group.

The Lagrangian thus becomes:

$$\mathcal{L} = \bar{\psi}(x)(i\gamma^\mu \mathcal{D}_\mu - m)\psi(x) \tag{1.4}$$

and now it is invariant under a local transformation of the $\mathrm{SU}(2)_L \otimes \mathrm{U}(1)_Y$ group:

$$\mathcal{L}'(\psi') = \mathcal{L}(\psi) \tag{1.5}$$

To complete the description of the system, we have to include terms describing the propagation of gauge fields with the Yang-Mills Lagrangian density:

$$\mathcal{L}_{\mathrm{YM}} = -\frac{1}{4} B_{\mu\nu} B^{\mu\nu} - \frac{1}{4} W^a_{\mu\nu} W^{\mu\nu\, a} \tag{1.6}$$

where:

$$B_{\mu\nu} = \partial_\mu B_\nu - \partial_\nu B_\mu \tag{1.7}$$

$$W^a_{\mu\nu} = \partial_\mu W^a_\nu - \partial_\nu W^a_\mu + g\epsilon_{abc} W^b_\mu W^c_\nu \tag{1.8}$$

with the additional term $g\epsilon_{abc} W^b_\mu W^c_\nu$ due to the *non abelian* nature of the SU(2)$_L$ group.

In the Lagrangian density there are no quadratic terms for gauge fields: particles associated with them are then *massless.* In order to obtain the real fields γ, W$^\pm$, and Z^0 we need to introduce the *Spontaneous Symmetry Breaking* (SSB) and the Brout-Englert-Higgs-Guralnik-Hagen-Kibble mechanism (BEH).

1.2.1 Spontaneous Symmetry Breaking

The starting point to include a mass term for gauge bosons is the concept of Spontaneous Symmetry Breaking (SSB): given a Lagrangian density $\mathcal{L}$ of fields ϕ and a group trasformation U, we say we have SSB if:

- $\mathcal{L}$ is invariant under the transformation, that is $\mathcal{L} \xrightarrow{U} \mathcal{L}' = \mathcal{L}$;
- the *vacuum* of the theory $\langle\phi\rangle_0$ (that is, the state of minimum energy, also called ground state) is not invariant under the same trasformation, $\langle\phi\rangle_0 \xrightarrow{U} \langle\phi\rangle_0' \neq \langle\phi\rangle_0$.

The SSB of any continuous global symmetry implies the introduction of massless particles, the so-called Nambu-Goldstone bosons (from Y. Nambu, who discovered them in his supeconductivity studies [6], and J. Goldstone, who applied Nambu's discovery in QFT [7]). In particular, Goldstone's theorem states that the number of scalar massless particles is equal to the number of generators of the symmetry that are *broken*, that is that do not preserve the ground state.

The mechanism responsible for the masses of weak gauge bosons and elementary fermions, the BEH-mechanism, was independently proposed in 1964 by F. Englert and R. Brout [8], G. Guralnik [9], P. Higgs [10], C. R. Hagen and T. Kibble [11, 12]. Considering the SSB of a local symmetry, the Goldstone bosons combine with the gauge bosons; as a consequence, a number of bosons equal to the Goldstone bosons become massive. In

1967-1968, recovering Glashow's idea, S. Weinberg and A. Salam [13, 14] theorized the electroweak unification based on the SU(2)$_L\otimes$ U(1)$_Y$ group symmetry.

1.2.2 Higgs mechanism in the SU(2)$_L\otimes$ U(1)$_Y$ theory

The key point of the BEH-mechanism is the introduction of a new scalar boson, the Higgs boson, and the corresponding Higgs field, which is supposed to permeate all space-time. The masses of the boson and fermion fields are then caused by their interaction with the Higgs boson.

The Lagrangian of the electroweak theory is composed of four terms:

$$\mathcal{L}_{\text{SM}} = \mathcal{L}_{\text{YM}} + \mathcal{L}_{\text{f}} + \mathcal{L}_{\text{Higgs}} + \mathcal{L}_{\text{Yuk}} \tag{1.9}$$

The gauge term is the same as (1.6), while the fermion term is given by:

$$\mathcal{L}_{\text{f}} = \bar{\Psi}_L i\gamma^\mu \mathcal{D}_\mu \Psi_L + \bar{\Psi}_R i\gamma^\mu \mathcal{D}_\mu \Psi_R \tag{1.10}$$

where Ψ_L and Ψ_R are the left and right chiral projection of Ψ,

$$\Psi_{\text{L (R)}} = \frac{1 \mp \gamma_5}{2}\Psi \tag{1.11}$$

The gauge invariant derivatives acting on Ψ_L and Ψ_R are:

$$\mathcal{D}_\mu \Psi_L = (\partial_\mu + i\frac{g}{2}W^a_\mu \sigma_q + i\frac{g'}{2}B_\mu \mathbb{1})\Psi_L \qquad \mathcal{D}_\mu \Psi_R = (\partial_\mu + i\frac{g'}{2}B_\mu \mathbb{1})\Psi_R \tag{1.12}$$

To introduce the Higgs term of the Lagrangian we have to consider the complex doublet (with $I = \frac{1}{2}$ and $Y = +1$):

$$\phi = \begin{pmatrix} \phi^+ \\ \phi^0 \end{pmatrix} \tag{1.13}$$

where ϕ^+ and ϕ^0 are the complex scalar fields:

$$\phi^+ = \frac{1}{\sqrt{2}}(\phi_1 + i\phi_2) \qquad \phi^0 = \frac{1}{\sqrt{2}}(\phi_3 + i\phi_4) \tag{1.14}$$

The corresponding Lagrangian term is given by:

$$\mathcal{L}_{\text{Higgs}} = (\mathcal{D}^{\mu}\phi)^{\dagger}(\mathcal{D}_{\mu}\phi) - V(\phi^{\dagger}\phi) \tag{1.15}$$

where:

$$\mathcal{D}_{\mu} = \partial_{\mu} + i\frac{g}{2}W_{\mu}^{a}\sigma_{a} + i\frac{g'}{2}B_{\mu}\mathbb{1} \tag{1.16}$$

and:

$$V(\phi^{\dagger}\phi) = \mu^{2}\phi^{\dagger}\phi + \lambda(\phi^{\dagger}\phi)^{2} \tag{1.17}$$

μ^2 and λ being complex constants.
We can distinguish two different cases based on the sign of μ^2:

- if $\mu^2 > 0$, the potential is described by a parabolic shape with a unique minimum: there is no SSB and the symmetry is preserved even by the vacuum;

- if $\mu^2 = -|\mu^2| < 0$, the potential is described by the so-called “Mexican Hat” shape, shown in Figure 1.1. The potential does not have a unique minimum and the ground state ($\phi = 0$) corresponds to a local maximum of the potential. The system is invariant under global transformations but is no longer invariant under local transformations: this is the case that gives spontaneous symmetry breaking.

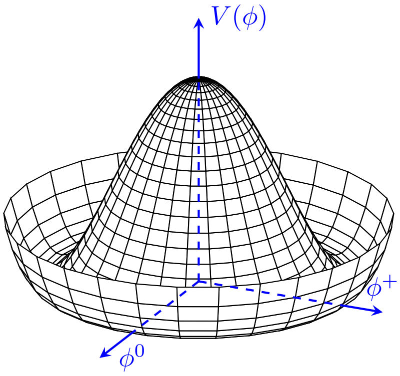

Figure 1.1: Mexican Hat potential $V(\phi)$ when $\mu^2 < 0$.

Minimizing the potential (1.17) we find that there is an infinte number of degenerate states with minimum energy satisfing the condition:

$$\phi^\dagger\phi = \frac{v^2}{2} \tag{1.18}$$

where $v = \sqrt{\frac{-\mu^2}{\lambda}}$ is the vacuum expectation value (VEV) of the Higgs field, that can be estimated from the Fermi constant G_F (from the muon lifetime), giving a value $v \approx 246$ GeV.

Therefore we can arbitrarily choose $\phi_1 = \phi_2 = \phi_3 = 0$ and $\phi_4 = \sqrt{\frac{-\mu^2}{2\lambda}}$, in order to have:

$$\phi_0 = \frac{1}{\sqrt{2}}\begin{pmatrix}0\\ v\end{pmatrix} \tag{1.19}$$

With this choice, the SU$(2)_L\otimes$ U$(1)_Y$ symmetry is broken: this means that ϕ_0 is not invariant under the group transformation. In particular, all the generators of the electroweak group are broken but their linear combination corresponding to the electric charge operator Q (given by (1.1)), is not. This means that under the subgroup U$(1)_{\text{EM}}$, the vacuum is invariant; for this reason the photon remains massless whereas the three mediators of the weak interaction become massive.

After choosing a value for the minimum, we have to expand the theory around the ground state introducing four real fields: an appropriate choice is to parametrize the expansion as:

$$\phi(x) = \frac{e^{\frac{i\vec{\xi}(x)\cdot\vec{\sigma}}{v}}}{\sqrt{2}}\begin{pmatrix}0\\ v+h(x)\end{pmatrix} \tag{1.20}$$

where the fields $\vec{\xi}(x)$ are the massless Goldstone bosons. They can be eliminated rotating the Higgs doublet in the *unitary* gauge, that is:

$$\phi(x) \to \phi'(x) = e^{\frac{-i\vec{\xi}(x)\cdot\vec{\sigma}}{v}}\phi(x) = \frac{1}{\sqrt{2}}\begin{pmatrix}0\\ v+h(x)\end{pmatrix} \tag{1.21}$$

This means that Goldstone bosons are not particles with a physical meaning; on the other hand, there is no chance to delete the field $h(x)$, which is so interpreted as a real particle, the Higgs boson.

We can now introduce the expression for the scalar field ϕ in the Lagrangian (1.15), obtaining (considering only second order terms for gauge bosons):

$$\begin{aligned}\mathcal{L}_{\text{Higgs}} = \frac{1}{2}(\partial_\mu h)(\partial^\mu h) + \frac{1}{2}(-2\mu^2)h^2 + \frac{1}{2}\left(\frac{g^2v^2}{4}\right)(W^1_\mu W^{1\mu} + W^2_\mu W^{2\mu}) \\ + \frac{1}{8}v^2(gW^3_\mu - g'B_\mu)(gW^3_\mu - g'B_\mu) + \mathit{const} + \mathit{higher\ order\ terms}\end{aligned} \tag{1.22}$$

where we can see that W^3_μ and B_μ appear in mixed products: they cannot be treated as physical particles, but we have to consider two orthogonal combinations of them:

$$\mathcal{Z}_\mu = \cos\theta_W W^3_\mu - \sin\theta_W B_\mu \tag{1.23}$$

$$\mathcal{A}_\mu = \sin\theta_W W^3_\mu + \cos\theta_W B_\mu \tag{1.24}$$

where θ_W is the Weinberg angle, that is the mixing angle chosen such as the mixed products of $\mathcal{Z}_\mu$ and $\mathcal{A}_\mu$ disappear:

$$\tan\theta_W = \frac{g'}{g} \tag{1.25}$$

In this way, $\mathcal{Z}_\mu$ and $\mathcal{A}_\mu$ represent the real bosons Z^0 and γ respectively. Using this definition, we can now rewrite the term $\mathcal{L}_{\text{YM}} + \mathcal{L}_{\text{Higgs}}$ as:

$$\begin{aligned}\mathcal{L}_{\text{YM}} + \mathcal{L}_{\text{Higgs}} = {} & \frac{1}{2}(\partial_\mu h)(\partial^\mu h) - \frac{1}{2}(-2\mu^2)h^2 \\ & - \frac{1}{4}W^1_{\mu\nu}W^{1\mu\nu} + \frac{1}{2}\left(\frac{g^2v^2}{4}\right)W^1_\mu W^{1\mu} \\ & - \frac{1}{4}W^2_{\mu\nu}W^{2\mu\nu} + \frac{1}{2}\left(\frac{g^2v^2}{4}\right)W^2_\mu W^{2\mu} \\ & - \frac{1}{4}Z_{\mu\nu}Z^{\mu\nu} + \frac{1}{2}\left(\frac{g^2v^2}{4\cos^2\theta_W}\right)\mathcal{Z}_\mu\mathcal{Z}^\mu \\ & - \frac{1}{4}B_{\mu\nu}B^{\mu\nu} + 0 \cdot \mathcal{A}_\mu\mathcal{A}^\mu \\ & + \frac{g^2v}{4}hW^1_\mu W^{1\mu} + \frac{g^2v}{4}hW^2_\mu W^{2\mu} + \frac{g^2v}{4\cos^2\theta_W}h\mathcal{Z}_\mu\mathcal{Z}^\mu\end{aligned} \tag{1.26}$$

To obtain the physical charged fields of the weak interaction, we have to consider the linear combinations:

$$W^-_\mu = \frac{1}{\sqrt{2}}(W^1_\mu + iW^2_\mu) \qquad W^+_\mu = \frac{1}{\sqrt{2}}(W^1_\mu - iW^2_\mu) \tag{1.27}$$

Replacing these definitions in the Lagrangian (1.26), we can identify:

- a mass term for the $W^\pm$ bosons (which correspond to the gauge fields W^1_μ and W^2_μ), given by $m^2_W = \frac{g^2v^2}{4}$;
- a mass term for the Z^0 boson (which corresponds to $\mathcal{Z}_\mu$), given by $m^2_Z = \frac{g^2v^2}{4\cos\theta_W}$;
- no mass term for the photon ($\mathcal{A}_\mu$), $m^2_\gamma = 0$;
- a mass term for the Higgs boson (associated to h^2), given by $m_H = \sqrt{-2\mu^2} = \sqrt{2\lambda}v$
- no coupling term between the Higgs boson and the photon;
- a coupling term between Higgs boson and massive weak bosons, given by $g_{\mathrm{WWH}} = \frac{2m^2_W}{v}$ and $g_{\mathrm{ZZH}} = \frac{m^2_Z}{v}$; the coupling between the Higgs boson and vector bosons is then proportional to the square of their masses.

Introducing a SU(2) doublet ϕ and considering a potential with a SSB, we managed to describe a theory which is gauge invariant for the SU$(2)_L\otimes$ U$(1)_Y$ symmetry group and includes the physical massive gauge bosons for the weak interaction.

To complete the description of (1.26), we need to describe the Yukawa term. In the SM, in fact, also fermion masses are caused by their interaction with the Higgs field. We then have:

$$\mathcal{L}^i_{\mathrm{Yuk}} = -g_{si}\phi\bar{\Psi}_i\Psi_i = -g_{si}\frac{v}{\sqrt{2}}\bar{\Psi}_i\Psi_i - \frac{g_{si}}{\sqrt{2}}h\bar{\Psi}_i\Psi_i \tag{1.28}$$

where we have expanded the theory around the ground state (1.19), i runs over all types of fermions and g_{si} are coupling constants with values chosen to obtain the *real* physical masses of the fermions. In (1.28) we can then indentify:

- a mass term for the i-th fermion:

$$m_{f_i} = g_{si}\frac{v}{\sqrt{2}}; \tag{1.29}$$

- the coupling between the i-th fermion and the Higgs boson:

$$\frac{g_{si}}{\sqrt{2}} = \frac{m_{f_i}}{v}. \tag{1.30}$$

The couplings between Higgs boson and fermions are then proportional to their masses.

1.2.3 Higgs boson discovery at LHC

The theory described by (1.9) was tested in several experiments: firstly, in 1973, neutral weak current interactions were observed in the bubble chamber Gargamelle at CERN [15], proving the existence of the neutral weak gauge boson Z^0 (even if without observing the boson itself). A direct observation of the weak interaction mediator bosons, $W^{\pm}$ and Z^0, was obtained at the Sp$\bar{\text{p}}$S collider in 1983 [16–18] while at LEP [19] more precise measurements were performed, all in agreement with SM predictions. However, a direct observation of the Higgs boson was still missing: its discovery was one of the main motivation for the construction of the Large Hadron Collider (LHC). In 2012 two different experiments, A Toroidal LHC ApparatuS (ATLAS) [20] and Compact Muon Solenoid (CMS) [21], finally announced the discovery of the Higgs boson [22, 23].

Higgs boson production

The main processes contributing to the Higgs boson production in pp colliders are:

- *gluon-gluon fusion*, $gg \to H$, the dominant channel in the whole mass range explored in the LHC experiments (Figure 1.2a);
- *vector-boson fusion*, $qq \to qqH$, the second contribution to the Higgs production with a clear signature of two hadronic jets in the forward-backward directions close to the beam axis (Figure 1.2b);
- *Higgstrahlung*, $qq \to VH$ where $V = W^{\pm}/Z^0$ (Figure 1.2c);
- $gg \to t\bar{t}H$, the lowest contribution but with a clear signature; the decay of the top quark pair, in fact, is $t\bar{t} \to b\bar{b}W^+W^-$, thus two b jets are present in the final state

and the whole signature is based on the following W decay, $W \to l\nu$ or $W \to qq'$ (Figure 1.2d).

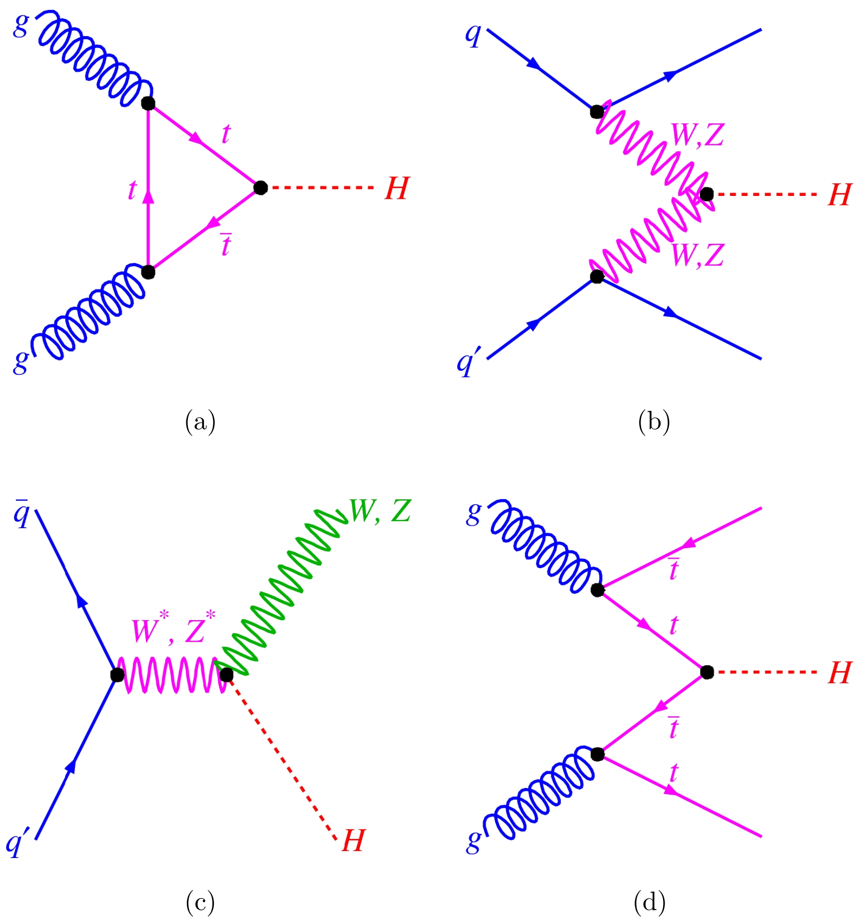

(a) (b) (c) (d)

Figure 1.2: Main production channels for the Higgs boson: (a) gluon-gluon fusion, (b) vector-boson fusion, (c) Higgstrahlung, (d) associated $t\bar{t}H$ [24].

As we have seen in the previous section, the SM predicts a mass for the Higgs boson given by:

$$m_H = \sqrt{-2\mu^2} = \sqrt{2\lambda}v \tag{1.31}$$

where λ is an external parameter: this means that the value of m_H is not predicted by the theory. The search for the Higgs boson was performed in the range 100 GeV $< m_H <$ 1 TeV. In Figure 1.3, the different production cross sections are shown as a function of the Higgs boson mass.

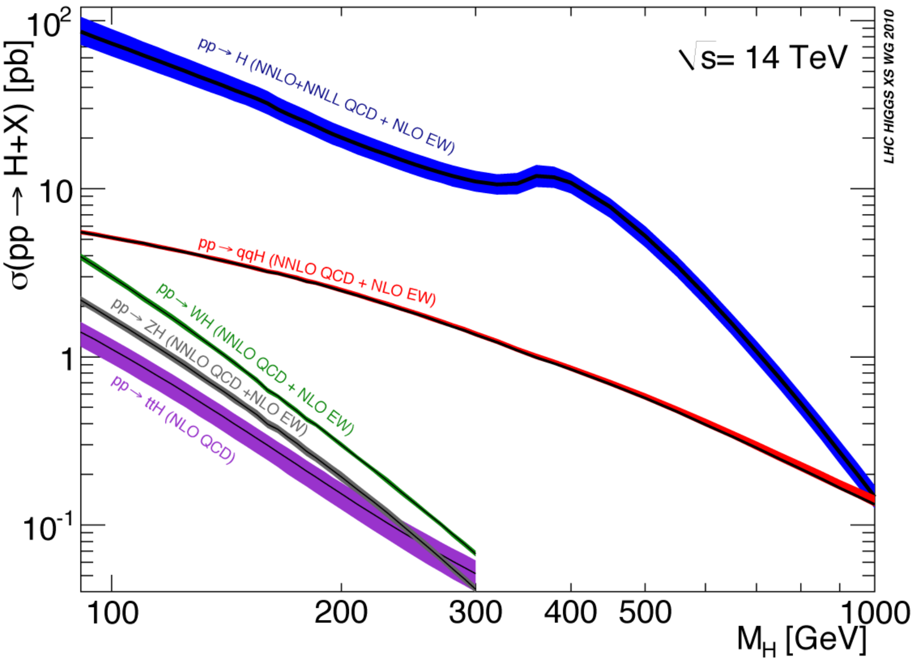

Figure 1.3: Higgs boson production cross section as a function of the Higgs mass at $\sqrt{s} = 14$ TeV [25].

Higgs boson decay modes

After being produced, the Higgs boson can decay in many different modes with different Branching Ratios (BR). The BR is defined as the ratio between the number of Higgs bosons decaying in a given channel with respect to the total number of decays (Figure 1.4a).

Taking into account both production and decay modes, we can estimate the sensitivity of a channel considering the product of the production section and the corresponding branching ratio, indicated by $\sigma \times BR$ and shown in Figure 1.4b.

Higgs boson discovery

Both LHC experiments, ATLAS and CMS, studied different Higgs decay channels in the region $110 \div 160$ GeV (the mass range was restricted by previous experiments [26–31]). Based on the analysis perfromed on data collected at a center-of-mass energy of $\sqrt{s} = 7$ TeV and $\sqrt{s} = 8$ TeV, on 4th of July 2012 both experiments announced the observation

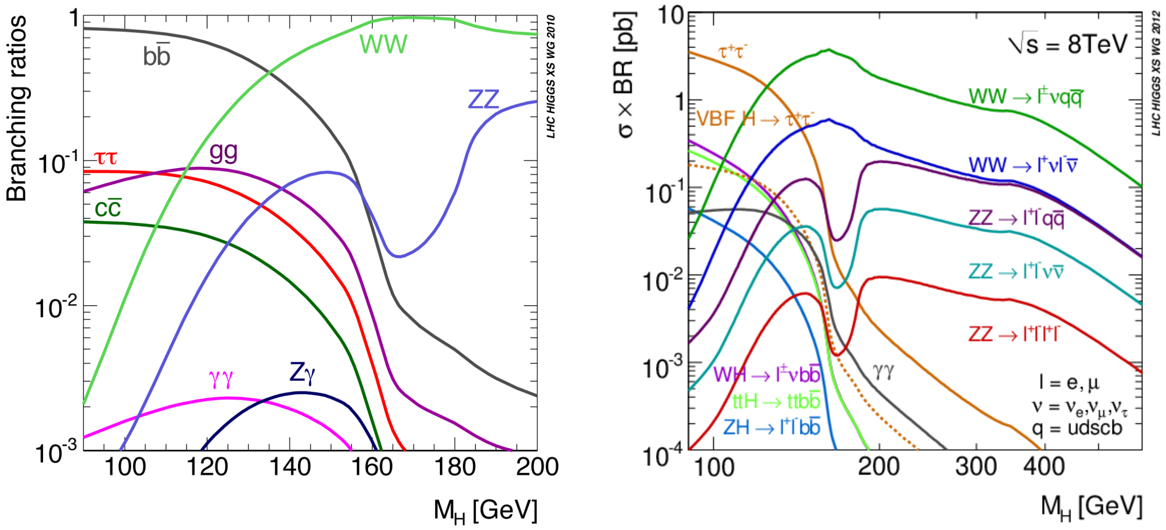

(a) (b)

Figure 1.4: Higgs boson decay branching ratios (a) and Higgs boson production cross sections times branching ratios (b) as a function of the Higgs mass at $\sqrt{s} = 8$ TeV [25].

of an excess of events at a mass near 125 GeV, with a local significance of $5.1\,\sigma$ (ATLAS) and $5.3\,\sigma$ (CMS): the Higgs boson was finally discovered.

The invariant mass distribution of a *di-photon* system produced by the decay $H \to \gamma\gamma$ and of a four-lepton system, emerging from the decay $H \to ZZ^* \to 4l$ are shown in Figure 1.5 and in Figure 1.6, for both ATLAS (a) and CMS (b) experiments.

In both decay channels, we can observe a clear signal peak over the background corresponding to a Higgs boson with a mass (considering the latest results at $\sqrt{s} = 13$ TeV):

$$\begin{aligned} m_H^{\text{ATLAS}} &= 124.86 \pm 0.27 \text{ GeV} \\ m_H^{\text{CMS}} &= 125.29 \pm 0.20\,(\text{stat.}) \pm 0.08\,(\text{sys.}) \text{ GeV}. \end{aligned}$$

The current world accepted value is [36]

$$m_H = 125.10 \pm 0.14 \text{ GeV} \tag{1.32}$$

and the combination of ATLAS and CMS results is shown in Figure 1.7

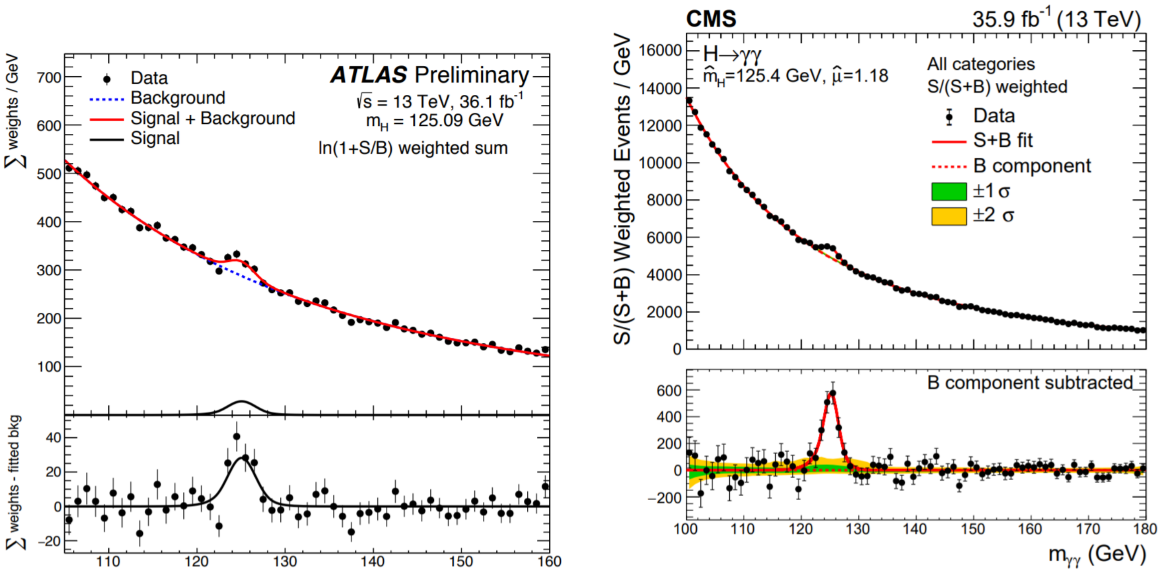

(a) (b)

Figure 1.5: ATLAS (a) and CMS (b) di-photon invariant mass distributions [32, 33].

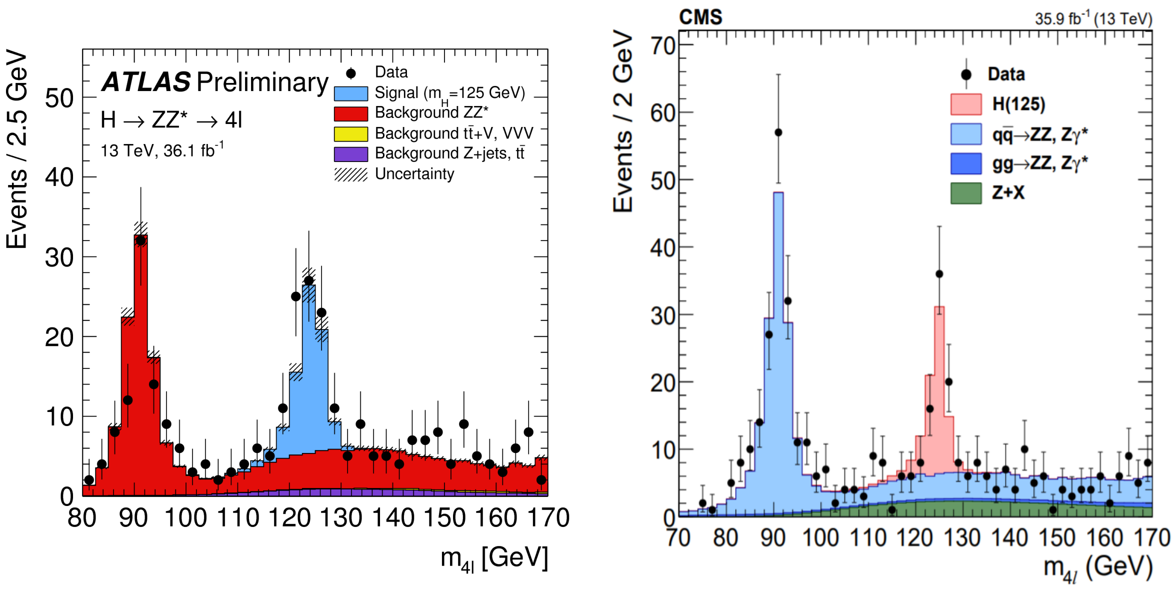

(a) (b)

Figure 1.6: ATLAS (a) and CMS (b) four-lepton invariant mass distributions [34, 35].

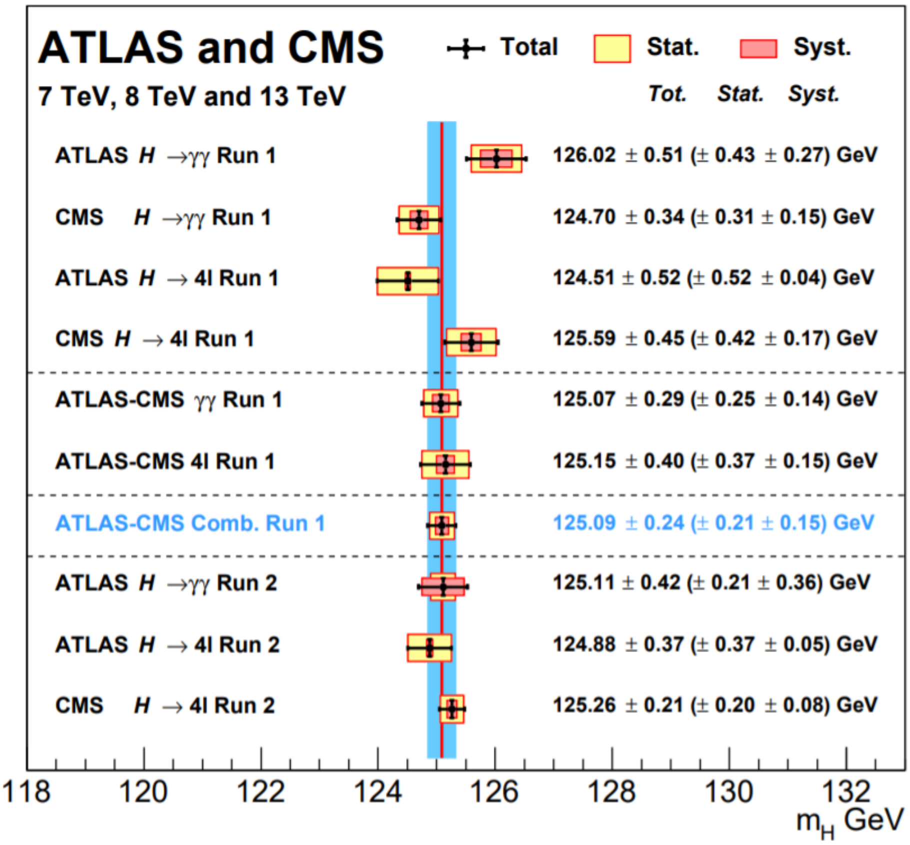

Figure 1.7: Summary of the CMS and ATLAS mass measurements [36].

1.3 Higgs boson pair production

Despite its importance, the discovery of the Higgs boson was only the first step in the study of the EWSB sector, including searches for BSM effects.

Considering the higher order and constant terms of (1.22),

$$\mathcal{L}_{\text{Higgs}} = (\dots) + \lambda v h^3 + \frac{\lambda}{4} h^4 - \frac{\lambda}{4} v^4 \tag{1.33}$$

the terms proportional to h^3 and h^4 represent the Higgs boson self-interaction via cubic and quartic vertices, respectively (while the constant term contributes to the vacuum energy).

Defining the two coupling constants as:

$$\lambda_3 = \lambda_4 = \lambda = \frac{m_H^2}{2v^2} \tag{1.34}$$

the Higgs potential $V(h)$ can be rewritten as:

$$V(h) = \frac{1}{2} m_H^2 h^2 + \lambda_3 v h^3 + \lambda_4 h^4 - \frac{\lambda}{4} v^4 \tag{1.35}$$

From the definition (1.34), the Higgs boson self-coupling is fully determined from m_H and v. The Higgs mass is experimentally known with good precision (1.32) while, as previously mentioned, v can be computed from the Fermi constant; within the SM predictions the value for the Higgs self-coupling λ_3 (also called *trilinear* coupling) is then:

$$\lambda_3 \approx 0.13 \tag{1.36}$$

The production of a pair of Higgs bosons (HH) is a unique and independent probe to test the SM predictions, since it allows a direct measurement of λ_3 (for the measurement of λ_4 a triple Higgs final state is necessary, and this process is very rare within the SM).

1.3.1 Production mechanisms

At the LHC the dominant HH production channel is the gluon-gluon fusion, $gg \to HH$, where two different top loops appear (Figure 1.8): the triangle diagram (a), which allows the direct extraction of λ_3, and the box diagram (b). They interfere destructively, causing

channel	$\sqrt{s} = 14$ (TeV)	$\sqrt{s} = 27$ (TeV)
ggHH	$36.69^{+2.1\%}_{-4.9\%} \pm 3.0\%$	$139.9^{+1.3\%}_{-3.9\%} \pm 2.5\%$
VBFHH	$1.95^{+1.1\%}_{-1.5\%} \pm 2.0\%$	$8.21^{+1.1\%}_{-0.7\%} \pm 1.8\%$
$\mathrm{t\bar{t}HH}$	$0.948^{+3.9\%}_{-13.5\%} \pm 3.2\%$	$5.27^{+2.0\%}_{-3.7\%} \pm 2.5\%$
WHH	$0.573^{+2.0\%}_{-1.4\%} \pm 1.9\%$	$1.48^{+2.3\%}_{-2.5\%} \pm 1.7\%$
ZHH	$0.359^{+1.9\%}_{-1.3\%} \pm 1.7\%$	$0.963^{+2.1\%}_{-2.3\%} \pm 1.5\%$
tjHH	$0.0383^{+5.2\%}_{-3.3\%} \pm 4.7\%$	$0.254^{+3.8\%}_{-2.8\%} \pm 3.6\%$

Table 1.1: HH production cross sections (in fb) [37].

the small production cross section values listed in Table 1.1 in both HE-LHC and HL-LHC scenarios (computed at Next-to-Next Leading Order) [37].

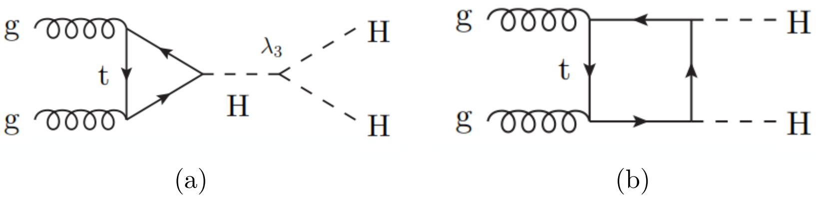

Figure 1.8: Gluon-gluon fusion di-Higgs production through triangle (a) and box (b) diagram.

Other di-Higgs production mechanisms are:

- vector-boson fusion (VBF HH), $qq' \to jjHH$;
- top pair associated production ($\mathrm{t\bar{t}HH}$), $qq'/gg \to t\bar{t}HH$;
- vector boson associated production (ZHH and WHH), $qq' \to VHH$;
- single top associated production (tjHH), $qq' \to tjHH$.

Feynman diagrams for these channels are shown in Figure 1.9.

In addition to SM predictions, in many BSM theories there are processes that can enhance the HH production rate, resulting in a larger σ_{HH}. In particular, some models [38–41] assume the existence of heavy resonances decaying in a Higgs pair; even if

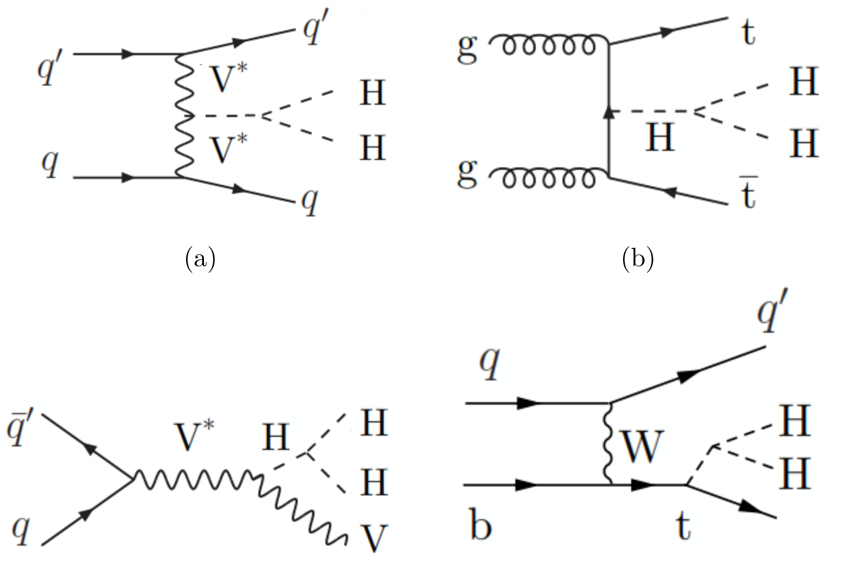

(a) (b) (c) (d)

Figure 1.9: Feynman diagram for the other di-Higgs production mechanisms: VBF (a), associated top pair (b), associated vector boson (c), and associated single top (d). Only diagrams involving the trilinear coupling are shown.

particles are too heavy to be observed with the accelerator energy, they can contribute to HH production via virtual processes.

In other non resonant models, instead, the Higgs boson couplings would be different from the SM ones; therefore, HH production through gluon-gluon fusion [42] and VBF [43] are modified.

The most general way to include BSM effects is writing the relevant Higgs Lagrangian $\mathcal{L}_{\mathrm{HH}}$ in the following form:

$$\mathcal{L}_{\mathrm{HH}} = \kappa_\lambda \lambda_3^{\mathrm{SM}} v h^3 - \frac{m_{\mathrm{t}}}{v}(\kappa_{\mathrm{t}} H + \frac{c_2}{v} h^2)(\bar{t}_{\mathrm{L}} t_{\mathrm{R}} + h.c.) + \frac{1}{4}\frac{\alpha_{\mathrm{s}}}{3\pi v}(c_{\mathrm{g}} h - \frac{c_{\mathrm{gg}}}{2v} h^2) G^{\mu\nu} G_{\mu\nu} \quad (1.37)$$

where:

- $\kappa_\lambda \equiv \lambda_3/\lambda_3^{\mathrm{SM}}$ is the self coupling modifier referred to the trilinear coupling ($\kappa_\lambda = 1$ in the SM);
- $\kappa_{\mathrm{t}} \equiv y_{\mathrm{t}}/y_{\mathrm{t}}^{\mathrm{SM}}$ takes into account a possible different top Yukawa coupling ($\kappa_{\mathrm{t}} = 1$

Benchmark point	κ_λ	κ_t	c_2	c_g	c_{gg}
1	7.5	1.0	−1.0	0.0	0.0
2	1.0	1.0	0.5	−0.8	0.6
3	1.0	1.0	−1.5	0.0	−0.8
4	−3.5	1.5	−3.0	0.0	0.0
5	1.0	1.0	0.0	0.8	−1.0
6	2.4	1.0	0.0	0.2	−0.2
7	5.0	1.0	0.0	0.2	−0.2
8	15.0	1.0	0.0	−1.0	1.0
9	1.0	1.0	1.0	−0.6	0.6
10	10.0	1.5	−1.0	0.0	0.0
11	2.4	1.0	0.0	1.0	−1.0
12	15.0	1.0	1.0	0.0	0.0
SM	1.0	1.0	0.0	0.0	0.0

Table 1.2: Values of the coupling parameters in different benchmarks [44].

in the SM);

- c_2, c_g, and c_{gg} include BSM interactions between two Higgs bosons and two top quarks, one Higgs boson and two gluons, two Higgs bosons and two gluons, respectively (with $c_i = 0$ in the SM).

In the BSM scenario, thus, there are five couplings which modify the di-Higgs production; moreover, the kinematics of the two Higgs bosons produced is strongly dependent on their values. With a statistical approach, regions with similar final state kinematics are identified in the parameters space; for each region, a benchmark model is selected as the most representative point. With the twelve benchmarks listed in Table 1.2 the phenomenology of the whole five-dimensional parameters space is represented. In this thesis, all the parameters have been fixed to their SM predicted values, with the exception of κ_λ, which is the subject of a part of this study.

Chapter 2

The Large Hadron Collider and CMS experiment

The Large Hadron Collider (LHC) [45–47], the biggest particle accelerator ever built, is installed at CERN (European Organization for Nuclear Research) [48] near Geneva. LHC is located in the 26.7 km long tunnel that was previously hosting the LEP (Large Electron-Positron) collider [19], about 100 m under the French-Swiss border close to Geneva. LHC accelerates and collides proton beams at an unprecedent center-of-mass energy (up to $\sqrt{s} = 14$ TeV) in order to be able to test the SM predictions to a high level of precision, as well as to search for physics BSM. The four main experiments that collect and analize data from the particle collisions provided by the LHC are:

- *A Large Ion Collider Exeperiment* (ALICE) [49], an experiment using $Pb - Pb$ dedicated collisions to study *quark-gluon-plasma*;

- *A Toroidal LHC ApparatuS* (ATLAS) [20] and *Compact Muon Solenoid* (CMS) [21], two general purpose experiments;

- *LHC beauty experiment* (LHCb) [50], specialized in studying quark-antiquark asimmetry.

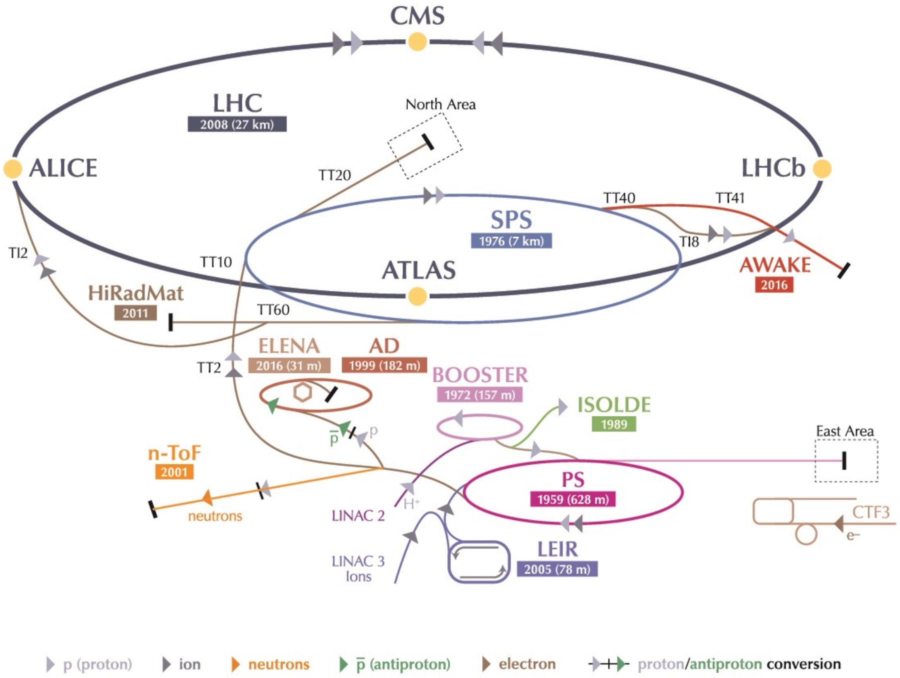

Figure 2.1: Schematic view of the LHC; pre-accelerators and main detectors [51].

2.1 LHC accelerating system

The LHC accelerating system consists of variuos steps (see Figure 2.1), going from the protons production to their acceleration in the LHC tunnel:

1. protons are producted through the ionisation of hydrogen atoms;
2. passing through a *linear accelerator* (LINAC), protons are accelerated up to 50 MeV;
3. after that, protons pass in the *Proton Syncrotron Booster* (PSB), from which they exit with an energy of 1.4 GeV;
4. then the *Proton Syncrotron* (PS) accelerates them up to 26 GeV;
5. in the last step before the injection in the LHC, protons are accelerated up to 450 GeV by the *Super Proton Synchrotron* (SPS).

After the injection, protons run into two separate and parallel beam pipes. The first challenge is to maintain particles in a circular trajectory: for this purpose, 1232 dipole magnets giving a 8.33 T magnetic field at a temperature of 1.9 K are needed (notice that magnets do not cover the entire circumference but about 2/3 of it). Superconductive magnets are based on NbTi cables, cooled thanks to about 96 tons of liquid helium. The beams are focused thanks to 392 quadrupole 3 m long magnets.

The acceleration up to the design value of $\sqrt{s} = 14$ TeV is reached by 16 *radiofrequency* cavities (RF) housed in four cylindrical refrigerators. The maximum energy is reached around 20 minutes after protons are injected in the LHC beam pipe. The oscillations of the RF group protons in so-called *bunches*: in nominal operating conditions, each beam is made of about 2800 bunches, each containing $\sim 10^{11}$ protons revolving with a beam crossing frequency of 40 MHz. The two beam pipes have four point of intersection, corresponding to the four main experiments.

A fundamental quantity used to understand the possibility of the machine, as well as the technical challeges for the experimental setup, is the *luminosity* $\mathcal{L}$, defined as:

$$\mathcal{L} = f \frac{n_1 n_2}{4\pi \sigma_x \sigma_y} \tag{2.1}$$

where n_i is the number of particles in the bunch, f is the crossing frequency and σ_x, σ_y are the tranverse dimensions of the beam.

Knowing the production cross section σ_p of a physical process, we can then calculate the *event rate* (that is, the number of events per second) as:

$$R = \mathcal{L}\sigma_p \tag{2.2}$$

As previously mentioned, the number of protons per bunch is $N \sim 10^{11}$; this implies the probability of overlapping events in the same time of data acquisition, referred to as pile-up (PU).

2.2 Future LHC scenarios

With LHC data taking at $\sqrt{s} = 14$ TeV, a deeper knowledge of the SM-predicted processes will be achieved. However, in order to face new challenges and explore the possibility of new physics BSM, a substantial upgrade of the accelerator is planned. In this new regime, called High Luminosity LHC (HL-LHC), the accelerator will produce pp collisions at 14 TeV, with an instantaneous luminosity of $\mathcal{L} = 5 \times 10^{34}$ cm^{-2}s^{-1}. After Run 3 (the period of data taking covering the years 2021-2023), keeping working with current accelerator design would mean having little statistical gain; this is one of the main motivation for the HL-LHC improvements [52]. Moreover, with an increased instantaneous luminosity even the rarest events predicted by or beyond the Standard Model could be observed.

Another possible future LHC regime is under study, the so-called High Energy LHC (HE-LHC), that could follow HL-LHC. In this scenario, proton-proton collisions wuold be provided at an increased center-of-mass energy of 27 TeV.

In this thesis I will focus on the possible performance of the HE-LHC scenario studying the HH→ b$\bar{\text{b}}$ZZ(4ℓ) channel and I will present a comparison with the same study performed in the HL-LHC scenario.

2.2.1 HL-LHC

In Figure 2.2 the LHC baseline program is shown: we are now at the beginning of the *Long Shutdown 2* (LS2) phase that will last until 2020; after that, a three-years data taking (Run 3) is scheduled with a center-of-mass energy of $\sqrt{s} = 14$ TeV. During the LS2, some upgrades will be performed [53]; in particular, the injector system will be updated [54] to match the HL-LHC requirements, including the realization of a new linear accelerator, the LINAC4 [55], and an improvement of both the PSB and SPS. Moreover, the first phase of the detector upgrade will be performed (Section 2.4.1).

To increase the luminosity of the LHC for the HL-LHC era, the LS3 is planned to start in 2024, with a major upgrade of the accelerator.

The main goals to be reached are:

- a peak luminosity of $\mathcal{L} = 5 \times 10^{34}$ cm^{-2}s^{-1}, that implies an increasing of detectors pile-up up to 200;

- an integrated luminosity of $L = 250$ fb^{-1} per year, with the ultimate goal of $L = 3000$ fb^{-1} in the full HL-LHC data acquisition period.

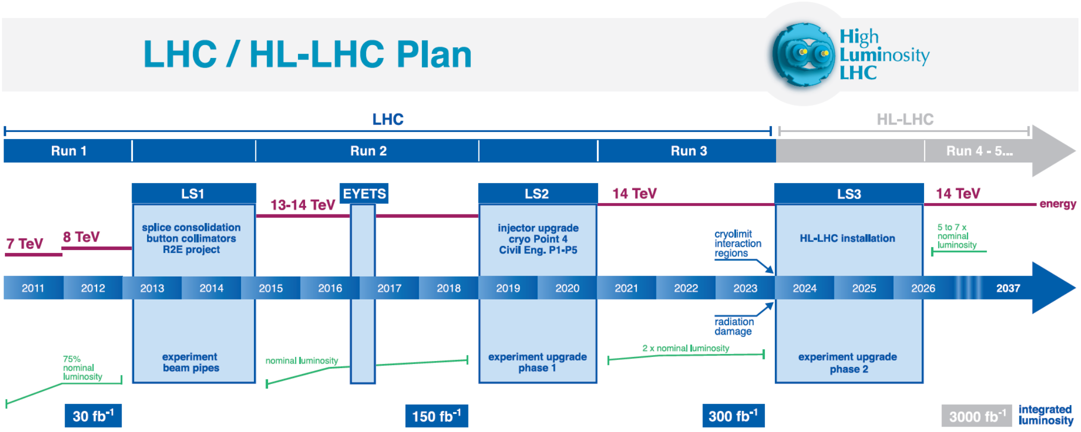

Figure 2.2: LHC baseline plan for the next twenty years [52].

In order to maximize the efficiency of the detectors (that is, limit the peak pile-up), HL-LHC will work in luminosity-leveled mode. As shown in Figure 2.3, the average luminosity achieved in the luminosity-leveled mode is almost the same than without leveling, but with a much lower maximum peak.

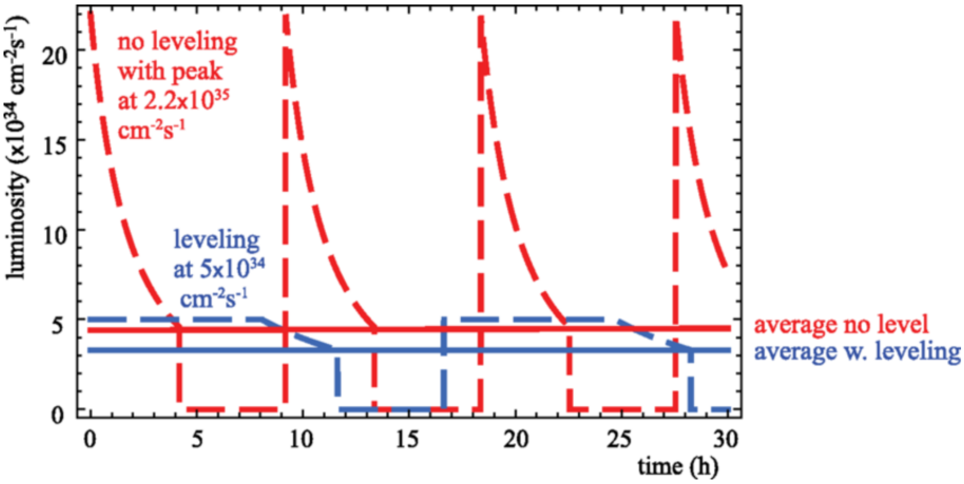

Figure 2.3: Luminosity profile for HL-LHC with and without levelling [52].

In order to have an accelator operating with these new characteristics (main parameters are reported in Table 2.1), some systems need to be substituted or improved, such as:

- **inner quadrupoles**. They will receive a dose of 30 MGy after about 300 fb^{-1}, resulting in possible damage; their replacement should take place before damages occur;

- **cryogenics**. A new cryogenics plant needs to be installed in order to increase machine availability;
- **collimation system**. It needs to be adapted to be compatible with the increased beam intensities;
- **dipole magnets**. The best solution seems to use dipoles with higher field (11 T) but shorter length (11 m) than the actual ones;
- **Quench Protection System**. Particular attention to machine protection and the kicker system is required;
- **remote manipulation**. This is necessary in order to minimize radiation doses during interventions.

2.2.2 HE-LHC

The central idea for the possible HE-LHC scenario [56] is to build up an accelarating system in order to provide pp collisions with a center-of-mass energy of about 27 TeV, and to reach an integrated luminosity up to 15 ab^{-1} in over twenty years of operation. With these new conditions, some potentially interesting physics results could be reached [57]:

- the direct search for new particles, performed in an extended mass region with repect to the HL-LHC scenario;
- the study of the structure of the Higgs potential;
- the improvement of the precision of the HL-LHC measurements, which leads to a better sensitivity to BSM physics, including SuperSimmetry and Dark Matter particles.

The main improvements to the LHC machine needed to realize the HE upgrade are:

- **dipole magnets**. In order to keep a proton beam of 13.5 TeV in a circular orbit, a larger magnetic field is needed. For this purpose niobium-tin (NbTi) magnets generating 16 T magnetic field will be used [58];

- **beam screen**. This is needed because of the increase of synchrotron radiation (SR) in the HE scenario, about 5-20 times higher than the actual one. Without the screen, SR would be absorbed by the magnets and could trigger a magnet quench [59];

- **crab cavities**. They are superconducting RF devices that generate transverse electric fields capable of rotate each bunch, providing a head-on collision [52];

- **collimators**. The same configuration than in the HL-LHC scenario will be kept;

- **injector upgrade** [60], already planned for LHC in 2020. In the HE-LHC scenario, three different ways of injection could be used: protons could come from the present SPS with an energy of 450 GeV, from a new single-layer superconducting synchrotron with an energy of 900 GeV or from a new double-layer synchrotron with an energy of 1.3 TeV [61];

- **cryogenics**. Eight new cryoplants will be needed, each reaching 1.5 times the present cryoplant capacity;

- **optics**. Two different alternatives, denoted “18×90” and “23×90” (with 18 and 23 cells, respectively), are being taken into account, with major features reported in Table 2.2. Each cell has a so-called FODO structure, consisting of alternated focusing and defocusing quadrupole lenses, with dipole and other multipole magnets installed between them.

A typical day in the HE-LHC scenario is reported in Figure 2.4, while a comparison between main characteristics of both High Luminosity and High Energy scenarios is described in Table 2.1

Parameter	unit	**HL-LHC**	**HE-LHC**
$\sqrt{s}$	[TeV]	14	27
Injection energy	[TeV]	0.45	0.45/0.9/1.3
Dipole field	[T]	8.33	16
N_b	10^{11}	2.2	2.2
Beam current	[A]	1.12	1.12
Bunch spacing	[ns]	25	25 (12.5)
Luminosity per year	[fb^{-1}]	250	730

Table 2.1: Comparison of the main operational parameters of an accelerating machine between High Luminosity LHC and High Energy LHC [52, 56]. Number in parentheses are alternative operational options.

Parameter	unit	23×90	18×90
Cell length	[m]	106.9	137.2
Quadrupole length	[m]	3.5	2.8
Dipole field for 13.5 TeV	[T]	16.59	15.83
$\sqrt{s}$ for 16 T dipole	[TeV]	26.01	27.28

Table 2.2: Comparison between the two optics design [56].

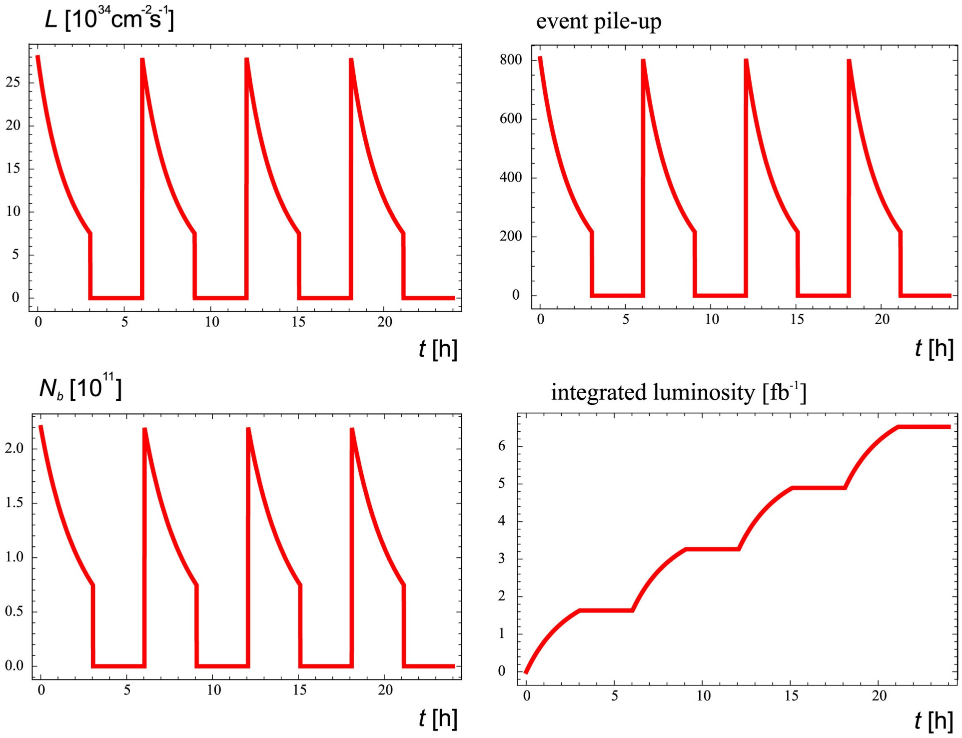

Figure 2.4: Typical day at 100% machine availability for the HE-LHC scenario. From the top left to the bottom right instantaneous luminosity, pile-up, number of particle per bunch, and integrated luminosity as a function of time are shown [62].

2.3 The CMS experiment

> *Un disegno che mi ha conquistato per la sua bellezza e la chiarezza senza compromessi che emana.*

With these words Guido Tonelli [63], the CMS 2010-2011 spokeperson, explains why he decided, together with his colleagues, to carry on with the project in spite of the general skepticism at the time of the first proposal. CMS is a so-called multipurpose experiment [64, 65] made of high quality subdetectors, each capable to detect a specific type or group of particles. Its construction was optimized in order to find a clear signature of the Higgs boson, but its performace are excellent also for other types of studies such as top, beauty and τ physics [66]. The structure of the detector is a cylinder 21.6 m long with a diameter of 15 m, for a total weight of 14500 tons.

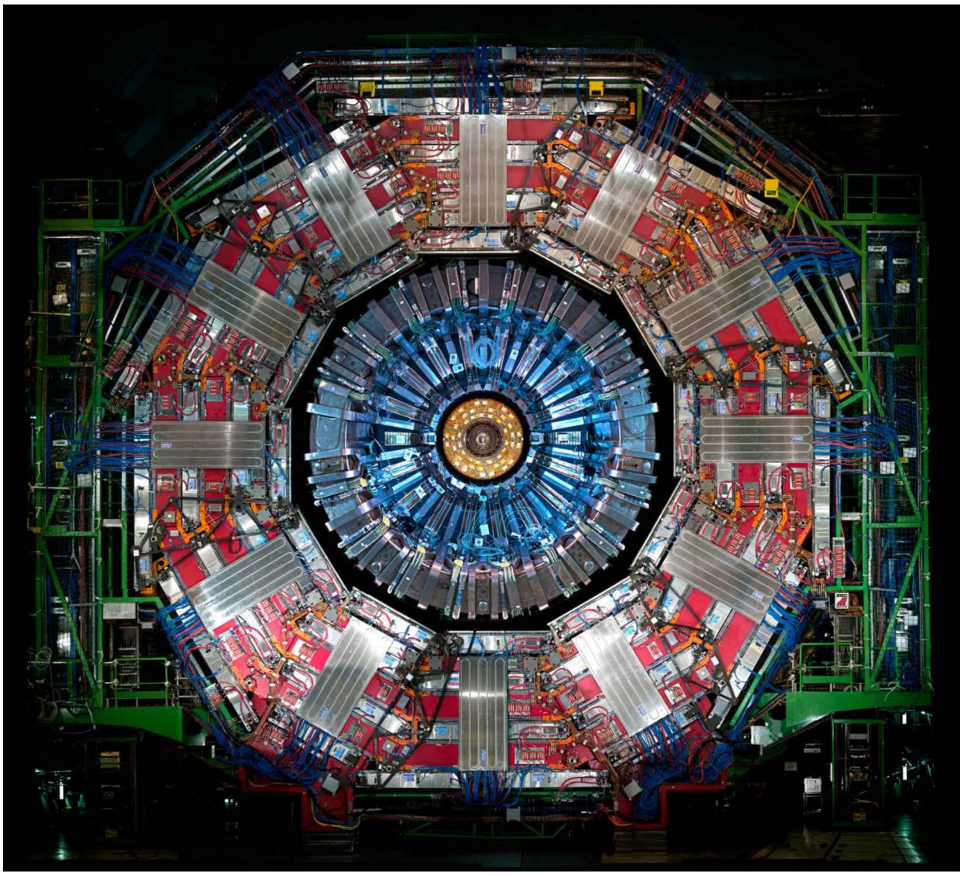

Figure 2.5: A transverse view of the CMS detector [67].

In Figure 2.5 a trasverse view of the detector is shown. Starting from the inner part, it is basically composed of concentrical subdetectors:

- the inner *tracking system*, that allows the charged particle tracks reconstruction;
- the *electromagnetic calorimeter* (ECAL), responsible for the detection and identification of photons and electrons, which deposit almost all their energy in this subdetector;
- the *hadronic calorimeter* (HCAL), which provides hadron identification as well as jets reconstruction;
- the *muon system*, in which muons can be identified.

A *solenoid magnet* surrounds the calorimeters and the tracking system: it allows to bend charged particles in order to identify their charge and momentum. A schematic view of the entire detector is presented in Figure 2.6.

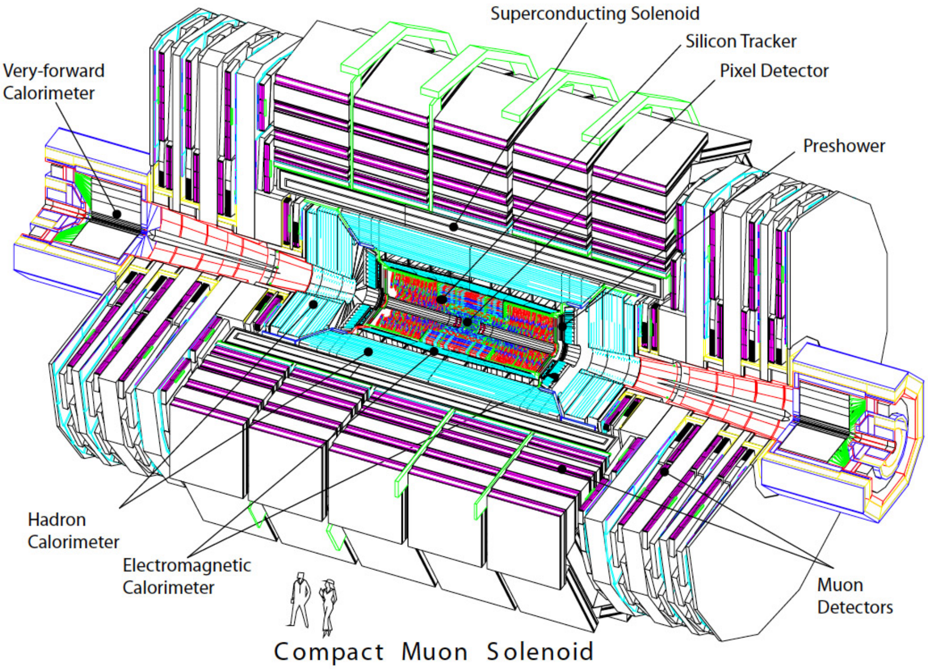

Figure 2.6: A schematic view of the CMS detector [64].

2.3.1 The CMS coordinate system

The origin of the cartesian reference frame is placed in the CMS interaction point and the axis are defined as follows:

- x-axis points to the centre of the LHC ring;
- y-axis points upwards;
- z-axis points to the anticlockwise beam direction.

The x-y plane is perpendicular to the beam line, and it is called transverse plane, while the z-direction is called longitudinal. Moreover, it is convenient to define cylindrical coordinates:

- r is the distance from the interaction point in the x-y plane, defined as $r = \sqrt{x^2 + y^2}$;
- the azimuthal angle ϕ is measured from the x-axis in the transverse plane;
- the polar angle θ is measured from the z-axis in the z-y plane.

With respect to these coordinates, some useful quantities are defined:

- the particle momentum is composed of the longitudinal and tranverse components:

$$p = \sqrt{p_z^2 + p_\mathrm{T}^2} \quad \text{where } p_\mathrm{T}\sqrt{p_x^2 + p_y^2}; \tag{2.3}$$

- the tranverse energy E_T is defined as:

$$E_T = E \sin\theta \tag{2.4}$$

- considering momentum conservation, the missing tranverse energy E_T^{miss} is defined as:

$$E_T^{\mathrm{miss}} = -\sum_i \vec{p}_T^{\,i} \qquad |E_T\mathrm{miss}| = \sqrt{(\sum_i p_x^i)^2 + (\sum_i p_y^i)^2} \tag{2.5}$$

- the rapidity y, which is Lorentz-invariant, is

$$y = \frac{1}{2} \ln \frac{E + p_z}{E - p_z} \tag{2.6}$$

- the pseudorapidity η is:

$$\eta = -\ln\left(\tan\frac{\theta}{2}\right) \tag{2.7}$$

  that is, small θ-angles correspond to large η-values;

- the distance in the $\eta - \theta$ plane is expressed by

$$\Delta R = \sqrt{(\Delta\eta)^2 + (\Delta\phi)^2} \tag{2.8}$$

  where $\Delta\eta$ and $\Delta\phi$ are the distance between two objects in terms of pseurapidity and azimuthal angle.

2.3.2 Magnet

As already mentioned, the magnetic field bends charged particles providing the possibility to measure their transverse momentum and charge in the tracker and muon system. This information, combined with the one from the other subdetectors, allows charged particles identification; the CMS detector uses a superconducting niobium-titanium solenoid [68] embedded in a 12000-ton iron return yoke.

Since the beginning it was clear the importance to have the highest magnetic field possible, in order to bend even high-energy particles; this allows to extend particle identification in a wide operational range and to reach a good momentum resolution. The magnetic field provided by the solenoid is 4 T and it is maintained at a temperature of 4 K by an external helium-cryogenic system keeping it in superconducting mode.

2.3.3 Tracker

The purpose of the tracking system [69] is to provide charged particle tracks reconstruction, good momentum resolution for energetic leptons, primary and secondary vertex reconstruction and precise pattern recognition. To reach these goals, the main requirements of the detector should be:

- high granularity;
- fast response;

- measurement redundancy.

The transverse momentum resolution achieved is

$$\delta p_{\mathrm{T}}/p_{\mathrm{T}} = (15 \cdot p_{\mathrm{T}} \oplus 0.5)\%$$

The entire tracking system is based on silicon detectors, divided in two different categories: Pixel and MicroStrip detectors.

Silicon Pixel detector

The Pixel detector covers the closest region around the beam pipe (with $r < 20$ cm) and provides precise vertex reconstruction and impact parameter measurement. Three barrel layers, each consisting of two half-cylinders, surround the beam pipe whereas two endcap disks for each side cover the forward region, as shown in Figure 2.7. The full Pixel subdetector is made of about 66 million cells, each of 100×150 μm^2, grouped in 1400 sensors with a total surface of 1.06 m^2.

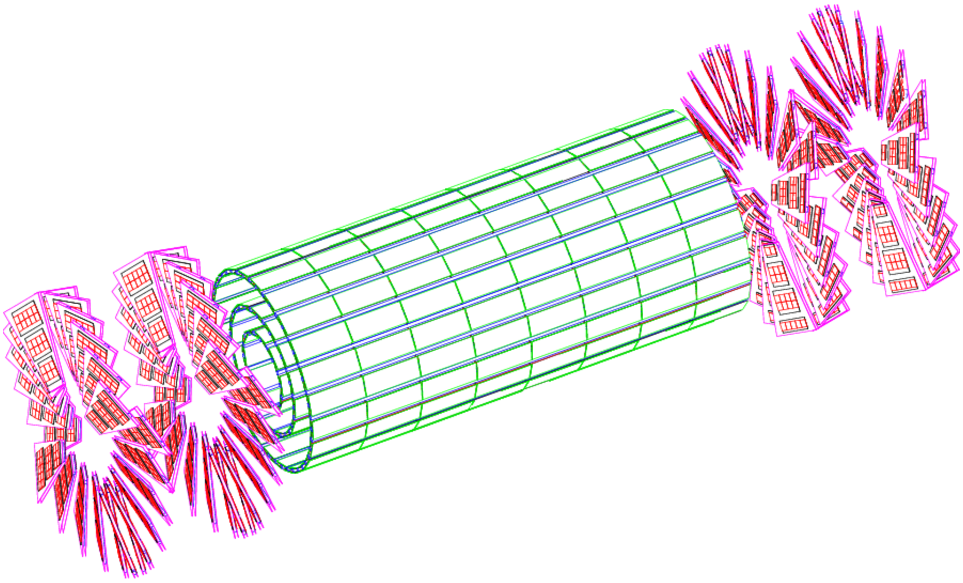

Figure 2.7: Schematic view of the Pixel detector system [64].

With this configuration, a spatial resolution of 10 μm in the $r - \theta$ plane and of 15 μm in the z-direction are achieved in the barrel region; in the endcaps slightly lower resolutions are obtained (15 μm and 20 μm, respectively).

Silicon Strip tracker

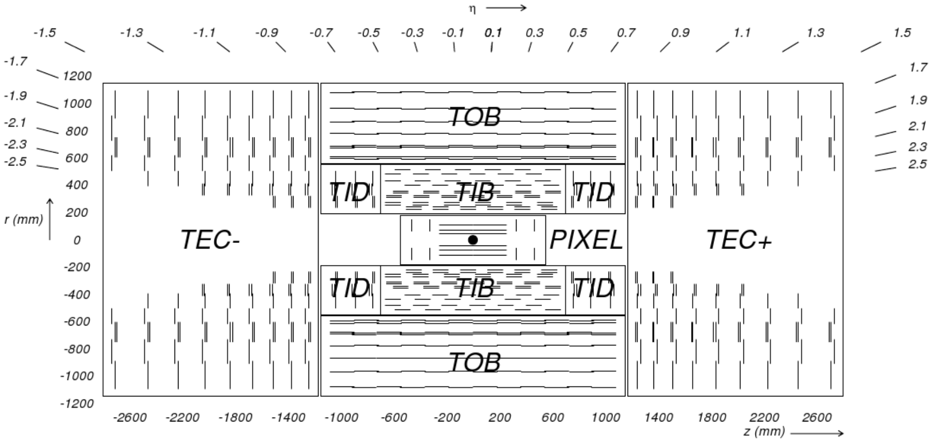

Figure 2.8: Schematic view of the Microstrip Tracker, where each line represents a module [69].

The MicroStrip detector covers the outer region, going from a radius of $r = 20$ cm to $r = 120$ cm to collect hits of particles in order to reconstruct their trajectories. It is composed of four inner barrel layers (TIB) and two inner endcaps (TID). The outer barrel (TOB) is instead made of six concentric layers and two endcaps close the tracker (TEC). A schematic view of the tracker is shown in Figure 2.8. The spatial resolution of this subdetector ranges from 40 to 60 μm in the $r - \theta$ plane, while it is of about 500 μm in the z-direction.

2.3.4 The Electromagnetic Calorimeter

The CMS Electromagnetic Calorimeter (ECAL) is a hermetic, homogeneous lead tungstate ($PbWO_4$) crystal scintillating calorimeter which provides photon and electron/positron identification [70]. The choice of the material was made in order to obtain good energy resolution, to minimize detector dimensions and have a fast response. It is made of about 75000 crystals, arranged in a central barrel section (EB) covering a region up to $|\eta| < 1.48$ and two endcap sections (EE) in the region $1.48 < |\eta| < 3.0$. In order to optimize photon-π^0 separation, a preshower detector (ES) realized with a lead absorber and silicon strip sensors is placed in front of the endcaps at $1.65 < |\eta| < 2.6$. The full calorimeter scheme is shown in Figure 2.9.

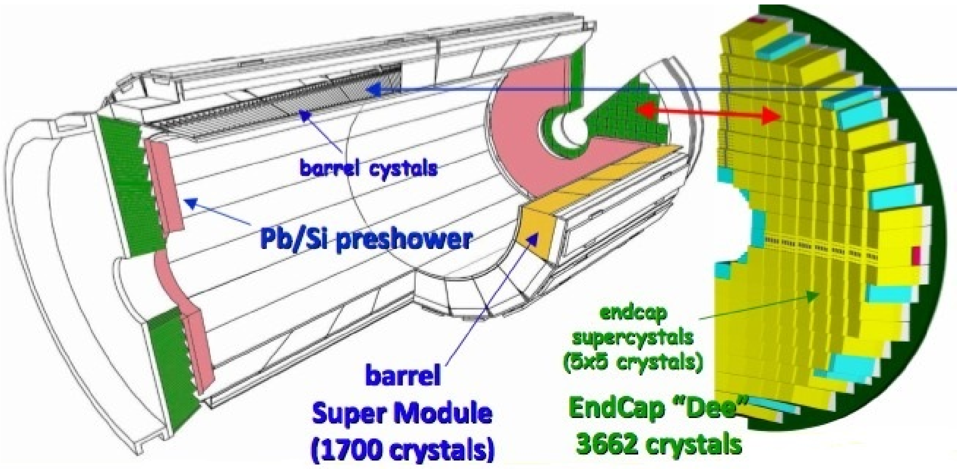

Figure 2.9: Schematic view of the Electromagnetic Calorimeter [71].

Light produced in the scintillating material is converted in electrons in the barrel section by avalanche photodiodes (APD) with gain set to ∼50, while in the endcap region vacuum photo-triodes are used, with gain ∼10.

A parametrization of the energy resolution for a particle with energy E in the mass range 25-500 GeV is given by:

$$\left(\frac{\sigma}{E}\right)^2 = \left(\frac{a}{\sqrt{E}}\right)^2 + \left(\frac{b}{E}\right)^2 + c^2 \tag{2.9}$$

where:

- a is the stochastic term, taking into account fluctuations in photo-electron production as well as shower containment;
- b is the noise term, due to electronics and pile-up noise;
- c is the constant term including ECAL calibration, energy leakage and non-uniformity of crystals.

With test beams calibrations, energy resolution was find to be (for a particle with energy E in GeV):

$$\left(\frac{\sigma}{E}\right)^2 = \left(\frac{2.8\%}{\sqrt{E}}\right)^2 + \left(\frac{12\%}{E}\right)^2 + (0.3\%)^2 \tag{2.10}$$

2.3.5 The Hadron Calorimeter

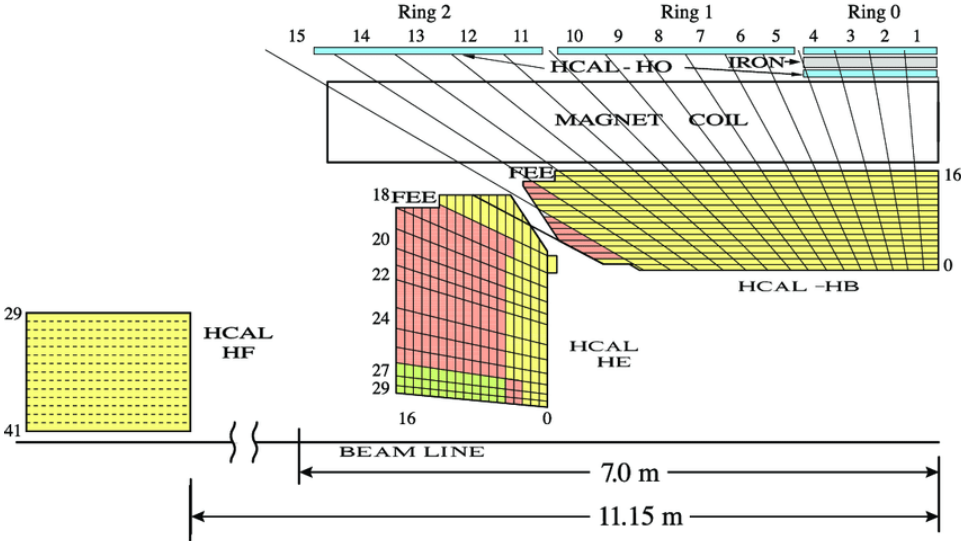

Figure 2.10: Schematic view of the Hadron Calorimeter [72].

The Hadron Calorimeter (HCAL) [73] is used to identify hadrons, and gives a measurement of the energy deposit of hadrons, providing also an indirect indication of the presence of non-interacting particles such as neutrinos. In order to limit information loss, it needs to be as hermetic as possible, covering the η region up to $|\eta| = 5$. HCAL is a sampling calorimeter, with two different working regions (Figure 2.10):

- the Barrel HCAL (HB) and Endcap HCAL (HE) are made of brass plates as absorber alternated with plastic scintillators as active material and are placed between ECAL and the magnet; these detectors are particularly useful for small dimension showers;
- two Forward Calorimeters (HF) are placed around the beam-pipe at $|z| = 11.2$ m and cover the η-region up to $|\eta| = 5$. Since they are closer to the beam line, they are made of radiation hard materials such as steel as absorber and quartz fibers (emitting Cherenkov light) as active material.

The energy resolutions for the different regions are:

$$\frac{\sigma}{E} \simeq \frac{65\%}{\sqrt{E}} \oplus 5\% \text{ for HB} \tag{2.11}$$

$$\frac{\sigma}{E} \simeq \frac{85\%}{\sqrt{E}} \oplus 5\% \text{ for HE} \tag{2.12}$$

$$\frac{\sigma}{E} \simeq \frac{100\%}{\sqrt{E}} \oplus 5\% \text{ for HF} \tag{2.13}$$

2.3.6 Muon system

The CMS muon system [74] is the outer part of the detector. Muons are highly penetrating and they are basically the only particles reaching this region of the CMS detector; the muon system is responsible for their identifications as well as p_{T} measurement. It is important to underline that reconstructed trajectories in this sub-detector must be related to vertex and tracks reconstruction from the inner tracker: a precise alignment of the two parts is crucial. As previously mentioned, the measurement of the curvature radius (needed for momentum calculation) is possible thanks to the 1.8 T magnetic field created by the return yoke.

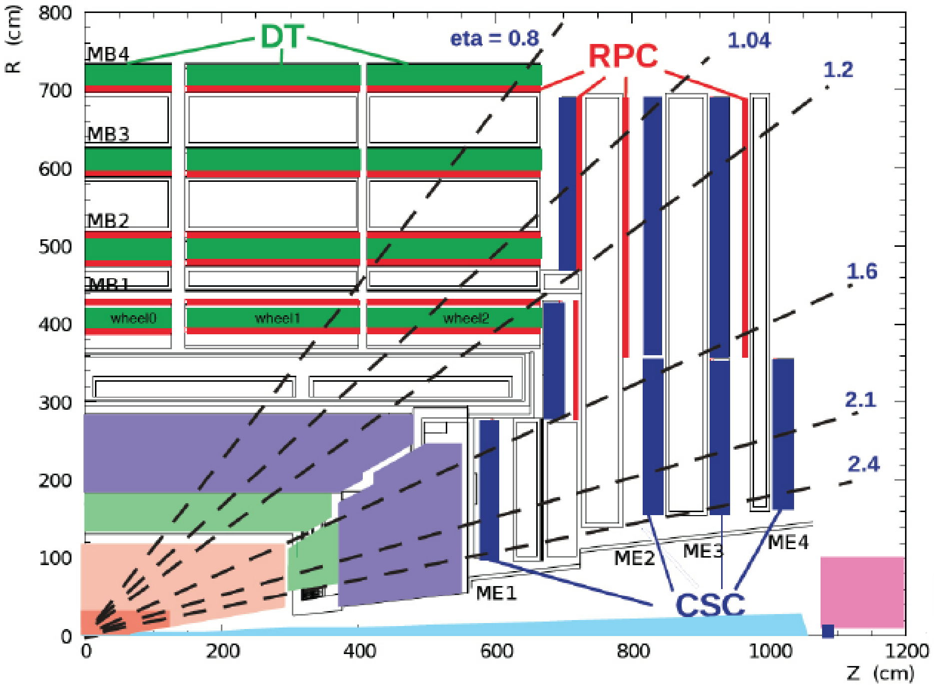

Figure 2.11: The CMS muon system [64].

This system, shown in Figure 2.11, is totally based on gaseous detectors that exploit the ionization electrons created by charged particles passing through the gas. Three different technologies are used: Drift Tubes (DTs), Cathode Strip Chambers (CSCs) and Resistive Plate Charmbers (RPCs).

Drift Tubes

Drift Tubes measure muon position in the barrel part, covering the region up to $|\eta| < 1.2$. They are grouped into four stations integrated in the return yoke of the magnet: the inner three stations (MB1, MB2, and MB3) are composed of 60 chambers, while the outer one (MB4) is made of 70 chambers. The system is divided into five wheels in the z-direction, with each wheel divided into twelve sectors (Figure 2.12).

The MB1, MB2, and MB3 stations are composed of three independent subunits called Super Layers (SL); two SL give a measure of the coordinate in the bending plane while the third measures the coordinate along the beam. MB4 station, instead, has only two SL to measure the coordinate in the bending plane.

The basic element of each SL is a drift tube covering an area of 4.2×1.3 cm^2 filled with Ar (85%) and CO_2 (15%).

Cathode Strip Chambers

Cathode Strip Chambers (CSC) are used in the endcap region where a non-uniform magnetic field is present and particle rate is high. Each endcap is divided into four stations, each composed of chambers with a trapezoidal shape, arranged in a serie of concentric rings centered on the beam line. Each chamber is a Multiwire Proportional Chamber (MWPC) with a cathode plane segmented in strips orthogonal to the anode wire in order to have a 2D information of the particle position(Figure 2.13).

The gas used to fill the chambers is a mixture of Ar (30%), CO_2 (50%) and CF_4 (20%).

Resistive Plate Chambers

Resistive Plate Chambers (RPC) (Figure 2.14) are fast gaseous detectors providing a muon trigger system parrallel with those of DTs and CSCs. They are placed both in the barrel and in the endcap region to provide redundancy.

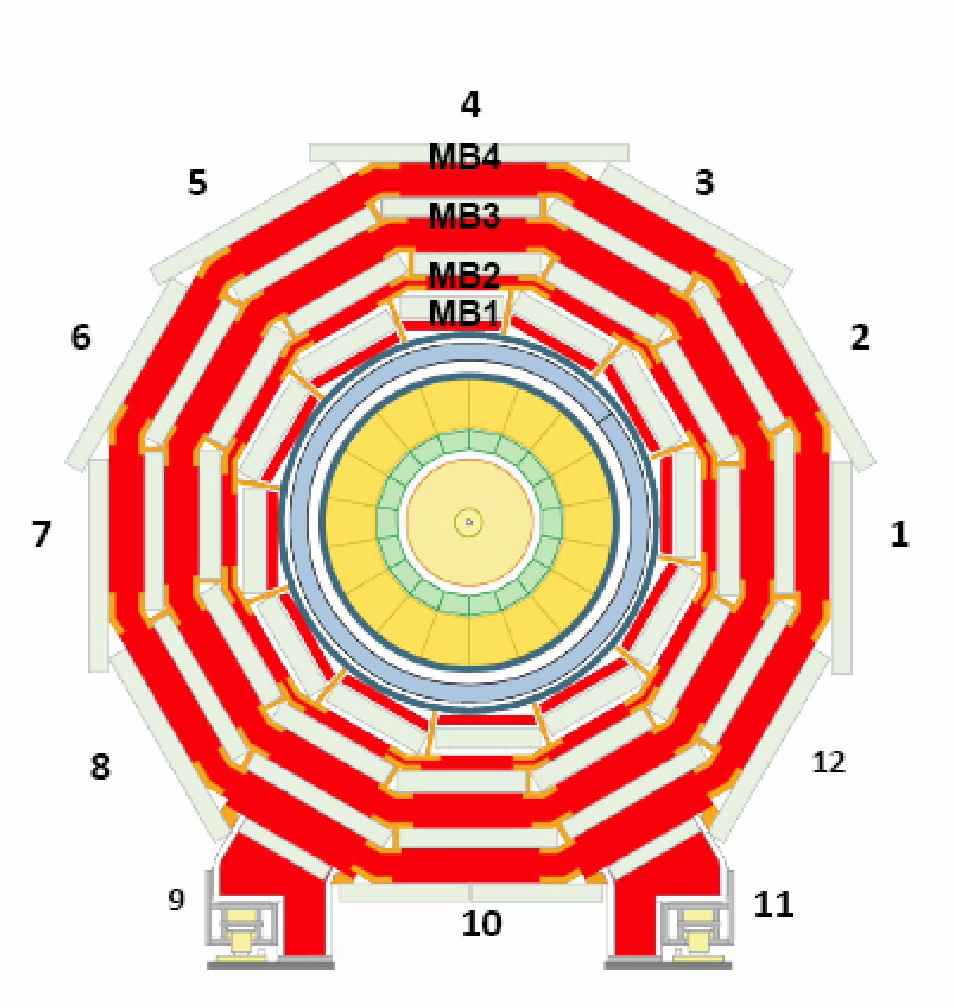

Figure 2.12: Transvers view of the DT system: numbers indicate the sector formed by the DT chambers (gray) embedded in the yoke (red) [75].

They are made of four planes, two positively-charged anodes and two negatively-charged cathodes, alternated to form two gaps filled with a mixture of $C_2H_2F_4$ (96.2 %), C_4H_{10} (3.5 %), and SF_6 (0.3%). Thanks to their fast response (of the order of 3 ns) they provide excellent time resolution and can thus be used for triggering.

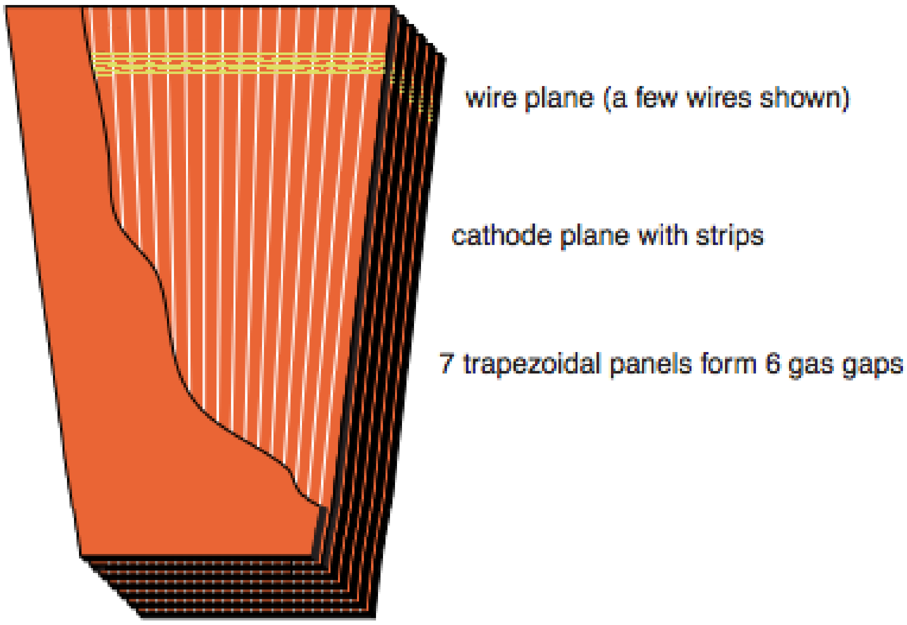

Figure 2.13: Schematic view of a CSC [64].

2.3.7 The Trigger and the Data Acquisition system

The Trigger and Data Acquisition system (DAQ) [77, 78] is designed to analyze and collect only interesting information from each event. About one billion pp interactions take place every second: an online event selection is crucial to discriminate and acquire only physically interesting events. However, considering the bunch crossing rate, particles from a new bunch crossing can be produced when those from the previous one have not been yet recorded: the solution is a multilevel trigger system; moreover, data are stored in pipelines that can retain information from more interactions.

The CMS trigger system is divided into two levels:

- **Level-1 Trigger (L1T)**, that reduces the rate from ∼40 MHz (the beam crossing rate) to ∼100 kHz, with pipeline storage time of 2.3 μs. It involves calorimeter and muon systems: the L1 performs a rough recontruction and its decision is based on the presence of objects such as photons, electrons, muons and jets, including a test of some variables such as E_{T}, p_{T}, and $E_{\mathrm{T}}^{\mathrm{miss}}$. If the L1T generates an accept, information of the event is delivered to the second level of trigger.

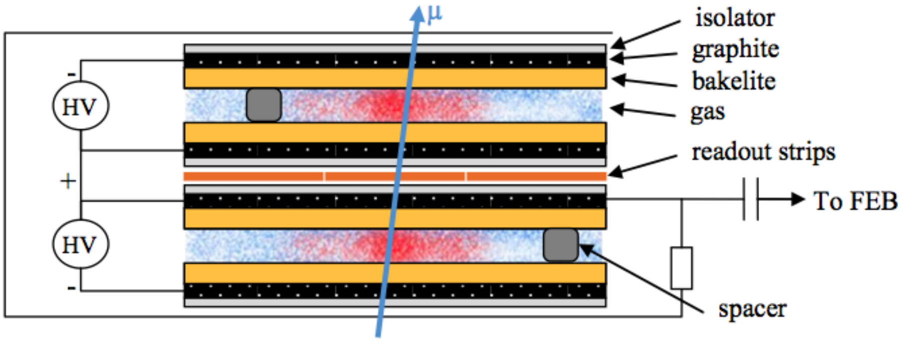

Figure 2.14: Schematic view of a RPC [76].

- **High Level Trigger (HLT)** is a software system reducing the rate from ∼100 kHz to ∼1 kHz. It performs a better reconstruction as well as selection of events. At the end of this process, using different variables, events are assigned to specific data-set, differing each other for the different potential physics channel.

2.4 The CMS detector upgrade

As already mentioned, the upgrade of the LHC scheduled in LS2 and LS3 is driven by physical considerations; the increase in the luminosity or the center-of-mass energy will make it possible to extend the present knowledge of the SM and to possibly discover new physics BSM. Experimental conditions will be more challenging for the detectors, which will have to be improved in order to fully exploit the new machine potentiality.

A two-phase upgrade project is planned for the CMS detector:

- **Phase-I upgrade** [79], planned during the LS2 (2019-2020), involving Pixel detector, the Trigger system, the HCAL and the muon system;

- **Phase-II upgrade** [80], scheduled during the LS3 (starting from 2024), involving the tracker, the muon system, the trigger and the DAQ. During this phase, a new High Granularity Calorimeter (HGCAL) will also replace endcap ECAL and HCAL.

2.4.1 Phase-I detector upgrade

Muon system

The muon system will be improved in order to enhance the trigger performance on muons with high transverse momentum. An additional fourth layer of chambers with associated readout will be added to reduce accidental trigger rate, preserving a low p_{T} threshold for L1T at high luminosity. Moreover, layer 1 electronics will be upgraded so every strip can be read out separately. In the same way, an additional layer of RPC will be installed to extend η-coverage.

To cope with new experimental conditions, the CMS Collaboration will install a new detector based on the *Gas Electron Multiplier* (GEM) technology [81], which has been proved to operate reliably at rates comparable to those of HL-LHC. A new chamber (GE1/1) [82], composed of two layers (each made of three subsequent GEM foils) will be placed in front of the first CSC station (ME1/1) (Figure 2.16).

Hadron Calorimeter

This detector upgrade is needed to handle higher instantaneous luminosity and improve overall robustness and efficiency.

Concerning calorimeters inside the solenoid (HB/HE/HO), improved photodetectors, the Silicon Photomultiplier (SiPM), will be installed; they are characterized by better quantum efficiency and higher gain with respect to the present ones. Thanks to the high performance of SiPM, a finer longitudinal segmentation will be realized, allowing better hadronic shower reconstruction.

Some upgrades are scheduled also for the HF, including the replacement of the Photomultipliers Tubes (PMT) with multi-anode tubes to reduce the amount of Cherenkov light generated by charged particles and improve rejection of spurious signals.

Pixel tracker

The goal is to replace the present pixel detector to cope with higher instantaneous luminosities (up to 2×10^{34} cm^{-2}s^{-1}). The future Pixel tracker will have an additional barrel layer at a radius of 16 cm and another forward disk to maintain the present tracking performance even with higher luminosity.

Trigger and DAQ

The new Trigger technology will be more maintainable and flexible. For what concerns the calorimeter trigger, improved algorithm will be implemented while the muon trigger will be upgraded using more powerful FPGAs and larger memories.

At the same time, due to the higher luminosity and the larger number of detector channels, it will be necessary to increase DAQ-bandwidth by a factor of two to five to acquire larger amount of data.

2.4.2 Phase-II detector upgrade

The Phase-II detector upgrade is planned in order to cope with the HL-LHC challenging conditions, especially the higher instantaneous luminosity. This will necessarily increase the interaction rate and pile-up: the main goal is to maintain present and Phase-I performance in this scenario. Pile-up mitigation will be reached by increasing the tracker granularity while new endcap calorimeters will provide improved energy resolution.

To fully exploit higher luminosity, the trigger electronics will be upgraded improving p_{T} resolution and lowering effects from combinatorial backgrounds. A new approach is required, as discussed in detail later.

Finally, a major goal of the HL-LHC physics program is to measure processes with small production sections; therefore, upgrades in the forward region of the detector are needed to maximize physical acceptance.

Tracker

The Tracker will be completely replaced for Phase-II [83, 84] in order to both handle higher amount of data and to become more radiation hard. The granularity of both the outer tracker and the pixel detector will be increased by a factor 4; concerning the outer tracker, this will be achieved shortening the length of the silicon strips, providing improved p_{T} resolution, while in the pixel system smaller pixels and thinner sensors will be implemented. The latter solution will improve impact parameter resolution and two-tracks separation. In the forward region, up to ten additional disks will be installed, extending the η-coverage up to $|\eta| \sim 4$.

In particular:

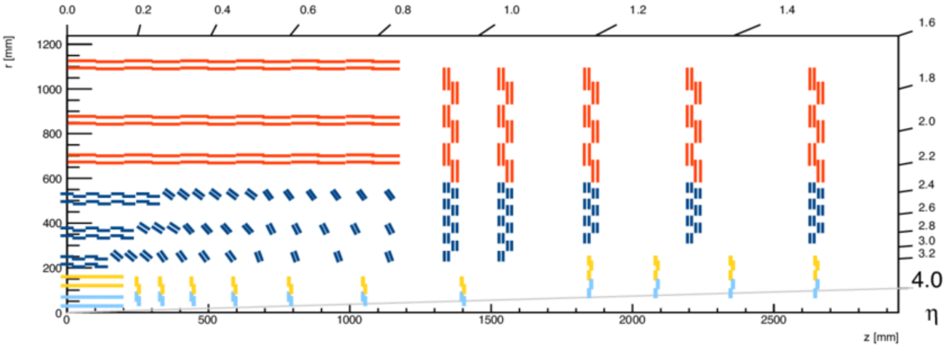

Figure 2.15: Schematic view of one quarter of the Phase-II tracker layout. Red lines represent 2S modules, blue ones are PS modules [84].

- **Pixel Tracker**: the geometry of Phase-I Pixel Tracker (four barrel layers and three forward disks) will be used as a starting point; in the forward direction, an extension will be realized increasing the number of disks up to ten; this new extended pixel detector will have an active surface of ∼4 m^2 (with respect to 2.7 m^2 of the Phase-I one). Moreover, to cope with higher integrated luminosity, pixel sizes of 25×100 μm^2 or 50×50 μm^2 (arranged in thin planar silicon sensors) have been considered, with a reduction of the surface area of a factor ∼6 compared to the present pixel cells.

- **Outer Tracker**: results from various studies showed that the best solution is to use 200 μm active thickness sensors. To cope with a higher instantaneous luminosity, the goal is to implement (both in the barrel and in the endcap region) modules capable of rejecting signals from particles below a certain p_T threshold (around 2 GeV). Two version are devised: **2S modules** are made of two superimposed strip sensors (10×10 cm^2) segmented in strips of 90 μm × 5 cm; they will be placed in the outer region (Figure 2.15). **PS modules** are composed of two sensors, one segmented in strips of 100 μm × 2.3 cm and the other segmented in macropixels of 100 μm × 1.4 mm; these devices will cover the radial region between $20 < r < 60$ cm (Figure 2.15).

Muon system

The only region of the muon detector with no redundant cover is the one corresponding to $1.5 \leq |\eta| \leq 2.4$, which is covered by four CSC station. For this reason, additional chambers will be installed [85]; two detectors will be realized with the GEM technology, while the other two will be made of improved RPCs; moreover, present DTs, CSCs, and RPCs will be improved to face the new challenging conditions. The new muon system setup is shown in Figure 2.16.

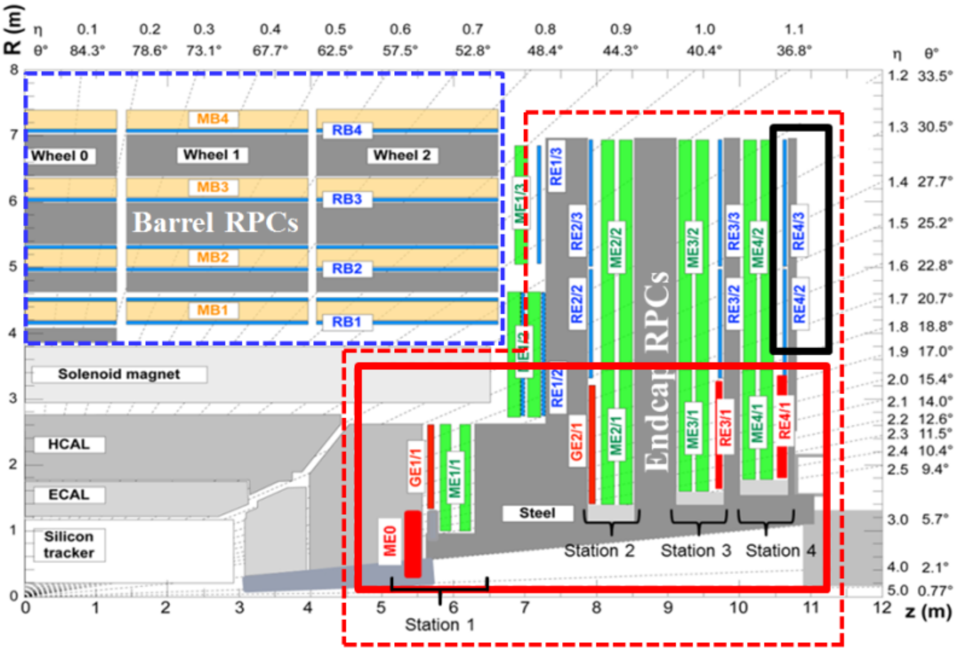

Figure 2.16: Schematic view of a quarter of the new muon system with the new stations for the Phase-II upgrade (RE3/1, RE4/1, GE2/1, and ME0) [85].

- **DTs upgrade**: present electronics can handle L1T rate up to 300 kHZ, while in the ultimate HL-LHC scenario it will reach 750 kHZ. In addition, some components are not sufficiently radiation hard. For these reasons, a new backend electronics will be implemented.
- **CSCs upgrade**: this upgrade is needed mainly to face the increased trigger latency as well as trigger rates. Like for the DTs, most of the improvements involve electronic components.

- **RPCs upgrade**: the upgrade will mainly affect the link system between front-end boards and trigger/DAQ.
- **New RPCs detectors**: the main motivation for new chambers is to obtain redundancy in the forward region. Improved RPC chambers (iRPC) will be faster and with better spatial resolution, improving background rejection and particle identification. With these new chambers (RE3/1 and RE4/1), the p_{T} assignement will also be better, improving low-p_{T} tracks suppression.
- **New GEM chambers**: the GEM technology will be implemented in the Triple-GEM configuration. The first new detector (GE2/1) covers the region $1.55 < |\eta| < 2.45$, while a second one (ME0) is planned to be installed behind the new calorimeter HGCAL to increase the muon coverage up to $|\eta| = 2.8$. GEM detectors will also be used to give trigger signal in the very forward region.

Calorimeters

As for other subdetectors, electromagnetic and hadron endcap calorimeters will suffer radiation damage and will be replaced. The solution adopted is to install, in front of the muon system, a new detector with an electromagnetic and hadronic section, the *High Granularity CALorimeter* (HGCAL) [86, 87] (a schematic view of the calorimeter itself is shown in Figure 2.17).

The main requirements for the HGCAL to cope with new experimental conditions are:

- *radiation tolerance* to preserve energy resolution even after 3000 fb^{-1};
- *dense calorimeter* to build a compact detector;
- *fine lateral granularity* to give a signal-to-noise ratio high enough to allow MIP calibration and to help two-shower separation;
- *fine longitudinal granularity* to make the detector capable of sampling the longitudinal development of the shower.

The design for the HGCAL is the following: the electromagnetic section (EE) will be composed of 28 layers, followed by the forward-hadronic (FH) calorimeter made of 12

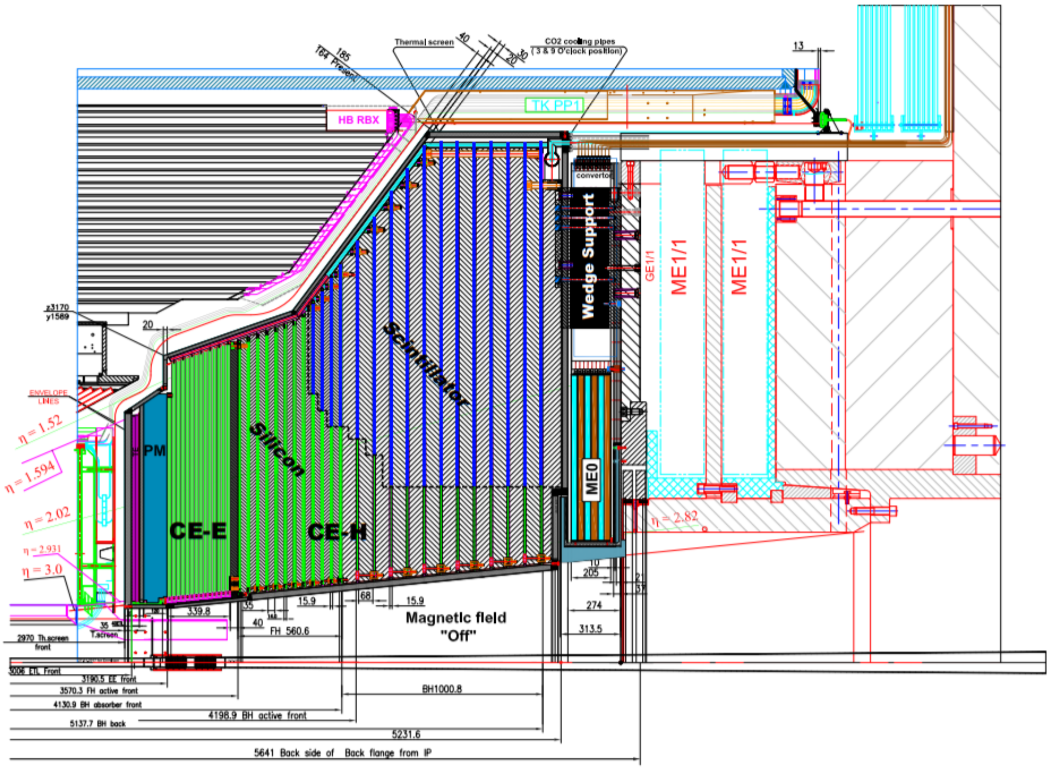

Figure 2.17: The new High Granularity Calorimeter of the CMS Phase-II detector [88].

layers; the detector is closed by a backing hadron calorimeter (BH) made of 12 layers. Considering the fact that the absorbed dose decreases from the inner to the outer part, for EE and FH a radiation-hard silicon detector will be used, while scintillators will be employed for BH. To provide small Molière radius for the electromagnetic shower, tungsten and copper will be used as absorber material, with a total EE-radiation length of about $26X_0$. Instead, brass has been proposed for the hadronic parts.

Trigger

The two level structure of the present trigger will be maintained, although the entire trigger and DAQ system will be replaced to cope with higher rate [89, 90]. Improvements will lead to a maximum L1T rate of 750 kHz with a latency of 12.5 μs; the L1T will also include tracking and HGCAL information, as shown in Figure 2.18. The Correlator Trigger will receive information from the tracker, the endcap and barrel calorimeters and the muon system, applying complex object identification algorithms to provide a list of sorted trigger objects to the Global Trigger, which also receives data from the precision proton spectrometer (CT-PPS), the beam position and timing monitors (BPTX) and the beam monitoring detectors (BRIL). The Global Trigger algorithms will be more sophisticated as well; finally, the L1-accept is sent to the CMS Trigger Control and Distribution System from which it is passed to subdetectors elecronics to start the DAQ.

For what concerns the HLT, it will have to face an input rate up to 750 kHz; it is proposed to increase its output rate up to 7.5 kHz in order to cope with the higher luminosity in the HL-LHC scenario. The processing power needs to be increased by a factor 24 (52) operating with pile-up value of 140 (200).

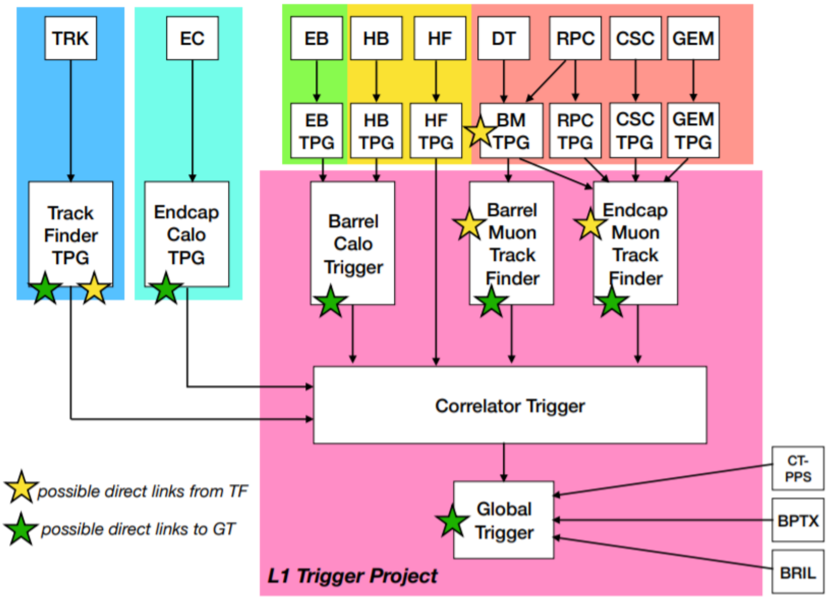

Figure 2.18: Schematic representation of the Phase-II L1 trigger [89].

Chapter 3

Event generator and simulation

The analysis described in this thesis is fully based on Monte Carlo (MC) simulations. To simulate high energy physics events, two main steps are performed:

- the event generation;
- the simulation of the detector response to the passage of particles;

After these two steps, the data obtained are in the same form of the real ones.

3.1 Event generator

An event generator is needed to simulate high energy physics events; to obtain them, a series of physics models are needed. The main concept consists in generating few body hard processes and then in simulating parton shower and hadronization to lead to a more complex final state.

For the data used in this thesis, two different software are used:

- MadGraph5_aMC@NLO [91] for the generation of hard processes;
- Pythia 8.2 [92] for parton shower and hadronization.

3.1.1 MadGraph5_aMC@NLO

MadGraph5_aMC@NLO is an event generator for high energy physics experiments which includes not only electroweak calculations but also QCD processes at the next-to-leading order (NLO) of the perturbative expansion. As the name suggests, this software merges in a unique framework both MadGraph5 [93] and aMC@NLO [94] features; it also includes new properties which make it capable to perform NLO-QCD calculations with all fundamental ingredients.

The key feature of MadGraph5_aMC@NLO is that it can compute tree-level and one-loop amplitudes for every process; prediction of physical observables is then possible. Different accuracy in perturbative calculation and precision in final state description can be reached, allowing the investigation of various scenarios within the same framework.

After the events are generated, they are stored in files which can be passed to a parton shower and hadronization MC program.

3.1.2 PYTHIA8

Pythia8 is a software for event generation, which includes a set of physics models for the evolution from a few-body hard-scattering process to a complex multiparticle final state.

Events generated with MadGraph5_aMC@NLO are in the "Les Houches Event" format (.lhe) which is fully compatible with Pythia8: in particular, calculations of matrix elements from the first can be combined exploiting Pythia8 specialities such as initial-state radiation (ISR), final-state radiation (FSR), multiparton interactions (MPI). The program works with either hadron-hadron (protons, neutrons and pions) and lepton-lepton collisions, with center-of-mass energy in the range $10\ \text{GeV} < \sqrt{s} < 100\ \text{TeV}$. It is important to notice that in Pythia8 particles are produced in vacuum and no interaction with detectors is included.

A large number of hard processes are available, including BSM physics, focusing primarily in $2 \to 1$ and $2 \to 2$ processes; it is also possible to simulate higher final-state multiplicity if the particles come from decays of resonances. Taking into account soft processes, Pythia8 is capable of describing all components contributing to the total cross section in hadronic collisions, including elastic, diffractive and non-diffractive topologies; the full derivation of various cross section contributions can be found in [92].

With regard to parton distribution, sixteen parton distribution functions (PDF) for the proton are built, with additional sets for pions and leptons. Starting from them, algorithms for parton shower production and hadronization are performed.

In order to obtain final data for the analysis, the interaction between particles and the detector has to be simulated.

3.2 Detector simulation and object reconstruction with Delphes

Detector response is usually obtained using Geant4 [95], a C++ toolkit which provides a complete simulation of the geometry and material description of the detector. In a Geant4 simulation, each particle is propagated through the materials and interactions are simulated according to an appropriate physics list (in which all the physical processes to be considered for the simulation are listed); for each interaction, the energy deposit in the detector is computed and secondary particles are produced. However, for production and analysis of large background samples, a complete simulation is not fast enough and very demanding in terms of computing time. On the contrary, a parametric description of the detector as well as algorithms for object reconstruction and identification, allow faster performance since they do not include the complete simulation of the detector materials as well as secondary processes. This parametric simulation is performed with Delphes [96], a C++ modular framework for fast multipurpose detector simulation.

Since in the Delphes framework a simplified and faster simulation is performed, it is therefore crucial to validate its results. The parametrization of the detector response is obtained comparing the Delphes results with the ones achieved from a complete simulation through the Geant4 toolkit.

As previously mentioned, the need for a faster simulation software emerges when studying large data samples and performing phenomenological studies comparing different detector configurations. The Delphes framework takes as input the most common event generator outputs and performs a quick and realistic simulation of the reconstruction of particles inside the detector volume. In addition, an emulating of a Particle-Flow (PF) reconstruction algorithm is also implemented (see Section 3.2.1).

3.2.1 Simulation of the detector

As shown in Figure 3.1, Delphes can simulate a general purpose detector composed of an inner tracker embedded in a magnetic field, electromagnetic and hadronic calorimeter and a muon system. The volume of the active material, the calorimeter segmentation and the intensity of the magnetic field can be defined by the user.

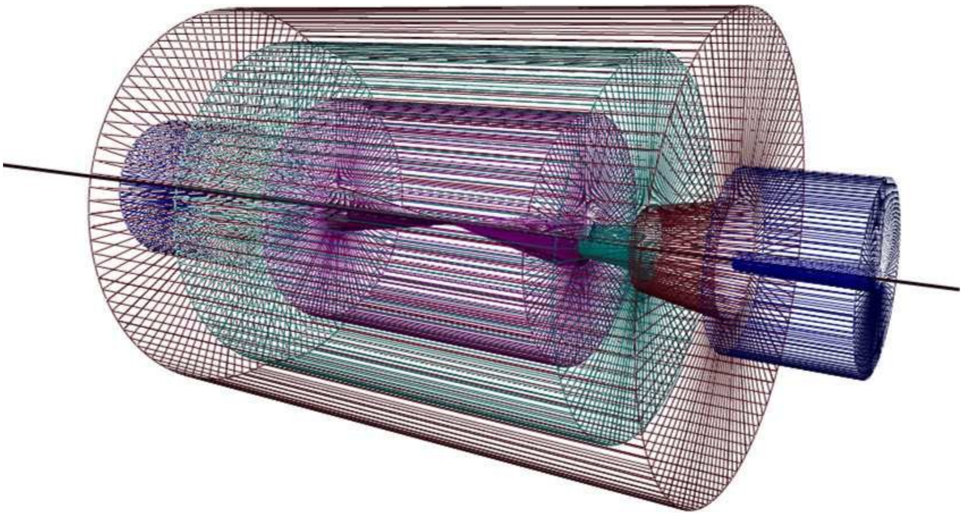

Figure 3.1: General purpose detector simulation in Delphes; inner tracker is in purple, calorimeters in green, muon system in brown and forward calorimeters in blue [97].

Tracker

The first step of the simulation is the propagation of particles within a uniform magnetic field in the tracker volume:

- a neutral particle follows a straight line trajectory from its production point to a calorimeter cell;
- a charged particle, instead, has a helicoidal trajectory.

User defined parameters are energy and momentum resolutions and tracking reconstruction efficiency as a function of transverse momentum ad pseudo-rapidity.

Calorimeters

Calorimeters have a finite segmentation in pseudo-rapidity and azimuthal angle (η, ϕ); for computational reason, the same granularity is assumed for both ECAL and HCAL. The two sections of the calorimeter are simulated to be perfectly superimposed: a particle reaching one ECAL cell reaches exactly one cell in the HCAL volume. The coordinate of the energy deposit, the so-called *tower*, is assumed to be the center of the cell.

Each particle leaves a fraction of its energy in the electromagnetic and hadronic volume, with a ratio of the two signals given by two user defined values, namely f_{ECAL} and f_{HCAL}. Default values are different according to the type of the particle:

- electrons and photons leave all their energy in ECAL, so $f_{\text{ECAL}} = 1$;
- hadrons are assumed to deposit energy in the HCAL only, so $f_{\text{HCAL}} = 1$;
- kaons and Λ are considered as stable particles, with $f_{\text{HCAL}} = 0.3$ and $f_{\text{ECAL}} = 0.7$, according to their dominant decays;
- muons and neutrinos do not deposit energy neither in ECAL nor in HCAL.

The resolutions of HCAL and ECAL are indipendently parametrized following the formula:

$$\left(\frac{\sigma}{E}\right)^2 = \underbrace{\left(\frac{S(\eta)}{\sqrt{E}}\right)^2}_{\textit{stochastic}} + \underbrace{\left(\frac{N(\eta)}{E}\right)^2}_{\textit{noise}} + \underbrace{C(\eta)^2}_{\textit{constant}} \tag{3.1}$$

Moreover, energy deposits are smeared by a log-normal distribution and the final tower energy is computed as:

$$E_{\text{Tower}} = \sum_{\text{particles}} \ln\mathcal{N}(f_{\text{ECAL}} \cdot E, \sigma_{\text{ECAL}}(E,\eta)) + \ln\mathcal{N}(f_{\text{HCAL}} \cdot E, \sigma_{\text{HCAL}}(E,\eta)) \tag{3.2}$$

where σ_{ECAL} and σ_{HCAL} are resolutions calculated from (3.1) and the sum runs over all particles reaching one tower.

Particle-Flow

In Delphes a simplified approach based on tracking system and calorimeters is adopted to implement the Particle-Flow (PF) event reconstruction.

Charged particles momenta are always estimated using information from the tracking system, even if in a real experiment the tracker resolution is better than the calorimeters one only under a certain threshold.

PF algorithm produces two collections of 4-vectors, namely *particle-flow tracks* and *particle-flow towers*, according to a procedure which starts with:

- E_{ECAL} and E_{HCAL}, the energy deposits in calorimeter volumes;
- $E_{\mathrm{ECAL},trk}$ and $E_{\mathrm{HCAL},trk}$, the total energy deposited respectively in ECAL and HCAL associated with a charged reconstructed particle.

From them, two quantities are defined:

$$\Delta_{\mathrm{ECAL}} = E_{\mathrm{ECAL}} - E_{\mathrm{ECAL},trk} \qquad \Delta_{\mathrm{HCAL}} = E_{\mathrm{HCAL}} - E_{\mathrm{HCAL},trk} \tag{3.3}$$

and $E^{\mathrm{eflow}}_{\mathrm{Tower}}$ is computed from:

$$E^{\mathrm{eflow}}_{\mathrm{Tower}} = \max(0, \Delta_{\mathrm{ECAL}}) + \max(0, \Delta_{\mathrm{HCAL}}) \tag{3.4}$$

From these values:

- a *particle-flow track* is associated to each reconstructed track;
- if $E^{\mathrm{eflow}}_{\mathrm{Tower}} > 0$, a *particle-flow tower* is created with $E = E^{\mathrm{eflow}}_{\mathrm{Tower}}$.

3.2.2 Object reconstruction

The object reconstruction and identification is performed with a series of approximations in order to maintain a fast procedure but good resolution. An important feature has to be emphasized: no fake rate is implemented for electrons, muons and photons in DELPHES.

Muons

A muon ($\mu^{\pm}$) originating from the interaction is reconstructed according to a user-defined tracking efficiency inside the tracker acceptance with a p_{T} higher than a certain threshold. A Gaussian smearing is applied to the initial p_{T} value to obtain the final muon momentum, with a resolution defined by the user.

Electrons

The same procedure as the one followed for muons is applied to electron ($e^{\pm}$) reconstruction, but combining tracker and electromagnetic calorimeter information. At low energy, tracker resolution is dominant while at high energy the ECAL one dominates.

Photons

Photons recontruction in fully based on the ECAL information, with the approximation that the photon pair production ($\gamma \to e^+e^-$) is neglected. The final photon energy is computed starting from the generated value and applying the ECAL resolution previously defined in (3.1). It is important to underline that true electrons with no reconstructed tracks are also classified as photons.

Isolation

An important parameter for the detection of the leptons (muons or electrons) arising from the Higgs boson decay is the *isolation*: an electron, a muon or a photon is isolated if it is not surrounded by other particles. In DELPHES the definition of isolation is based on considering a cone of radius R around the particle; the quantity isolation I of a particle P, $I(P)$, is computed as:

$$I(P) = \frac{\sum_{i \neq P} p_{\mathrm{T}}^{\mathrm{charged}}(i) + \max[\sum_{i \neq P} p_{\mathrm{T}}^{\mathrm{neutral}}(i) - I_C, 0]}{p_{\mathrm{T}}(P)} \tag{3.5}$$

and I_C is the pile-up subtraction, applied only to neutral particles, defined as:

$$I_C = \frac{\rho \cdot \pi R^2}{p_{\mathrm{T}}(P)} \tag{3.6}$$

with ρ indicating the pile-up density, which can be computed trhough the FASTJET package [98].

The particle is considered isolated if $I(P) < I_{\mathrm{min}}$, where the threshold I_{min} as well the cone radius R and $p_{\mathrm{T}}^{\mathrm{min}}$ are user-defined.

Jets

In DELPHES, jets can be produced starting from different input collections:

- **generated jets** are clustered from generator-level particles obtained after parton-shower and hadronization;

- **calorimeter jets** are made from towers (described in Section 3.2.1);

- **particle-flow jets** are obtained from clustering PF-tracks and PF-towers (described in Section 3.2.1).

The FastJet package is included, allowing jet recontruction with the most popular algorithms (the anti-$\mathrm{k_T}$ is used in this thesis) developed for high energy particle physics.

The identification of τ jets or b jets is achieved with the following procedure:

- a jet is labelled as b or τ jet candidate if a generated b or τ is found within a distance ΔR from the jet axis, with

$$\Delta R = \sqrt{(\eta^{\mathrm{jet}} - \eta^{\mathrm{b},\,\tau})^2 - (\phi^{\mathrm{jet}} - \phi^{\mathrm{b},\,\tau})^2} \tag{3.7}$$

- a user-defined tagging efficiency (including mis-tagging rate, that is the probability that a particle different from b or τ is indentified as a b or a τ) is applied to obtain a tagged reconstructed jet.

Missing tranverse energy and scalar transverse energy

The definitions of missing transverse energy and scalar trasnverse energy are, respectively,

$$\vec{E}_{\mathrm{T}}^{\mathrm{miss}} = -\sum_i \vec{p}_{\mathrm{T}}(i) \qquad H_{\mathrm{T}} = -\sum_i |\vec{p}_{\mathrm{T}}(i)| \tag{3.8}$$

with i running over all the selected input collections.

Chapter 4

HH→ b$\bar{\text{b}}$ZZ(4ℓ) analysis for HE-LHC

The analysis to evaluate the Higgs boson self-coupling measurement at the HE-LHC is performed considering the HH→ b$\bar{\text{b}}$ZZ(4ℓ) channel, where $\ell = e, \mu$. Despite its small $\sigma \times BR$ (0.02 fb at $\sqrt{s} = 27$ TeV) this channel provides a clear final state signature thanks to the presence of two b jets associated with four isolated leptons, allowing a good signal to background discrimination.

4.1 Signal and background processes

The analysis is performed considering three different final states:

- $b\bar{b}4\mu$;
- $b\bar{b}4e$;
- $b\bar{b}2e2\mu$.

The signal process is generated at $\sqrt{s} = 27$ TeV at the leading order (LO) considering only the gluon-gluon fusion production mechanism. In addition to the SM scenario (with $\kappa_\lambda = \lambda_3/\lambda_3^{\text{SM}} = 1$), BSM signal samples with different κ_λ are simulated, as described in Section 4.4.

The background processes taken into account are t$\bar{\text{t}}$H, t$\bar{\text{t}}$Z, ggH, ZH, t$\bar{\text{t}}$ZZ, Higgs production via vector-boson fusion (VBF), and WH. All signal and background samples (except for VBF and ggH) are generated at LO using MadGraph5_aMC@NLO; the hadronization and detector response (in the CMS Phase-II configuration) are simulated with Pythia8 and Delphes, respectively, with an average number of PU events of 200.

The VBF and ggH contributions are rescaled from the results obtained in the HL-LHC scenario [37, 99], taking into account the different values of integrated luminosity and cross sections between HL-LHC and HE-LHC:

$$\text{yield (HE)} = \text{yield (HL)} \cdot \frac{\sigma_{\mathrm{HE}}}{\sigma_{\mathrm{HL}}} \cdot \frac{L_{\mathrm{HE}}}{L_{\mathrm{HL}}} \tag{4.1}$$

This choice is justified because the event selection efficiency both for signal and background obtained in the HE scenario is comparable with the HL one, as shown in Table 4.1.

	HE-LHC	HL-LHC
4μ	0.03	0.03
$4e$	0.006	0.006
$2e2\mu$	0.02	0.02
4ℓ	0.08	0.06

Table 4.1: Selection efficiency in the HE and HL scenarios.

The theoretical $\sigma \times BR$ of the simulated processes both in the HE-LHC and in the HL-LHC scenario are summarized in Table 4.2. For the $\mathrm{t\bar{t}Z}$ and $\mathrm{t\bar{t}ZZ}$ channel, no theoretical calculations exist for the HE-LHC scenario, thus their values are taken from the MadGraph5_aMC@NLO simulations.

Top quark production and Drell-Yan (DY) lepton pair production in association to jets are a reducible background for the analysis which however are not included in this work for two main reasons:

- their estimation is very difficult due to the limited size of MC samples available;
- large suppressions are expected thanks to reconstruction techniques and performance in the rejection of fake and non-prompt leptons that are not optimized in the Delphes simulation.

process	$\sigma \times$ BR [fb] @$\sqrt{s}$ = 14 TeV	$\sigma \times$ BR [fb] @$\sqrt{s}$ = 27 TeV
gg $\rightarrow$ HH $\rightarrow$ b$\bar{\text{b}}$ZZ(4ℓ)	0.0053	0.02
t$\bar{\text{t}}$H, H $\rightarrow$ ZZ(4ℓ)	0.076	0.358
t$\bar{\text{t}}$Z, Z $\rightarrow$ 2ℓ	69.224	207.876
ZH, Z $\rightarrow$ b$\bar{\text{b}}$, H $\rightarrow$ 4ℓ	0.018	0.047
WH, H $\rightarrow$ 4ℓ	0.188	0.425
t$\bar{\text{t}}$ZZ, Z $\rightarrow$ 2ℓ	0.0078	0.0383
gg(H), H $\rightarrow$ $4\ell, \ell = e, \mu, \tau$	15.007	40.592
VBF(H), H $\rightarrow$ $4\ell, \ell = e, \mu, \tau$	1.169	3.277

Table 4.2: Cross section times branching ratio for signal and background processes in both the HE-LHC and the HL-LHC scenario [100, 101]. In the Table, $\ell = e, \mu$ except where indicated.

4.2 Event selection

The event selection in the HE-LHC scenario is performed following a cut-based analysis in order to identify events with two b jets and four leptons in the final state. First of all, the Z candidates are chosen considering the following steps:

- at least four identified leptons are required; they must be isolated (with $I(\ell) < 0.7$) and produced at pseudorapidity $|\eta| < 2.8$, with $p_{\mathrm{T}} > 5$ GeV for muons and $p_{\mathrm{T}} > 7$ GeV for electrons. Muons (electrons) are selected if passing the Loose (Medium) Working Point identification [102];
- Z boson candidates are formed from pairs of same flavour and opposite charge leptons, requiring an angular separation $\Delta R_{l^+l^-} > 0.02$;
- the lepton pair with the invariant mass closest to the nominal Z mass is labelled as Z_1, with a constraint on the invariant mass: $40 < M_{Z_1} < 120$ GeV;
- the second candidate is accepted only if its distance from Z_1 is $\Delta R_{Z_1 Z_2} > 0.05$ and its mass satisfies: $12 < M_{Z_2} < 120$ GeV; if more Z candidates are present, the one with the highest p_{T} is chosen;

- Among the four leptons selected (forming the two Z candidates) at least one leptons is required to have $p_{\mathrm{T}} > 10$ GeV and at least another lepton must have $p_{\mathrm{T}} > 20$ GeV.
- the four-lepton invariant mass, $M_{4\mathrm{l}}$, must be in the range $120 < M_{4\mathrm{l}} < 130$ GeV.

The other Higgs candidate is selected analyzing hadronic reconstructed jets. Hadronic jets are reconstructed with a particle-flow algorithm, in which candidates are clustered using tracks and calorimeter deposits using the anti-k_{T} algorithm. The PileUp Per Particle Identification (PUPPI) algorithm [103] is applied for PU mitigation. Two or three b-tagged jets are required, reconstructed inside a cone of radius $R = 0.4$; a b tag Medium working point is assumed [104]. The invariant mass of the $b\bar{b}$ system must be in the range $80 \leq M_{\mathrm{b\bar{b}}} \leq 160$ GeV, while the angular distance between the two b jets in the range $0.5 < \Delta R_{\mathrm{b\bar{b}}} < 2.3$.

The distance between the two reconstructed Higgs bosons is required to be $\Delta R_{\mathrm{HH}} \geq 2.0$. Finally, a cut on the missing trasverse energy (MET) is applied, with the requirement that MET < 150 GeV.

The analysis selection is optimized thanks to the characteristics of some relevant distributions such as:

- the invariant mass of the two Z bosons, M_{Z_1} (Figure 4.1) and M_{Z_2} (Figure 4.2);
- the invariant mass of the pair of b jets, $M_{b\bar{b}}$ (Figure 4.3);
- the invariant mass of the four leptons, M_{4l} (Figure 4.4);
- the invariant mass of the di-Higgs system, M_{HH} (Figure 4.5);
- the angular distances between the two selected b jets, $\Delta R_{b\bar{b}}$ (Figure 4.6) and between the two H bosons, ΔR_{HH} (Figure 4.7);
- the missing transverse energy, MET (Figure 4.8).

The percentage of events passing each cut of the analysis are shown in Figures 4.9-4.10 for all the considered final states.

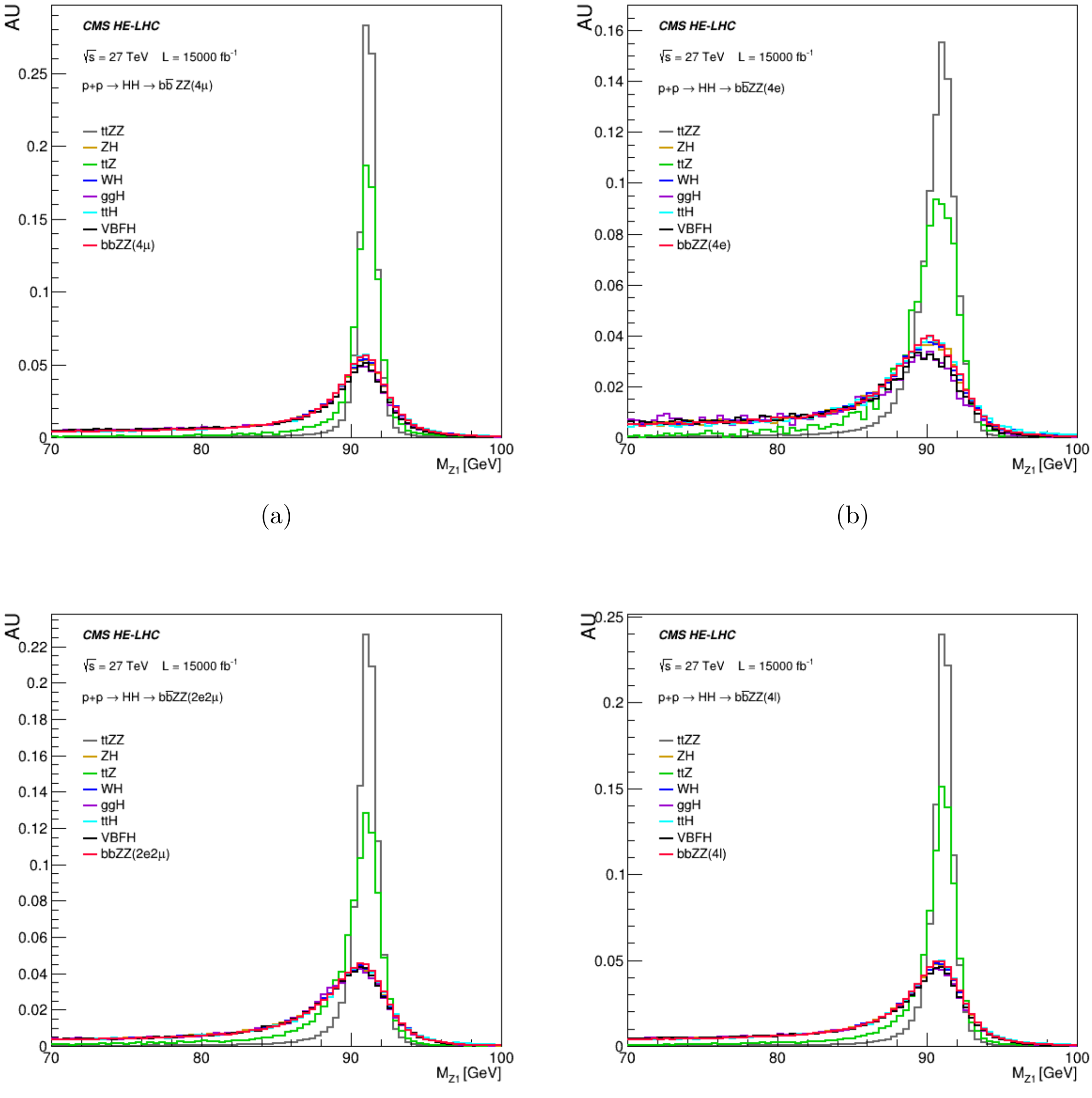

(a)

(b)

(c)

(d)

Figure 4.1: Invariant mass of the first Z boson for each final state: $b\bar{b}4\mu$ (a), $b\bar{b}4e$ (b), $b\bar{b}2e2\mu$ (c), $b\bar{b}4\ell$ (d). HH→ $\mathrm{b\bar{b}ZZ}$ signal process is in red.

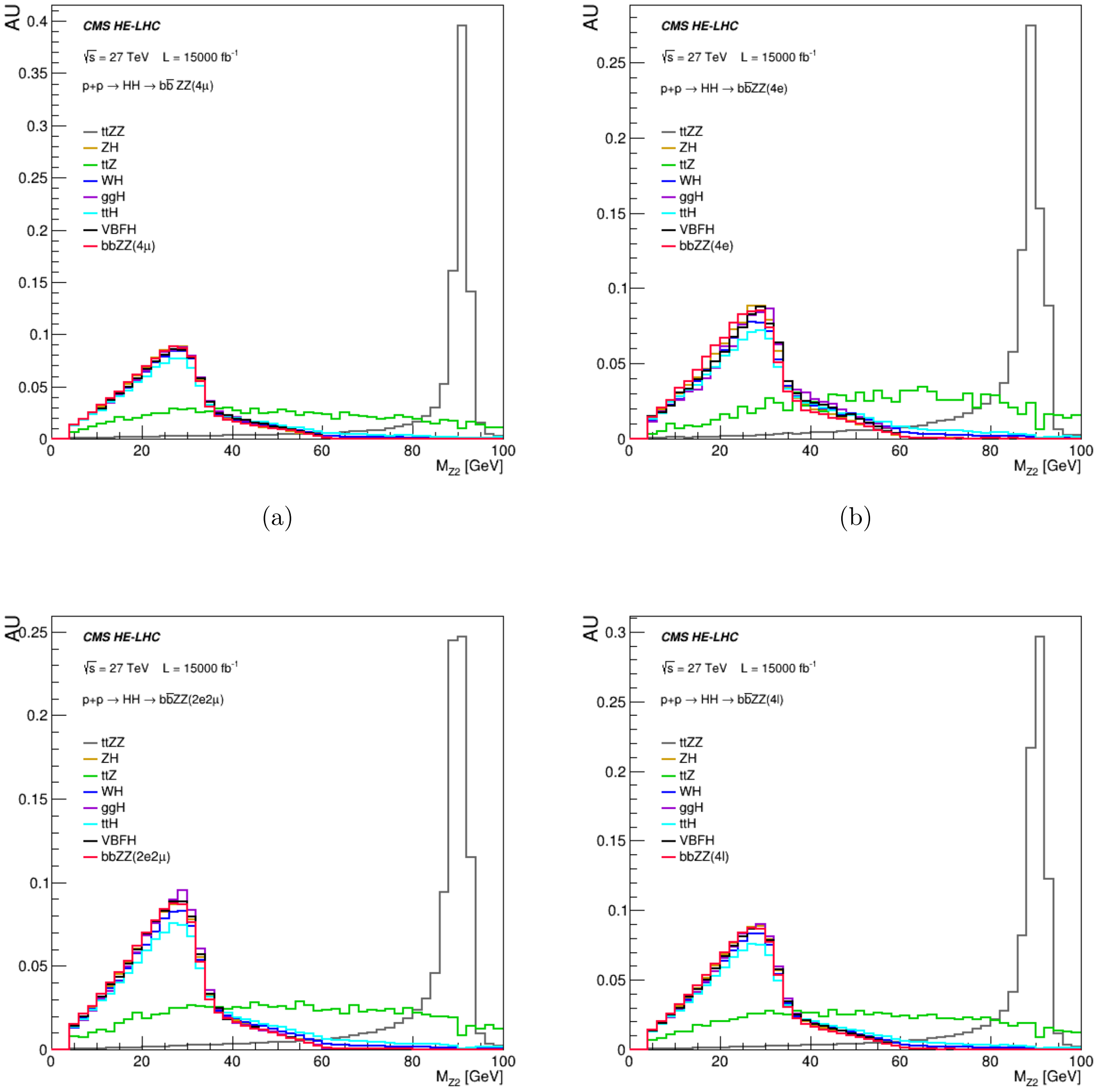

(a) (b)

(c) (d)

Figure 4.2: Invariant mass of the second Z boson for each final state: $b\bar{b}4\mu$ (a), $b\bar{b}4e$ (b), $b\bar{b}2e2\mu$ (c), $b\bar{b}4\ell$ (d). HH→ b$\bar{\text{b}}$ZZ signal process is in red.

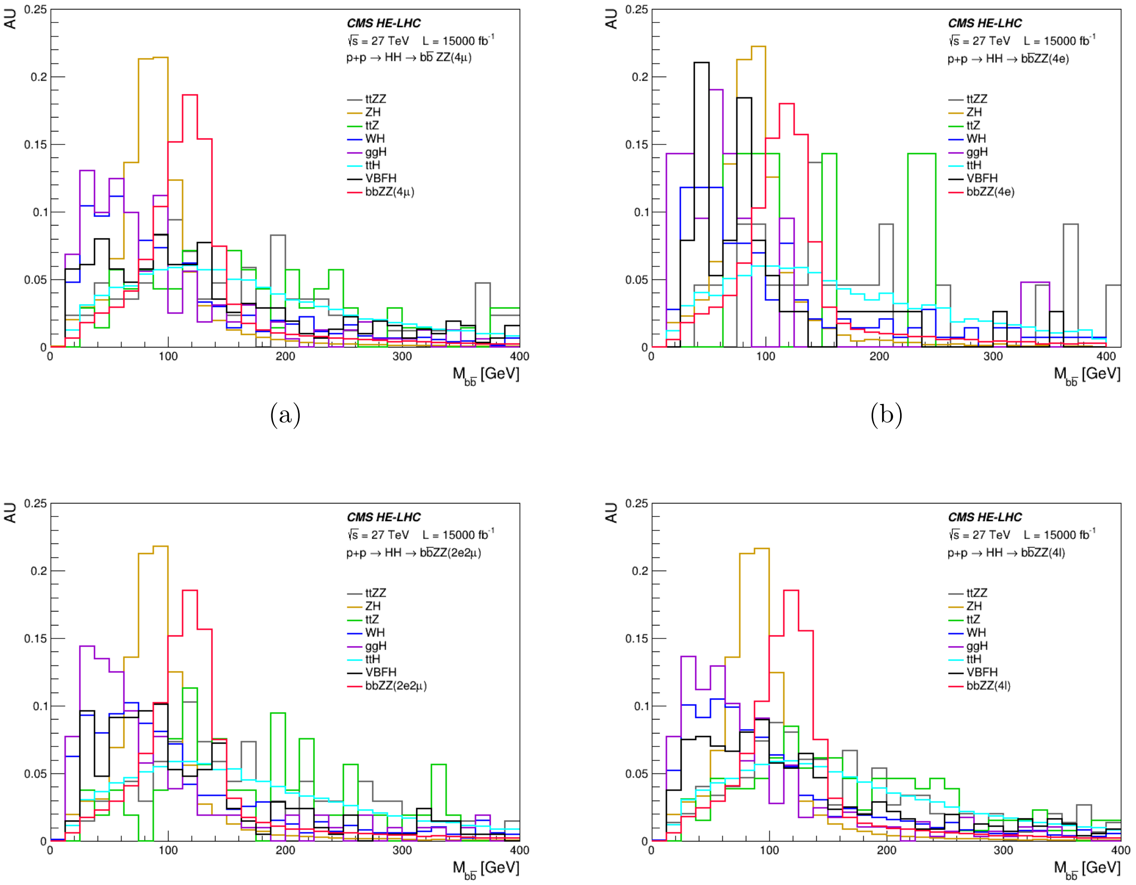

(a)

(b)

(c)

(d)

Figure 4.3: Invariant mass of the two b jets system for each final state: $b\bar{b}4\mu$ (a), $b\bar{b}4e$ (b), $b\bar{b}2e2\mu$ (c), $b\bar{b}4\ell$ (d). HH→ b$\bar{\text{b}}$ZZ signal process is in red.

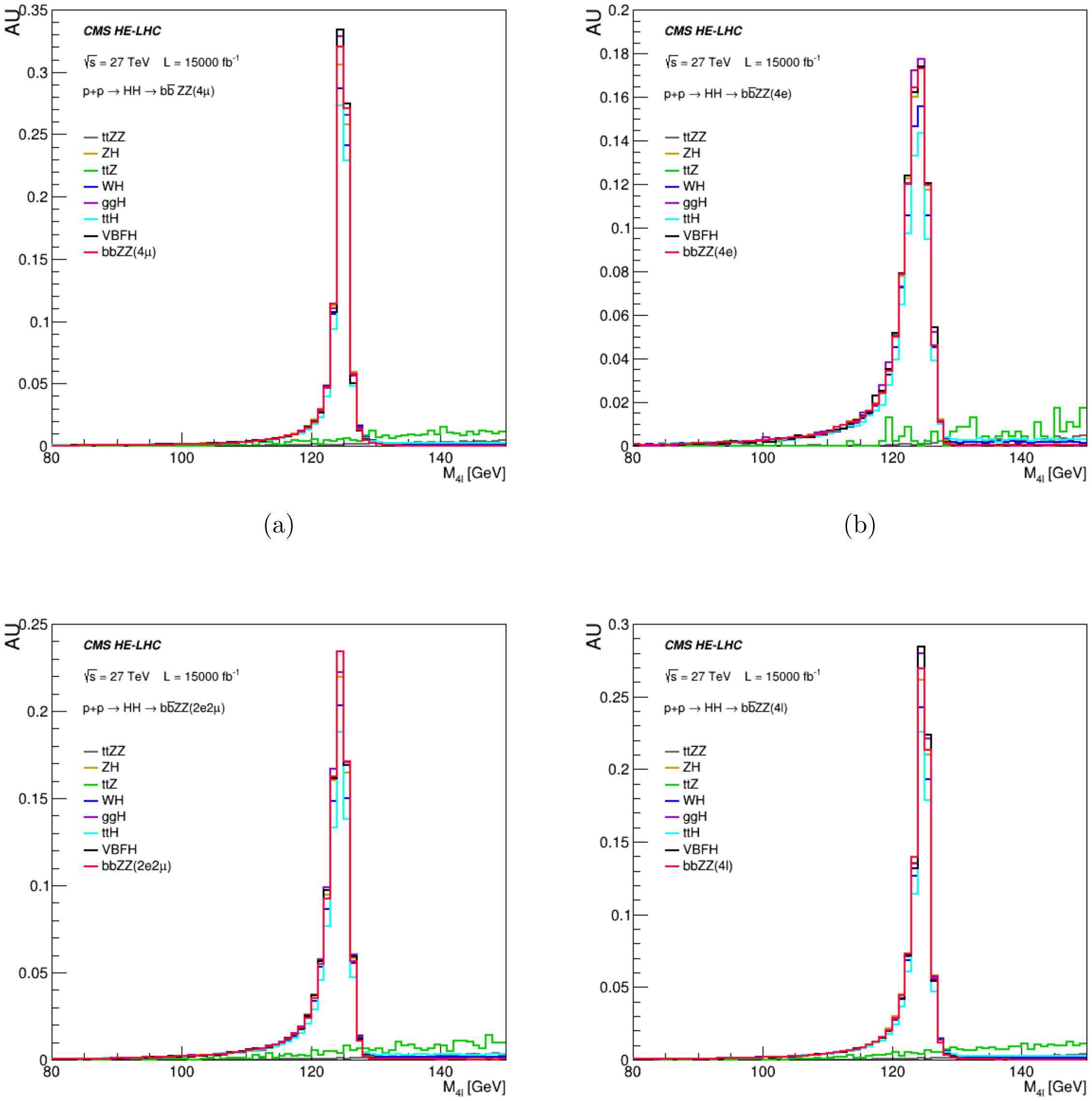

(a) (b)

(c) (d)

Figure 4.4: Invariant mass of the four leptons for each final state: $b\bar{b}4\mu$ (a), $b\bar{b}4e$ (b), $b\bar{b}2e2\mu$ (c), $b\bar{b}4\ell$ (d). HH→ b$\bar{\text{b}}$ZZ signal process is in red.

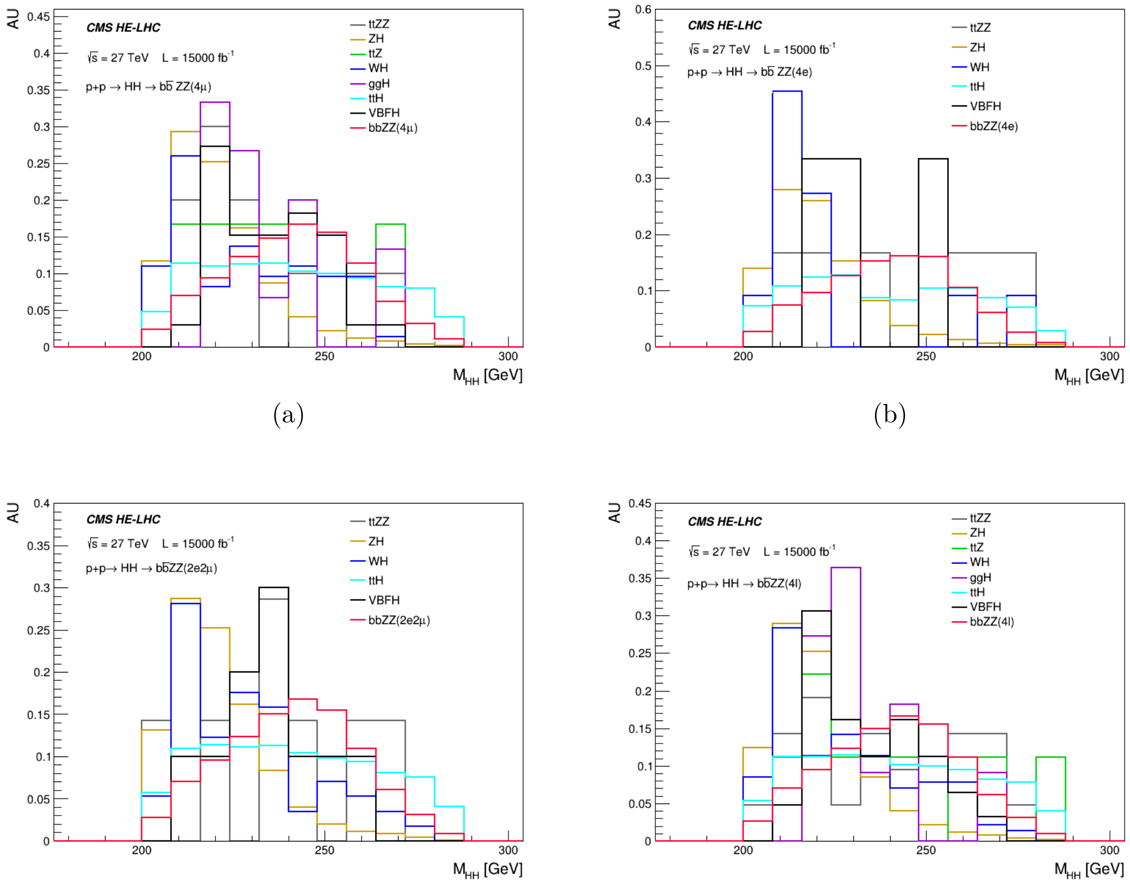

(a) (b)

(c) (d)

Figure 4.5: Invariant mass of the di-Higgs system for each final state: $b\bar{b}4\mu$ (a), $b\bar{b}4e$ (b), $b\bar{b}2e2\mu$ (c), $b\bar{b}4\ell$ (d). HH→ b$\bar{\text{b}}$ZZ signal process is in red.

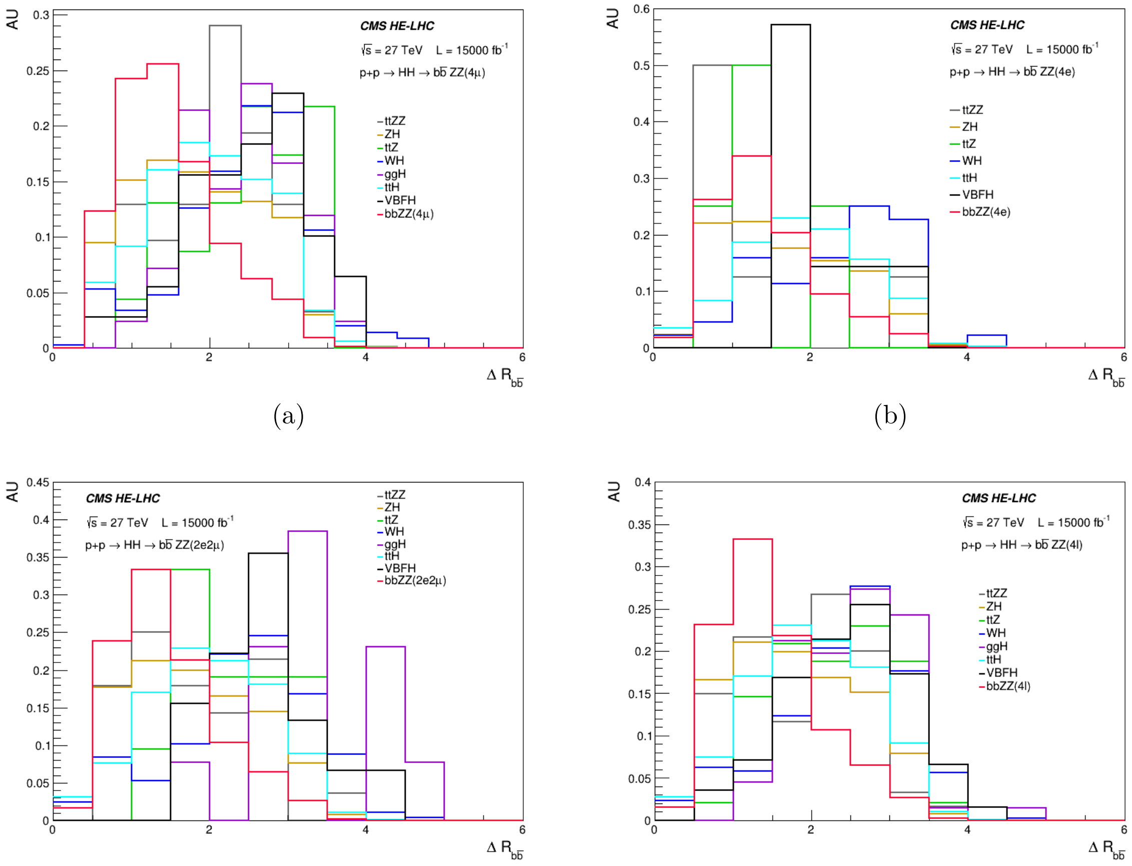

(a) (b) (c) (d)

Figure 4.6: Angular distance between the two b jets for each final state: $b\bar{b}4\mu$ (a), $b\bar{b}4e$ (b), $b\bar{b}2e2\mu$ (c), $b\bar{b}4\ell$ (d). HH→ b$\bar{\text{b}}$ZZ signal process is in red.

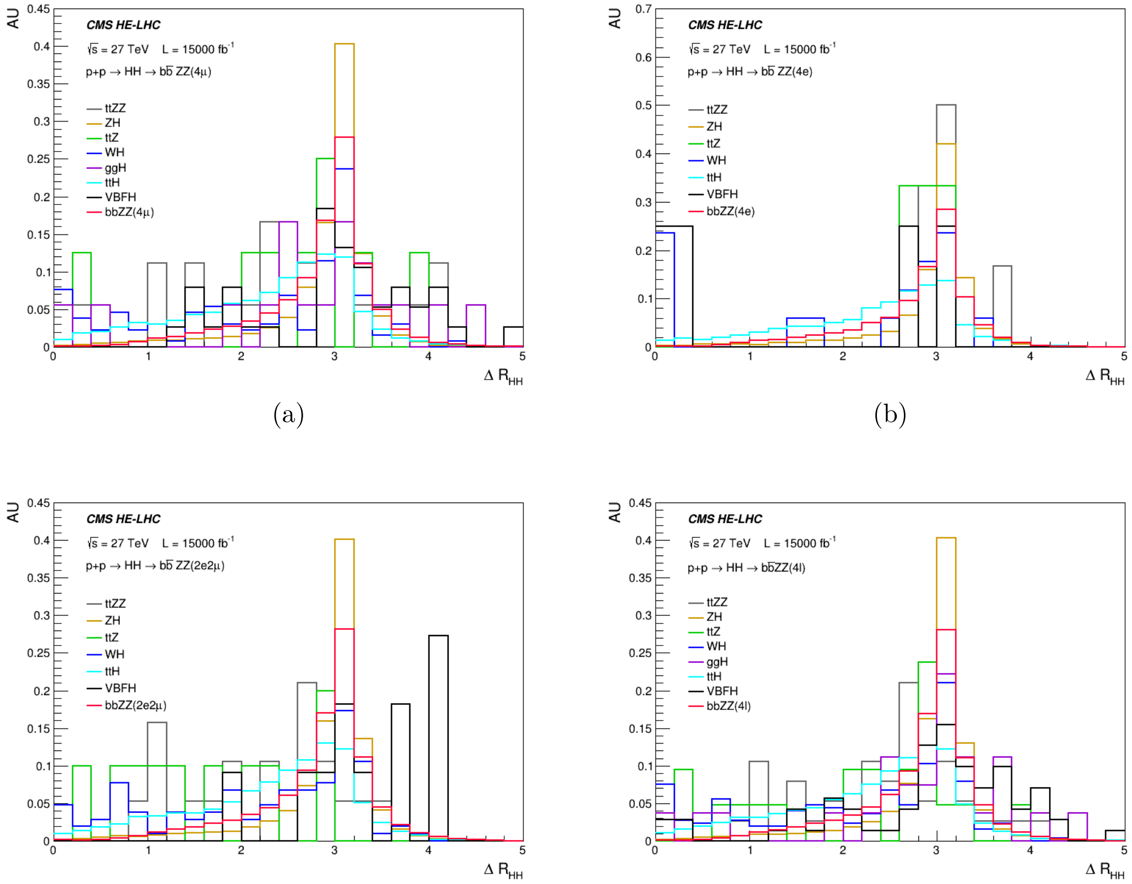

(a) (b)

(c) (d)

Figure 4.7: Angular distance between the two reconstructed Higgs bosons for each final state: $b\bar{b}4\mu$ (a), $b\bar{b}4e$ (b), $b\bar{b}2e2\mu$ (c), $b\bar{b}4\ell$ (d). HH→ b$\bar{\text{b}}$ZZ signal process is in red.

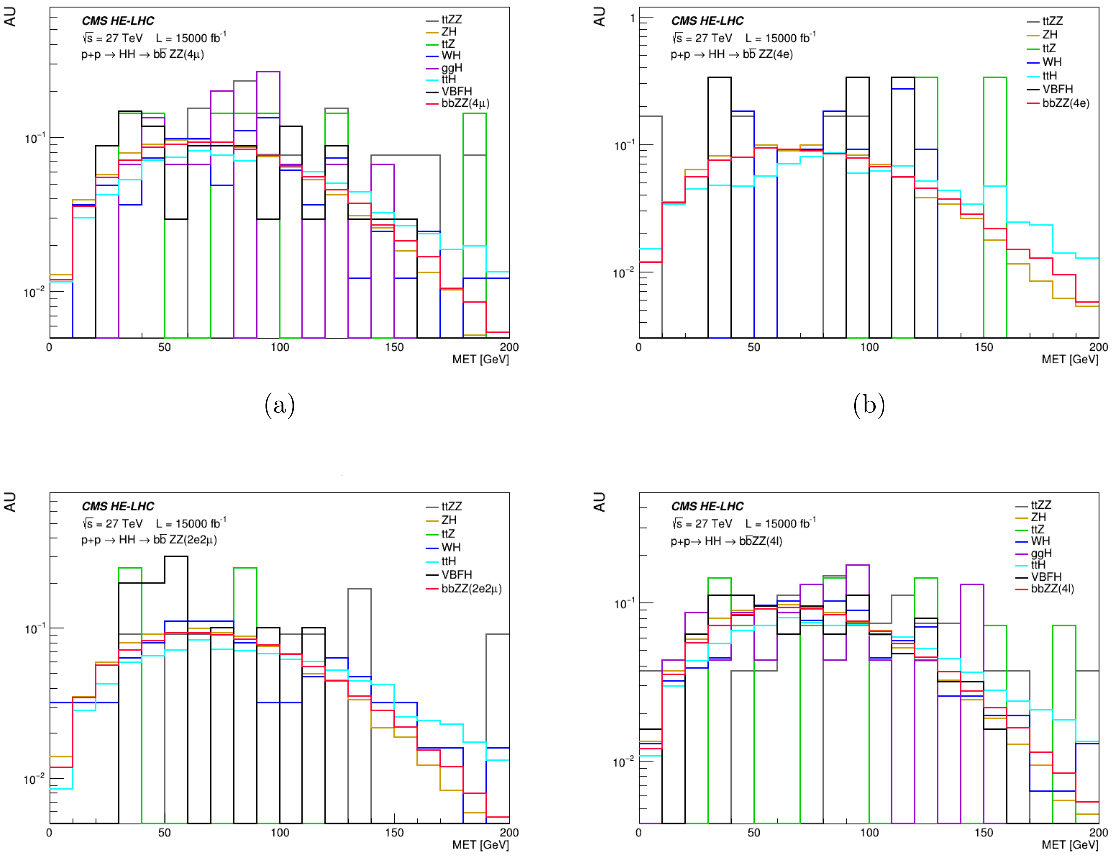

(a)

(b)

(c)

(d)

Figure 4.8: Logarithmic missing transverse energy (MET) for each final state: $b\bar{b}4\mu$ (a), $b\bar{b}4e$ (b), $b\bar{b}2e2\mu$ (c), $b\bar{b}4\ell$ (d). HH→ b$\bar{\text{b}}$ZZ signal process is in red.

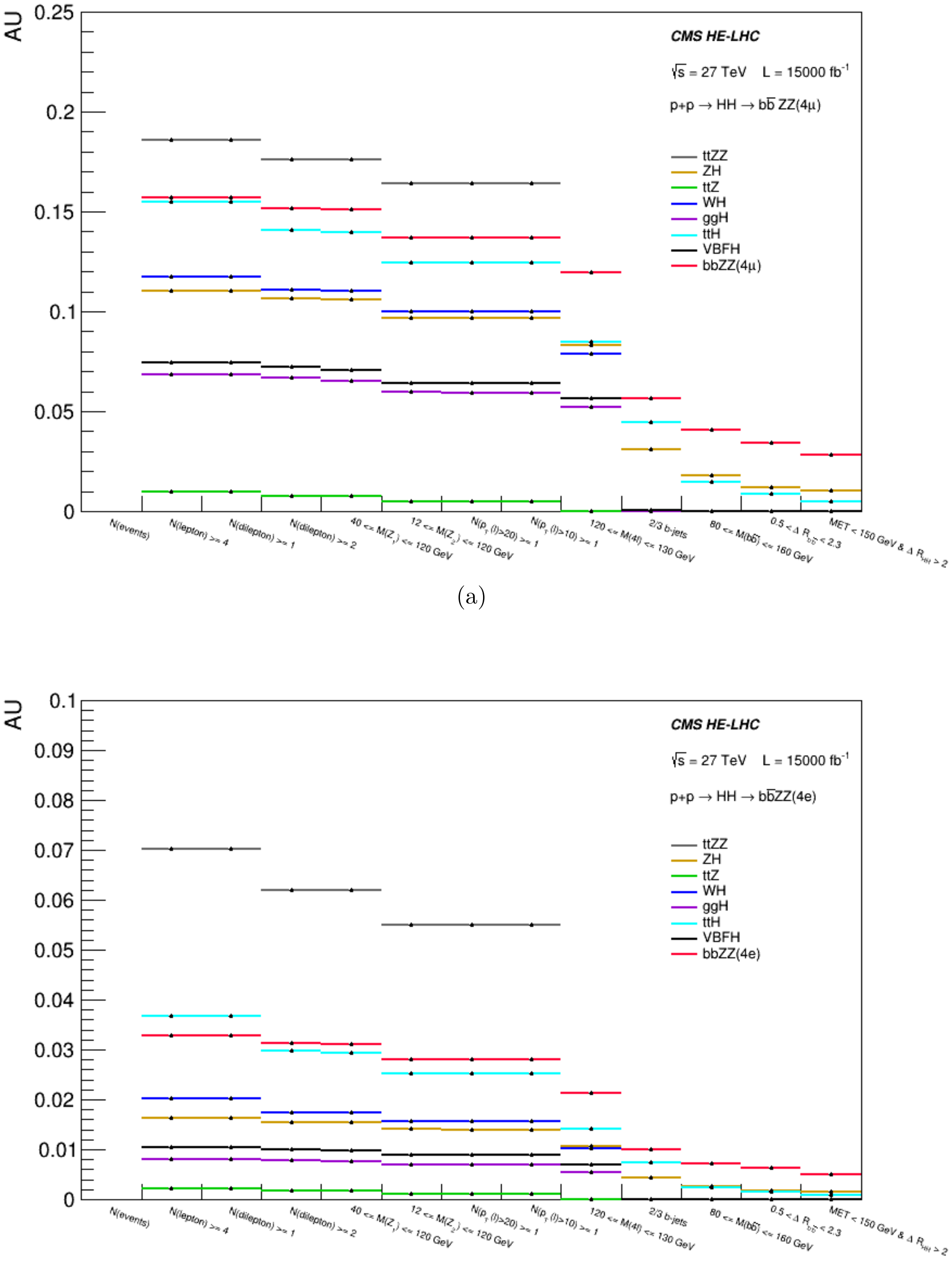

(b)

Figure 4.9: Percentage of events passing each step of the analysis for the $b\bar{b}4\mu$ (a) and $b\bar{b}4e$ (b) final states. HH→ b$\bar{\text{b}}$ZZ signal process is in red.

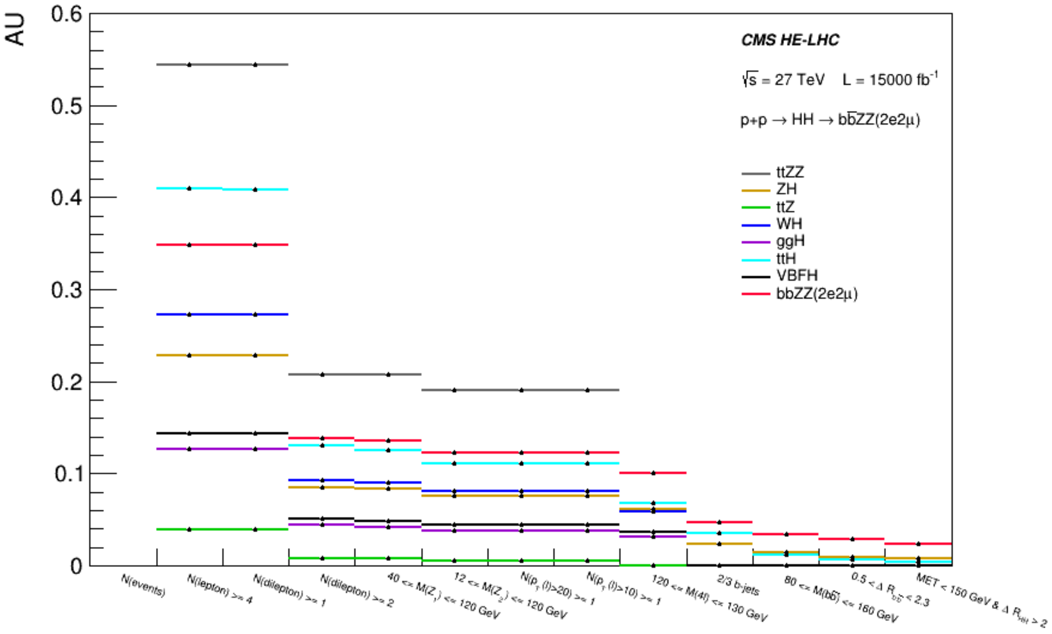

(a)

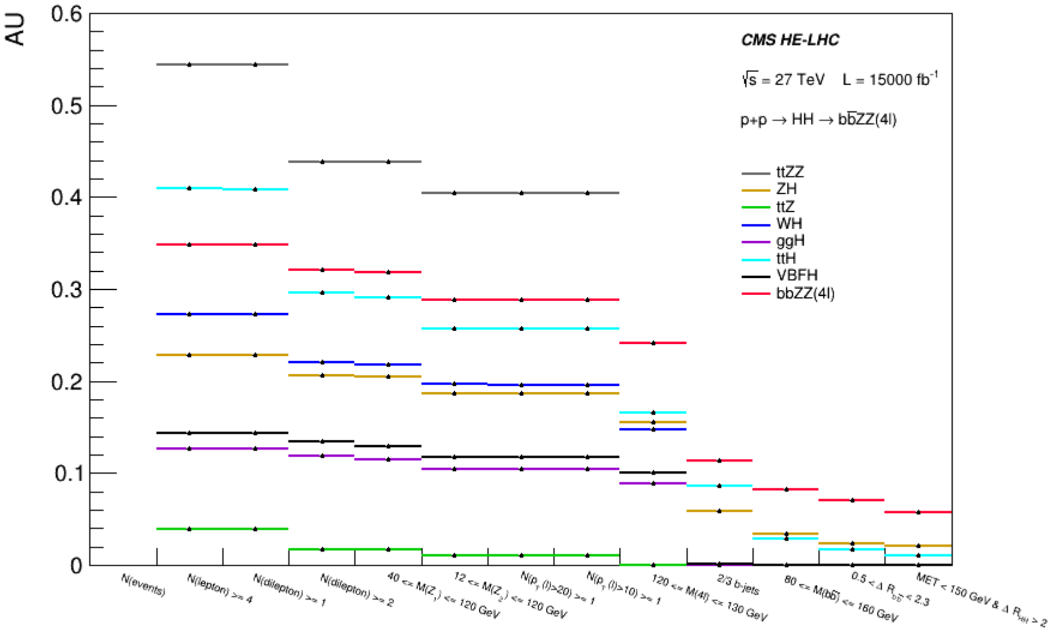

(b)

Figure 4.10: Percentage of events passing each step of the analysis for the $b\bar{b}2e2\mu$ (a) and $b\bar{b}4\ell$ (b) final states. HH→ b$\bar{\text{b}}$ZZ signal process is in red.

4.3 Results

After the full analysis selection, the expected yields in the HE-LHC scenario are obtained considering an integrated luminosity $L = 15000$ fb^{-1}. The results are shown in Table 4.3.

	$b\bar{b}4\mu$	$b\bar{b}4e$	$b\bar{b}2e2\mu$	$b\bar{b}4\ell$
HH	8.51	1.52	7.16	17.19
$\mathrm{t\bar{t}H}$	27.30	4.58	21.50	52.96
ggH	9.67	0.74	10.44	21.02
ZH	7.38	1.11	5.79	14.28
WH	0.26	0.04	0.20	0.50
VBFH	1.49	0.15	0.67	2.30
$\mathrm{t\bar{t}Z}$	10.65	1.78	3.55	15.97
$\mathrm{t\bar{t}ZZ}$	0.005	0.003	0.004	0.011

Table 4.3: Event yields for the signal and background processes for an integrated luminosity of 15000 fb^{-1}.

The invariant mass distributions of the four leptons after the full event selection is shown in Figure 4.11. The results show that the main background contribution is represented by the $\mathrm{t\bar{t}H}$ process, followed by $\mathrm{t\bar{t}Z}$, ggH, and ZH; minor contribution comes from VBFH, while WH and $\mathrm{t\bar{t}ZZ}$ are found to be negligible.

Since from the $\mathrm{t\bar{t}Z}$ background sample only few events satisfy all the requirements, leading to large uncertainties, its contribution is plotted considering a flat distribution (which is the one followed by the $\mathrm{t\bar{t}Z}$ events, to a first approximation) normalized to the expected yield, which is not negligible due to the large cross section.

The sensitivity of the HE-LHC scenario to the observation of a Higgs boson pair production in the $b\bar{b}4\ell$ channel is evaluated computing the signal strength $r = \sigma_{\mathrm{obs}}/\sigma_{\mathrm{SM}}$ using the statistical tool Combine [105]. The study is performed considering two different scenarios:

- statistical uncertainties only;
- statistical and systematic uncertainties;

The systematic uncertainties considered in this analysis are listed in Table 4.4. The uncertainties related to the detector performance are assumed to be the same recom-

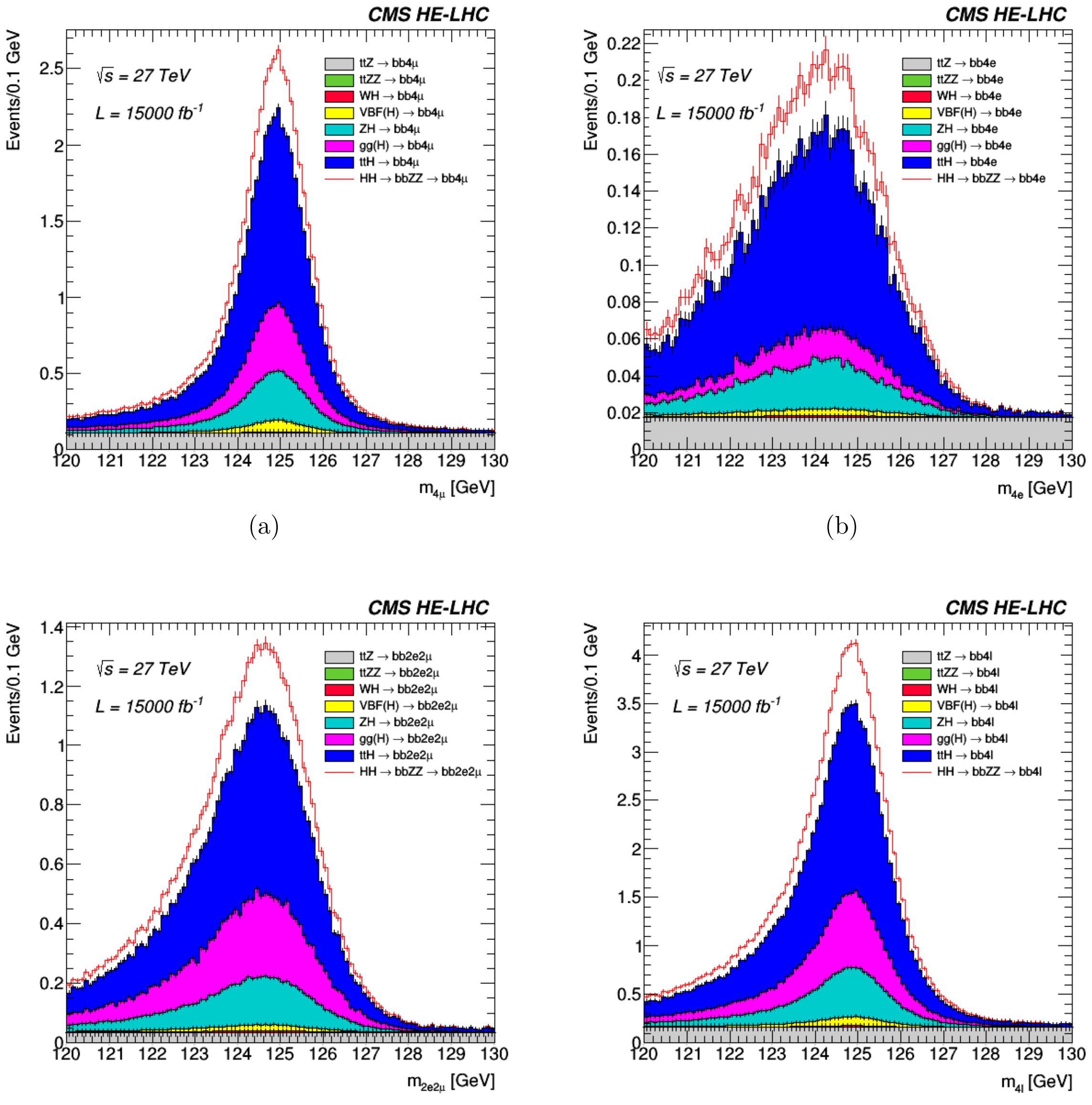
(a)

(b)

(c)

(d)

Figure 4.11: Invariant mass distributions of the four leptons selected at the end of the analysis for each final state: $b\bar{b}4\mu$ (a), $b\bar{b}4e$ (b), $b\bar{b}2e2\mu$ (c), $b\bar{b}4\ell$ (d).

mended for the HL-LHC scenario since the detector configuration is the same. For the theoretical uncertainties, the ones recommended at $\sqrt{s} = 27$ TeV are used.

The significance on the HH signal for each final state considered in this analysis is computed, as listed in Table 4.5, with values ranging from $\sim 0.5\,\sigma$ to $\sim 1.1\,\sigma$. Conservative

Luminosity	1.0%
Muon identification and isolation	0.5%
Electron identification and isolation	1.0%
b-tagging	2.0%
HH MC uncertainty	3.4%
HH PDF and α_s uncertainty	2.5%
$\mathrm{t\bar{t}H}$ QCD scale	$^{+7.8\%}_{-9.0\%}$
$\mathrm{t\bar{t}H}$ PDF and α_s	2.8%
WH QCD scale	$^{+0.29\%}_{-0.72\%}$
WH PDF and α_s	1.37%
ZH QCD scale	$^{+5.42\%}_{-4.00\%}$
ZH PDF and α_s	2.24%
$\mathrm{t\bar{t}Z}$ QCD scale	$^{+9.6\%}_{-11.2\%}$
$\mathrm{t\bar{t}Z}$ PDF	2.7%
$\mathrm{t\bar{t}Z}$ α_s	2.8%
ggH QCD scale	$^{+4.53\%}_{-6.43\%}$
ggH PDF	1.95%
ggH α_s	$^{+2.69\%}_{-2.64\%}$
VBF PDF and α_s	2.1%

Table 4.4: Systematic uncertainties [106, 107]

upper bounds at the 95% CL for the signal strength (listed in Table 4.6) are computed through the evaluation of the negative log-likelihood, which is shown in Figure 4.12 for each final state. As expected, the most sensitive channel is $b\bar{b}4\mu$; the presence of at least one pair of electrons, which are worstly reconstructed, leads to a lower significance and, thus, to a worse upper limit. The best results are obtained combining the three final states in the $b\bar{b}4\ell$ selection, where the signal strength is $r = 1.45$ ($r = 1.25$) and the significance is $1.43\,\sigma$ ($1.63\,\sigma$) considering statistical and systematic uncertainties (statistical uncertainty only).

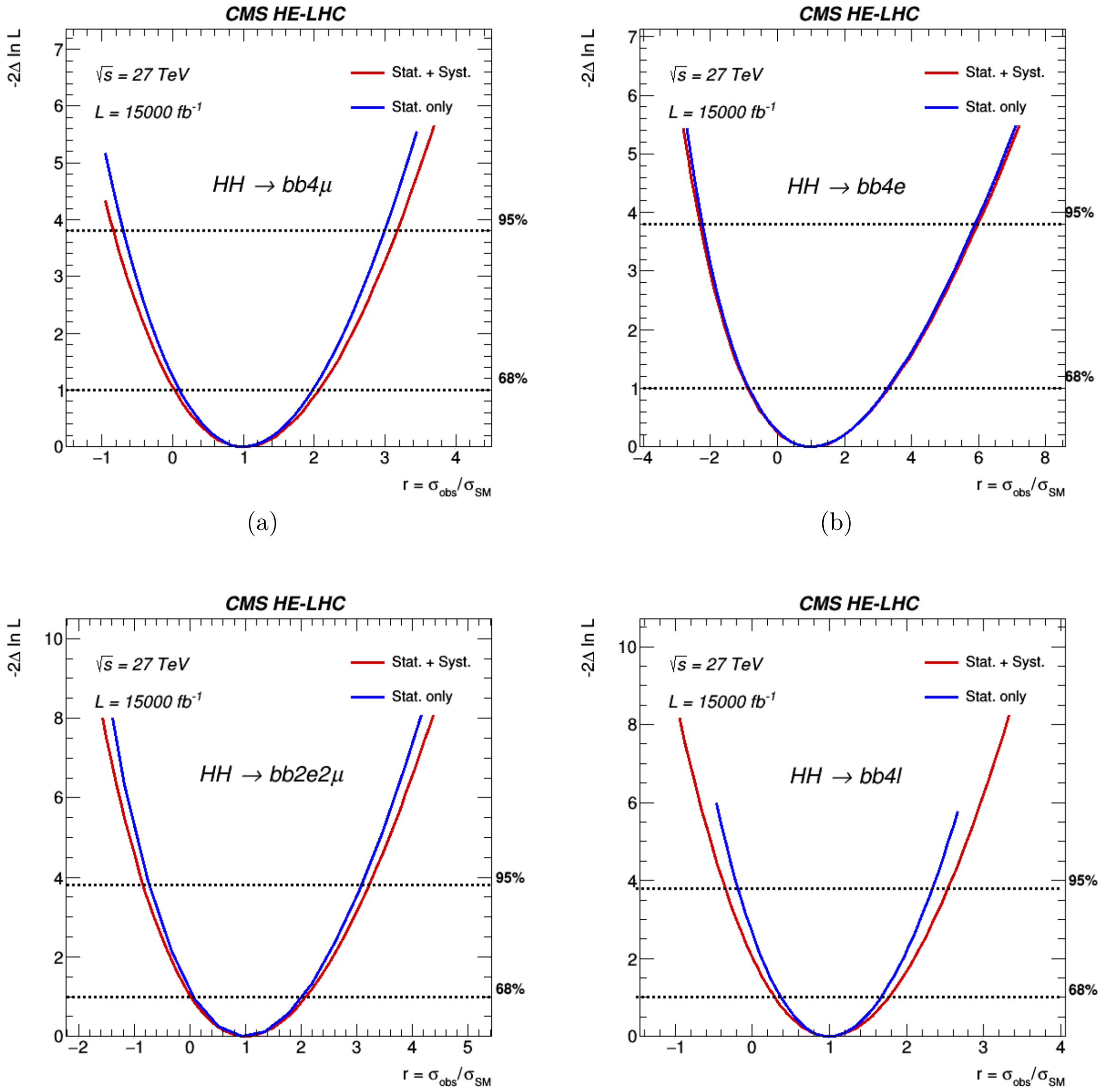

(a) (b)

(c) (d)

Figure 4.12: Expected likelihood scan as a function of the signal strength $r = \sigma_{\rm obs}/\sigma_{\rm SM}$ for each final state: $b\bar{b}4\mu$ (a), $b\bar{b}4e$ (b), $b\bar{b}2e2\mu$ (c), $b\bar{b}4\ell$ (d).

Uncertainty	$b\bar{b}4\mu$	$b\bar{b}4e$	$b\bar{b}2e2\mu$	$b\bar{b}4\ell$
Stat. only	1.11	0.51	1.08	1.63
Stat. + Syst.	1.03	0.50	1.02	1.43

Table 4.5: Significance on the HH signal in the HE-LHC scenario for each final state, considering statistical uncertainties only or both statistical and systematic uncertainties.

Uncertainty	$b\bar{b}4\mu$	$b\bar{b}4e$	$b\bar{b}2e2\mu$	$b\bar{b}4\ell$
Stat. only	1.88	4.61	1.95	1.25
Stat. + Syst.	2.04	4.69	2.08	1.45

Table 4.6: Limits at the 95% CL on the signal strength $r = \sigma_{\mathrm{obs}}/\sigma_{\mathrm{SM}}$ in the HE-LHC scenario, considering statistical uncertainties only or both statistical and systematic uncertainties.

4.4 Prospects of the measurement of λ_3

4.4.1 Description of the study

As previously mentioned, the production of a pair of Higgs bosons can be used to look for any deviations from SM predictions. In order to evaluate the sensitivity of the possible HE-LHC data-taking phase to BSM effects, the signal process is simulated with different values of the self-coupling modifier $\kappa_\lambda = \lambda_3/\lambda_3^{\mathrm{SM}}$, covering the range of values $-20 < \kappa_\lambda < 20$.

As for signal samples used in the SM scenario, these samples are generated with MadGraph5_aMC@NLO and the hadronization and the detector response are simulated with Pythia8 and Delphes, respectively.

The MadGraph5 software gives a cross section value at the leading order (LO). To take into account next-to-next leading order (NNLO) corrections on the values of the cross sections for each κ_λ, the following procedure is applied:

- a quadratic fit is performed on the cross section ratio:

$$\frac{(\sigma_{\mathrm{HH}}^{\mathrm{madgraph}}, \kappa_\lambda)}{(\sigma_{\mathrm{HH}}^{\mathrm{madgraph}}, \kappa_\lambda = 1)} \tag{4.2}$$

  obtaining a function of κ_λ:

$$r_{\mathrm{corr}}(\kappa_\lambda) = 0.243\kappa_\lambda^2 - 1.243\kappa_\lambda + 2.002 \tag{4.3}$$

- the rescaled value for the cross section at a given κ_λ is obtained by:

$$\sigma_{\mathrm{HH}}(\kappa_\lambda) = (\sigma_{\mathrm{HH}}^{\mathrm{theor}}, (\kappa_\lambda = 1)) \cdot r_{\mathrm{corr}}(\kappa_\lambda) \tag{4.4}$$

In Table 4.7 the cross sections times the BR($H \to b\bar{b}$) (because the simulation is performed forcing the decay of an Higgs boson into a pair of b quarks) for the considered κ_λ values are listed, before ($\sigma_{\mathrm{HH}}^{\mathrm{madgraph}}$) and after correction ($\sigma_{\mathrm{HH}}^{\mathrm{corrected}}$).

κ_λ	-20	-10	-7	-5	-3	-1	-0.5	0
$\sigma_{\mathrm{HH}}^{\mathrm{madgraph}}$	13.9	4.33	2.53	1.60	0.89	0.39	0.30	0.22
$\sigma_{\mathrm{HH}}^{\mathrm{corrected}}$	10.1	3.16	1.84	1.16	0.65	0.28	0.22	0.16
κ_λ	0.5	1	1.5	2	2.5	3	3.5	4
$\sigma_{\mathrm{HH}}^{\mathrm{madgraph}}$	0.16	0.11	0.08	0.05	0.05	0.05	0.07	0.10
$\sigma_{\mathrm{HH}}^{\mathrm{corrected}}$	0.12	0.08	0.06	0.04	0.03	0.04	0.05	0.07
κ_λ	4.5	5	5.5	6	7	10	15	20
$\sigma_{\mathrm{HH}}^{\mathrm{madgraph}}$	0.15	0.21	0.28	0.37	0.58	1.55	4.25	8.32
$\sigma_{\mathrm{HH}}^{\mathrm{corrected}}$	0.11	0.15	0.21	0.27	0.42	1.13	3.10	6.06

Table 4.7: $\sigma_{\mathrm{HH}} \times$ BR$(H \to b\bar{b})$ [pb] for the considered κ_λ values.

4.4.2 Results

Assuming that a HH signal exists with the properties predicted by the SM, the same cut-based analysis is performed to obtain, with the cross section computed by (4.4), the expected signal yields, reported in Table 4.8.

κ_λ	-20	-10	-7	-5	-3	-1	-0.5	0
Signal yield $b\bar{b}4\mu$	659.4	215.0	130.0	84.7	49.5	24.3	19.2	15.1
Signal yield $b\bar{b}4e$	96.6	34.2	20.7	13.5	8.20	3.98	3.22	2.59
Signal yield $b\bar{b}2e2\mu$	519.8	174.9	104.9	68.4	40.7	20.0	16.0	12.6
Signal yield $b\bar{b}4l$	1275	424.0	255.6	165.8	98.4	48.3	38.4	30.3
κ_λ	0.5	1	1.5	2	2.5	3	3.5	4
Signal yield $b\bar{b}4\mu$	11.5	8.51	6.13	4.37	3.24	2.68	2.75	3.42
Signal yield $b\bar{b}4e$	2.04	1.52	1.14	0.83	0.63	0.51	0.49	0.55
Signal yield $b\bar{b}2e2\mu$	9.70	7.16	5.26	3.84	2.83	2.33	2.31	2.77
Signal yield $b\bar{b}4l$	23.2	17.2	12.5	9.04	6.70	5.52	5.55	6.74
κ_λ	4.5	5	5.5	6	7	10	15	20
Signal yield $b\bar{b}4\mu$	4.77	6.67	9.17	12.2	20.3	59.5	172.3	348.9
Signal yield $b\bar{b}4e$	0.72	1.03	1.34	1.80	2.92	8.31	25.1	52.1
Signal yield $b\bar{b}2e2\mu$	3.75	5.18	7.12	9.51	16.0	45.7	135.1	274.4
Signal yield $b\bar{b}4l$	9.24	12.9	17.6	23.5	39.2	113.6	332.4	675.3

Table 4.8: Signal yields for the considered κ_λ values and for the four studied final state.

In oder to evaluate, through the statistical tool Combine, the negative log-likelihood on κ_λ, the signal yields of the κ_λ scans are plotted and fitted with a quadratic function as shown in Figure 4.13. The scan of the likelihood as a function of κ_λ coupling is shown in Figure 4.14.

In Table 4.9 the confidence intervals on κ_λ are reported for each final state.

Considering the inclusive channel $b\bar{b}4\ell$, the projected confidence interval on the coupling corresponds to $[-0.1, 6.4]$ at the 68% CL and to $[-0.7, 7.2]$ at the 95% CL.

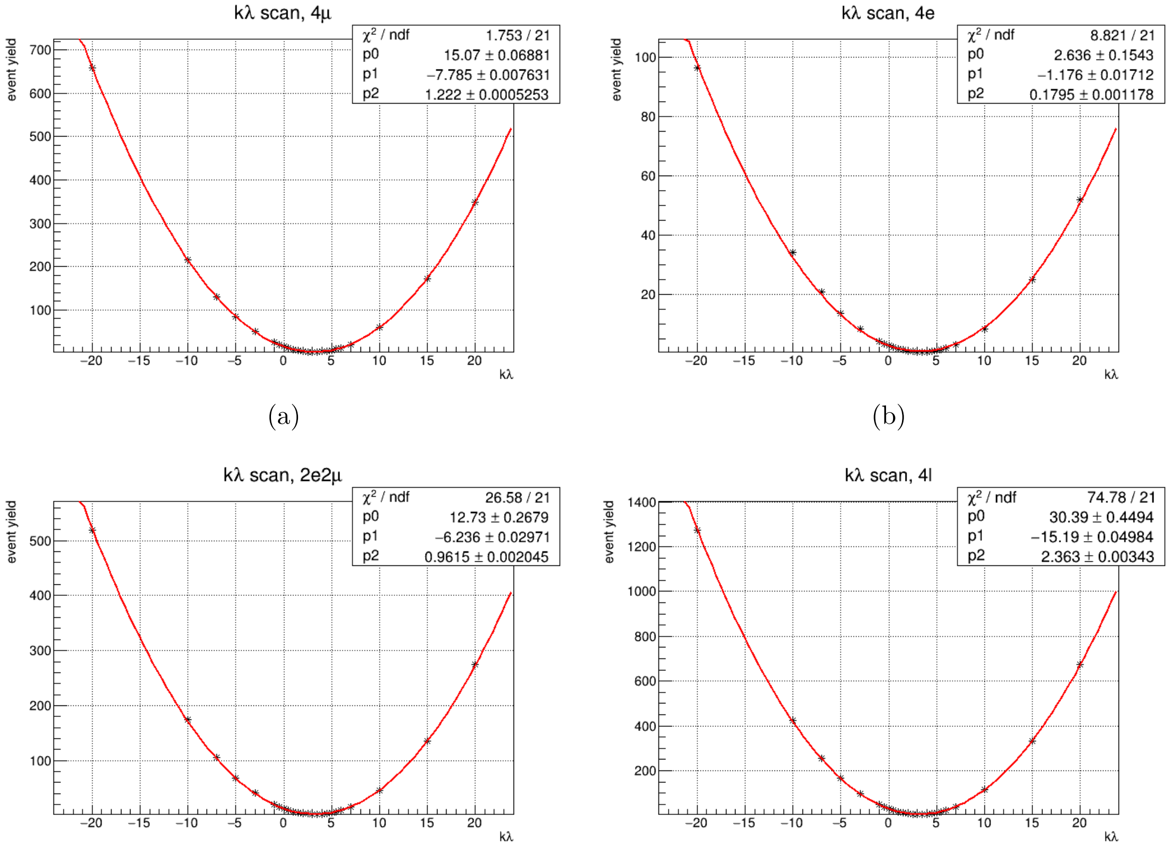

(a) (b)

(c) (d)

Figure 4.13: Quadratic fit of the signal yields as a funtion of κ_λ for each final state: $b\bar{b}4\mu$ (a), $b\bar{b}4e$ (b), $b\bar{b}2e2\mu$ (c), $b\bar{b}4\ell$ (d).

	68% CL	95% CL
$b\bar{b}4\mu$	$[-0.3, 6.7]$	$[-1.3, 7.7]$
$b\bar{b}4e$	$[-2.0, 8.3]$	$[-3.9, 10.5]$
$b\bar{b}2e2\mu$	$[-0.4, 6.9]$	$[-1.5, 8.0]$
$b\bar{b}4l$	$[-0.1, 6.4]$	$[-0.7, 7.2]$

Table 4.9: Confidence intervals on κ_λ for each final state.

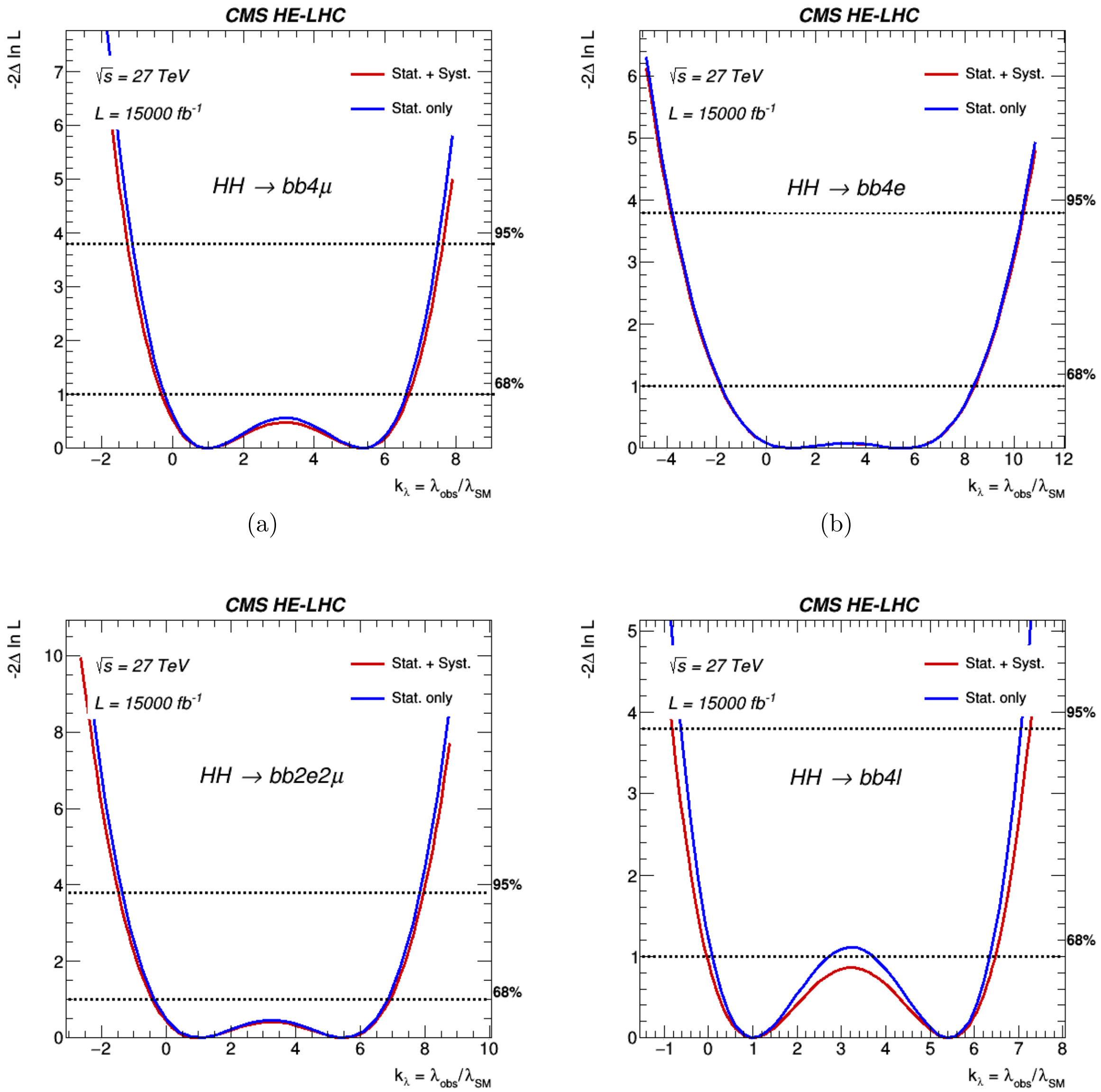

(a) (b)

(c) (d)

Figure 4.14: Expected likelihood scan as a function of the self-coupling modifier κ_λ for each final state: $b\bar{b}4\mu$ (a), $b\bar{b}4e$ (b), $b\bar{b}2e2\mu$ (c), $b\bar{b}4\ell$ (d).

4.5 Comparison with the High Luminosity LHC scenario results

The results of this thesis are compared to results obtained in the analysis performed in the HL-LHC scenario, which follows the same strategy [37, 99, 108] but with some different selection criteria:

- the Z boson candidates invariant mass constraints are: $50 < M_{Z_1} < 100$ GeV and $12 < M_{Z_2} < 60$ GeV;
- the $b\bar{b}$ invariant mass is required to be in the range $[90, 150]$ GeV. Moreover, an improvement of 20% in the resolution of the $m_{b\bar{b}}$ peak is assumed, as expected in the HL-LHC scenario thanks to better b jet energy reconstruction. This improvement is not considered in the HE-LHC scenario since no studies have been performed yet in this framework.

Improved results are achieved in the HE-LHC scenario with respect to the ones obtained in the HL-LHC. In Figure 4.15, the negative log-likelihood on the signal strength is plotted in both the HE-LHC and the HL-LHC frameworks, considering the results obtained with statistical and systematic uncertainties (which is the most conservative choice). A significance better by a factor $3 \div 5$ is reached, leading to lower upper limits at the 95% CL on the signal strength (the results for both scenarios are shown in Table 4.10).

	$b\bar{b}4\mu$	$b\bar{b}4e$	$b\bar{b}2e2\mu$	$b\bar{b}4\ell$
Significance HL-LHC	0.258	0.145	0.231	0.372
Significance HE-LHC	1.03	0.50	1.02	1.43
95% CL limits on r at HL-LHC	10.22	30.38	11.69	6.56
95% CL limits on r at HE-LHC	2.04	4.69	2.08	1.45

Table 4.10: Significance of the signal and limits at 95% CL on the signal strength $r = \sigma_{\text{obs}}/\sigma_{\text{SM}}$ in the HE-LHC and HL-LHC scenarios, considering both statistical and systematic uncertainties.

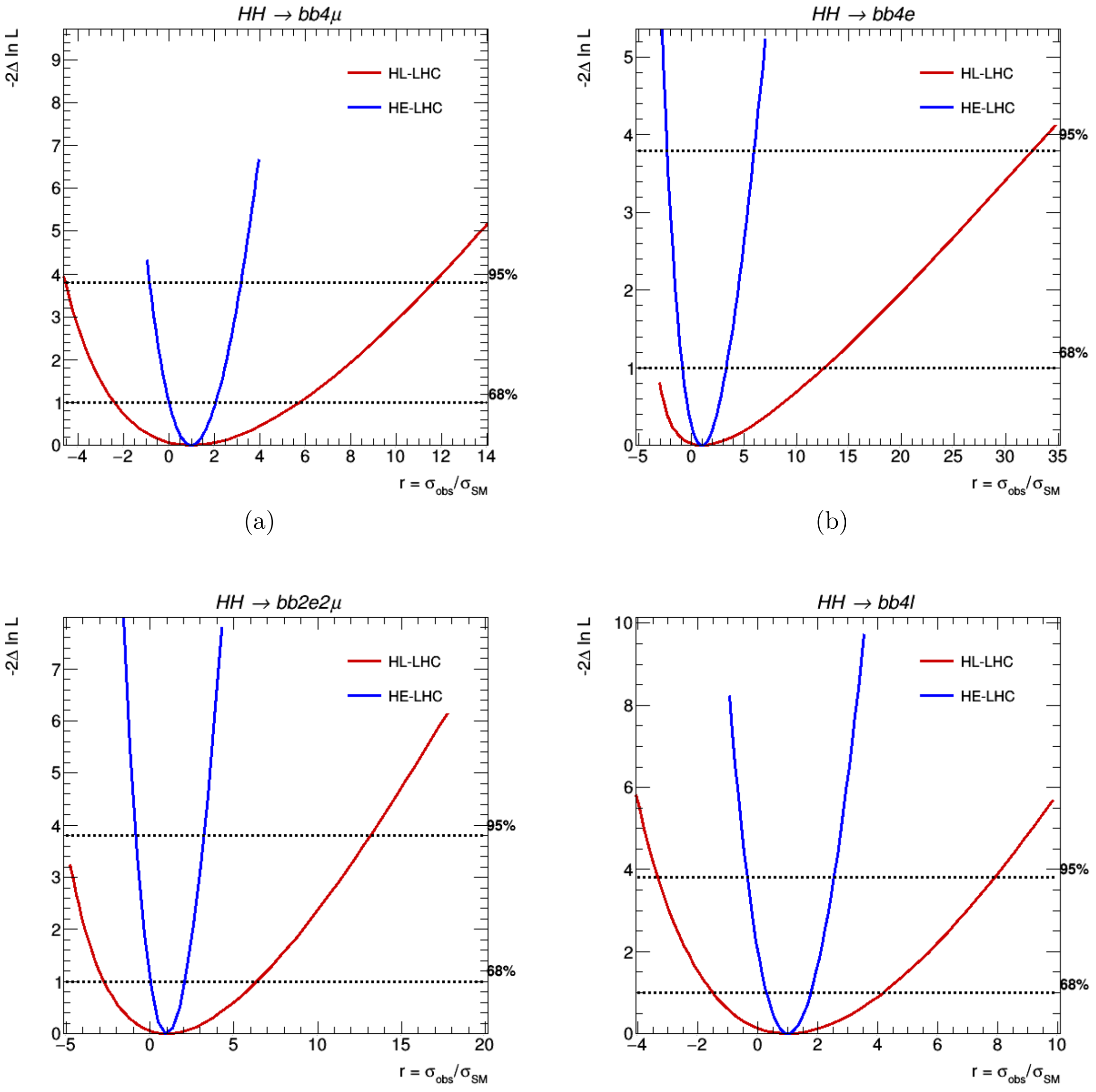

(a) (b)

(c) (d)

Figure 4.15: Expected likelihood scan as a function of the signal strength $r = \sigma_{\text{obs}}/\sigma_{\text{SM}}$ in the HE-LHC and the HL-LHC scenario for each final state: $b\bar{b}4\mu$ (a), $b\bar{b}4e$ (b), $b\bar{b}2e2\mu$ (c), $b\bar{b}4\ell$ (d).

A comparison with the results of the κ_λ study between the HE and the HL scenarios is also performed. As for the signal strength analysis, the study in the HE-LHC framework gives a tighter interval on κ_λ (the confidence intervals at the 68% and at the95% CL are reported in Table 4.11) with respect to the HL-LHC one (Figure 4.16).

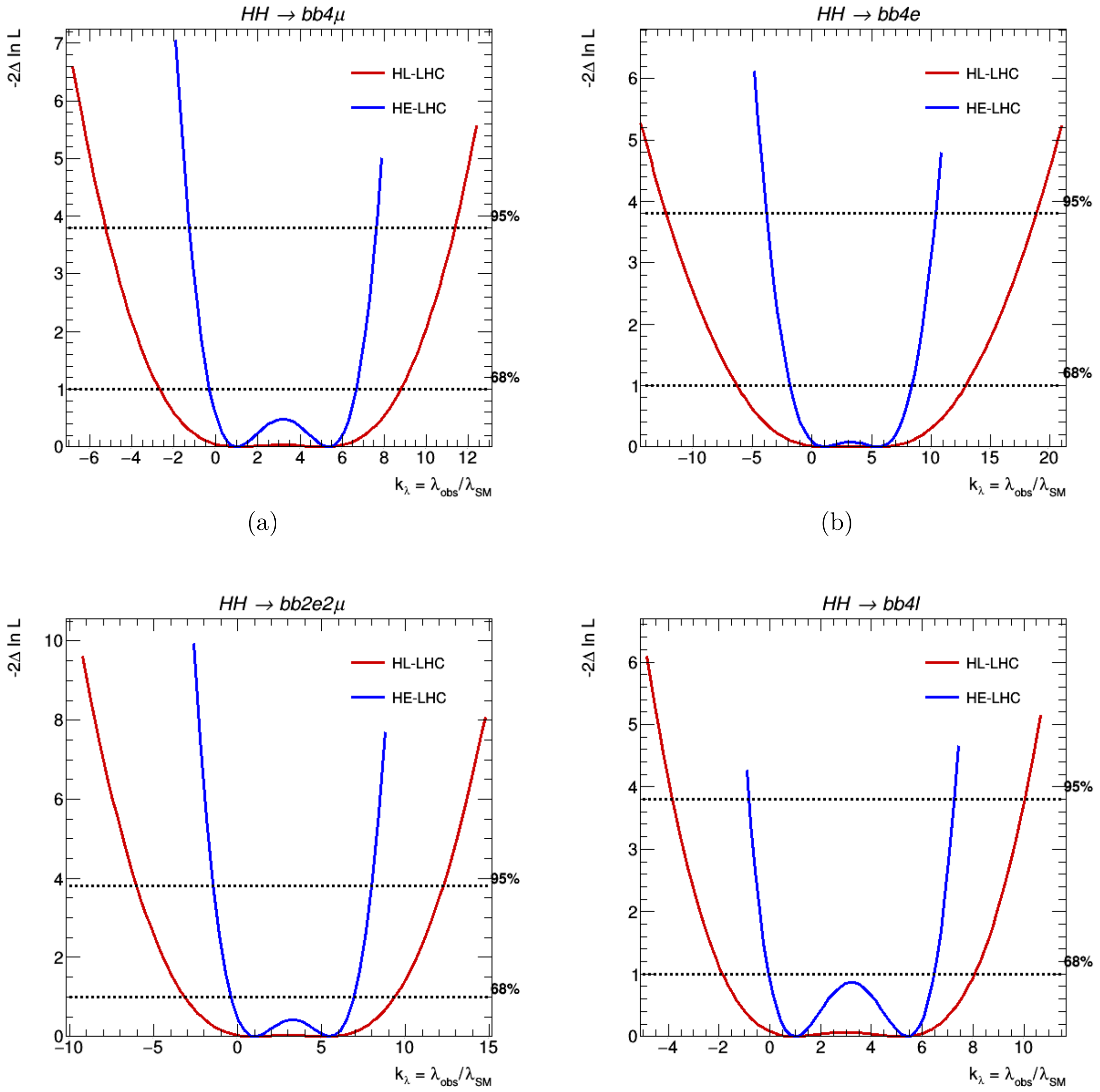

(a)

(b)

(c)

(d)

Figure 4.16: Expected likelihood scan as a function of the self-coupling modifier κ_λ for each final state: $b\bar{b}4\mu$ (a), $b\bar{b}4e$ (b), $b\bar{b}2e2\mu$ (c), $b\bar{b}4\ell$ (d).

	$b\bar{b}4\mu$	$b\bar{b}4e$	$b\bar{b}2e2\mu$	$b\bar{b}4\ell$
68% intervals on κ_λ at HL-LHC	$[-2.8, 8.8]$	$[-6.5, 13.3]$	$[-3.3, 9.3]$	$[-2.0, 8.0]$
68% intervals on κ_λ at HE-LHC	$[-0.3, 6.7]$	$[-2.0, 8.3]$	$[-0.4, 6.9]$	$[-0.1, 6.4]$
95% intervals on κ_λ at HL-LHC	$[-5.2, 11.2]$	$[-12.6, 18.6]$	$[-6.3, 12.3]$	$[-3.9, 9.9]$
95% intervals on κ_λ at HE-LHC	$[-1.3, 7.7]$	$[-3.9, 10.5]$	$[-1.5, 8.0]$	$[-0.7, 7.2]$

Table 4.11: Confidence intervals at 68% CL and 95% CL on the self-coupling modifier κ_λ in the HE-LHC and HL-LHC scenarios, considering both statistical and systematic uncertainties.

Conclusions

During the next decade a substantial upgrade is planned for the Large Hadron Collider (LHC) in order to achieve new experimental conditions to study the Standard Model (SM) predictions and to look for Beyond Standard Model (BSM) effects. The so-called High Luminosity LHC (HL-LHC) scenario is planned to start in 2026 to increase the instantaneous luminosity to $\mathcal{L} = 5 \times 10^{34}$ cm^{-2}s^{-1}. A possible future scenario, the High Energy LHC (HE-LHC) with increased center-of-mass energy from 14 to 27 TeV, is also under study and could follow the HL-LHC data-taking phase.

In order to cope with these challenging experimental conditions, the CMS detector will undergo a significant upgrade, referred to as Phase-I (during the long shutdown 2, LS2, ongoing until 2020) and as Phase-II (during the LS3, in 2024-2026).

In this thesis, the prospects for the measurement of the Higgs boson self-coupling in the HE-LHC scenario, considering the Phase-II CMS detector upgrade, is performed in the HH→ b$\bar{\text{b}}$ZZ(4ℓ) channel, where $\ell = e, \mu$. The results are compared to those obtained in the HL-LHC scenario in the same channel. The analysis is completely based on Monte Carlo simulations of the signal and the background samples: MadGraph5_aMC@NLO is used for event generation and Pythia8 for parton shower and hadronization. The CMS detector response is obtained in the parametrized framework provided by Delphes. In order to study the sensitivity of the HE-LHC scenario to the observation of BSM effects, signal samples with different values of self-coupling are also simulated.

From the obtained results, some conclusions are derived. No direct observation of a pair of Higgs boson is expected in the HE-LHC considering only the channel taken into account in this thesis. The most sensitive channel is $b\bar{b}4\mu$, as expected due to the better reconstruction performance of muons with respect to electrons. The best results are obtained with the inclusive $b\bar{b}4\ell$ final state, where the limit at the 95% CL on the signal strength is $r = 1.45$, with a signal significance of $1.43\,\sigma$. Moreover, better results are obtained with respect to the ones in the HL-LHC scenario, where the limit at the 95% CL on the signal strength is $r = 6.56$, with a signal significance of $0.37\,\sigma$.

Considering the prospects on the measurements of the trilinear coupling λ_3, the expected likelihood scan on the self-coupling modifier κ_λ is computed. In the inclusive $b\bar{b}4\ell$ channel, the projected confidence intervals on the couplings correspond to $[-0.1, 6.4]$ at the 68% CL and to $[-0.7, 7.2]$ at the 95% CL, which give tighter constraints on the κ_λ possible values with respect to the results obtained in the HL-LHC scenario ($[-2.0, 8.0]$ at the 68% CL and $[-3.9, 9.9]$ at the 95% CL).

References

[1] F. Halzen and A. D. Martin. *Quarks and Leptons. An introductory course in Modern Particle Physics.* John Wiley and Sons, 1984.

[2] S. Braibant, G. Giacomelli, and M. Spurio. *Particles and Fundamental Interactions. An introduction to Particle Physics.* Springer, 2012.

[3] D. H. Perkins. *Introduction to High Energy Physics.* 4th ed. Cambridge University Press, 2000.

[4] C. N. Yang and R. L. Mills. 'Conservation of Isotopic Spin and Isotopic Gauge Invariance'. In: *Phys. Rev.* 96 (1 1954), pp. 191–195. DOI: `10.1103/PhysRev.96.191`.

[5] S. L. Glashow. 'Partial Symmetries of Weak Interactions'. In: *Nucl. Phys.* 22 (1961), pp. 579–588. DOI: `10.1016/0029-5582(61)90469-2`.

[6] Y. Nambu. 'Quasi-Particles and Gauge Invariance in the Theory of Superconductivity'. In: *Phys. Rev.* 117 (3 1960), pp. 648–663. DOI: `10.1142/9789814578158_0004`.

[7] J. Goldstone. 'Field theories with « Superconductor » solutions'. In: *Il Nuovo Cimento* 19.1 (1961), pp. 154–164. DOI: `10.1007/BF02812722`.

[8] F. Englert and R. Brout. 'Broken Symmetry and the Mass of Gauge Vector Mesons'. In: *Phys. Rev. Lett.* 13 (1964).

[9] G. S. Guralnik, C. R. Hagen, and T. W. B. Kibble. 'Global Conservation Laws and Massless Particles'. In: *Phys. Rev. Lett.* 13 (1964). DOI: `10.1103/PhysRevLett.13.585`.

[10] P. W. Higgs. 'Broken symmetries, massless particles and gauge fields'. In: *Phys. Rev. Lett.* 12 (1964). DOI: `10.1016/0031-9163(64)91136-9`.

[11] G. S. Guralnik, C. R. Hagen, and T. W. B. Kibble. 'Global Conservation Laws and Massless Particles'. In: *Phys. Rev. Lett.* 13 (20 1964), pp. 585–587. DOI: `10.1103/PhysRevLett.13.585`.

[12] T. W. B. Kibble. 'Symmetry Breaking in Non-Abelian Gauge Theories'. In: *Phys. Rev.* 155 (5 1967), pp. 1554–1561. DOI: `10.1103/PhysRev.155.1554`.

[13] S. Weinberg. 'A Model of Leptons'. In: *Phys. Rev. Lett.* 19 (21 1967), pp. 1264–1266. DOI: `10.1103/PhysRevLett.19.1264`.

[14] A. Salam. 'Weak and Electromagnetic Interactions'. In: *Conf. Proc.* C680519 (1968), pp. 367–377.

[15] F. J. Hasert et al. 'Observation of neutrino-like interactions without muon or electron in the Gargamelle neutrino experiment'. In: *Physics Letters B* 46.1 (1973), pp. 138–140. DOI: `https://doi.org/10.1016/0370-2693(73)90499-1`.

[16] The UA1 Collaboration. 'Experimental observation of isolated large transverse energy electrons with associated missing energy at s=540 GeV'. In: *Physics Letters B* 122.1 (1983), pp. 103–116. DOI: `10.1016/0370-2693(83)91177-2`.

[17] The UA2 Collaboration. 'Observation of single isolated electrons of high transverse momentum in events with missing transverse energy at the CERN pp collider'. In: *Physics Letters B* 122.5 (1983), pp. 476–485. DOI: `10.1016/0370-2693(83)91605-2`.

[18] The UA1 Collaboration. 'Experimental observation of lepton pairs of invariant mass around 95 GeV/c2 at the CERN SPS collider'. In: *Physics Letters B* 126.5 (1983), pp. 398–410. DOI: `10.1016/0370-2693(83)90188-0`.

[19] *The Large Electron-Positron Collider.* URL: `https://home.cern/science/accelerators/large-electron-positron-collider`.

[20] *ATLAS experiment.* URL: `https://atlas.cern/`.

[21] *CMS experiment.* URL: `https://cms.cern/`.

[22] The ATLAS Collaboration. 'Observation of a new particle in the search for the Standard Model Higgs boson with the ATLAS detector at the LHC'. In: *Phys. Lett.* B716 (2012), pp. 1–29. DOI: `10.1016/j.physletb.2012.08.020`.

[23] The CMS Collaboration. 'Observation of a new boson at a mass of 125 GeV with the CMS experiment at the LHC'. In: *Phys. Lett.* B716 (2012), pp. 30–61. DOI: `https://doi.org/10.1016/j.physletb.2012.08.021`.

[24] S. M. Consonni. 'Higgs search at ATLAS'. In: *Proceedings, International School on High Energy Physics : Workshop on High Energy Physics in the near Future. (LISHEP 2013): Rio de Janeiro, Brazil, March 17-24, 2013.* 2013.

[25] *LHC Higgs Cross-Section Working Group.* URL: `https://twiki.cern.ch/twiki/bin/view/LHCPhysics/LHCHXSWGCrossSectionsFigures`.

[26] LEP Electroweak Working Group. 'Precision Electroweak Measurements and Constraints on the Standard Model'. In: (2010).

[27] R. Barate et al. 'Search for the standard model Higgs boson at LEP'. In: *Phys. Lett.* B565 (2003), pp. 61–75. DOI: `10.1016/S0370-2693(03)00614-2`.

[28] T. Aaltonen et al. 'Combination of Tevatron Searches for the Standard Model Higgs Boson in the W^+W^- Decay Mode'. In: *Phys. Rev. Lett.* 104 (6 2010), p. 061802. DOI: `10.1103/PhysRevLett.104.061802`.

[29] The D0 Collaboration. 'Combined search for the standard model Higgs boson decaying to a bb pair using the full CDF data set'. In: *Phys. Rev. Lett.* 109 (2012), p. 111802. DOI: `10.1103/PhysRevLett.109.121802`.

[30] T. Aaltonen et al. 'Evidence for a particle produced in association with weak bosons and decaying to a bottom-antibottom quark pair in Higgs boson searches at the Tevatron'. In: *Phys. Rev. Lett.* 109 (2012), p. 071804. DOI: `10.1103/PhysRevLett.109.071804`.

[31] The D0 Collaboration. 'Combined Search for the Standard Model Higgs Boson Decaying to $b\bar{b}$ Using the D0 Run II Data Set'. In: *Phys. Rev. Lett.* 109 (2012). DOI: `10.1103/PhysRevLett.109.121802`.

[32] The ATLAS collaboration. 'Measurement of Higgs boson properties in the diphootn decay channel with 36.1 fb $^{-1}$ pp collision data at the center-of-mass energy of 13 TeV with the ATLAS detector'. In: ATLAS-CONF-2017-045 (2017). DOI: `10.1103/PhysRevD.98.052005`.

[33] The CMS collaboration. 'Measurements of Higgs boson properties in the diphoton decay channel in proton-proton collisions at $\sqrt{s} = 13$ TeV'. In: *Journal of High Energy Physics* 2018.11 (2018), p. 185. DOI: `10.1007/JHEP11(2018)185`.

[34] The ATLAS collaboration. 'Measurement of inclusive and differential cross-sections in the $H \to ZZ \to 4l$ decay channel at 13 TeV with the ATLAS detector'. In: *5th Large Hadron Collider Physics Conference (LHCP 2017) Shanghai, China, May 15-20, 2017.* ATLAS-CONF-2017-032. CERN. Geneva: CERN, 2017.

[35] The CMS collaboration. 'Measurements of properties of the Higgs boson decaying into the four-lepton final state in pp collisions at $\sqrt{s} = 13$ TeV'. In: *Journal of High Energy Physics* 2017.11 (2017), p. 47. DOI: `10.1007/JHEP11(2017)047`.

[36] M. Tanabashi et al. 'Review of Particle Physics'. In: *Phys. Rev. D* 98 (3 2018).

[37] M. Cepeda et al. *Higgs Physics at the HL-LHC and HE-LHC.* Tech. rep. arXiv:1902.00134. CERN, 2018.

[38] W. D. Goldberger and M. B. Wise. 'Modulus Stabilization with Bulk Fields'. In: *Phys. Rev. Lett.* 83 (24 1999). DOI: `10.1103/PhysRevLett.83.4922`.

[39] H. Davoudiasl, J. L. Hewett, and T. G. Rizzo. 'Phenomenology of the Randall-Sundrum Gauge Hierarchy Model'. In: *Phys. Rev. Lett.* 84 (10 2000). DOI: `10.1103/PhysRevLett.84.2080`.

[40] D. O'Connell, M. J. Ramsey-Musolf, and M. B. Wise. 'Minimal extension of the standard model scalar sector'. In: *Phys. Rev. D* 75 (3 2007). DOI: `10.1103/PhysRevD.75.037701`.

[41] G. C. Branco et al. 'Theory and phenomenology of two-Higgs-doublet models'. In: *Physics Reports* 516.1 (2012). DOI: `https://doi.org/10.1016/j.physrep.2012.02.002`.

[42] J. Baglio et al. 'The measurement of the Higgs self-coupling at the LHC: theoretical status'. In: *Journal of High Energy Physics* 2013.4 (2013), p. 151. DOI: `10.1007/JHEP04(2013)151`.

[43] R. Gröber and M. Mühlleitner. 'Composite Higgs boson pair production at the LHC'. In: *Journal of High Energy Physics* 2011.6 (2011), p. 20. DOI: `10.1007/JHEP06(2011)020`.

[44] The CMS collaboration. 'Search for nonresonant Higgs boson pair production in the $b\bar{b}b\bar{b}$ final state at $\sqrt{s} = 13$ TeV'. In: *Journal of High Energy Physics* 2019.4 (2019), p. 112. DOI: `10.1007/JHEP04(2019)112`.

[45] O. S. Bruning et al. 'LHC Design Report Vol.1: The LHC Main Ring'. In: CERN Yellow Reports: Monographs (2004). DOI: `10.5170/CERN-2004-003-V-1`.

[46] O. S. Bruning et al. 'LHC Design Report. 2. The LHC infrastructure and general services'. In: CERN Yellow Reports: Monographs (2004). DOI: `10.5170/CERN-2004-003-V-2`.

[47] M. Benedikt et al. 'LHC Design Report. 3. The LHC injector chain'. In: CERN Yellow Reports: Monographs (2004). DOI: `10.5170/CERN-2004-003-V-3`.

[48] *CERN*. URL: `https://home.cern/`.

[49] *ALICE experiment*. URL: `http://alice.web.cern.ch/`.

[50] *LHCb experiment*. URL: `http://lhcb.web.cern.ch/lhcb/`.

[51] J. Haffner. 'The CERN accelerator complex. Complexe des accélérateurs du CERN'. In: (2013). General Photo. URL: `http://cds.cern.ch/record/1621894`.

[52] Apollinari G. et al. *High-Luminosity Large Hadron Collider (HL-LHC): Technical Design Report V. 0.1*. CERN Yellow Reports: Monographs. Geneva: CERN, 2017. DOI: `10.23731/CYRM-2017-004`.

[53] *The Long Shutdown 2 (LS2)*. URL: `https://indico.cern.ch/event/702149/contributions/2879714/attachments/1595391/2526647/LS2_Project_introduced_to_ILOs_v2018.0.pdf`.

[54] K. Hanke et al. 'The LHC Injectors Upgrade (LIU) Project at CERN: Proton Injector Chain'. In: *Proceedings, 8th International Particle Accelerator Conference (IPAC 2017): Copenhagen, Denmark, May 14-19, 2017*. 2017, WEPVA036.

[55] L. Arnaudon et al. *Linac4 Technical Design Report*. Tech. rep. CERN-AB-2006-084. Geneva: CERN, 2006.

[56] J.L. Abelleira et al. 'High-Energy LHC design'. In: *Journal of Physics: Conference Series* 1067 (2018). DOI: `10.1088/1742-6596/1067/2/022009`.

[57] *The physics potential of the HE-LHC*. URL: `https://twiki.cern.ch/twiki/pub/LHCPhysics/HLHELHCWorkshop/HEreport.pdf`.

[58] M. Benedikt and F. Zimmermann. 'FCC: Colliders at the Energy Frontier'. In: *Proceedings, 9th International Particle Accelerator Conference (IPAC 2018): Vancouver, BC Canada, April 29-May 4, 2018*. 2018, pp. 2908–2913.

[59] R. Kersevan. *Research program on the cryogenic beam-vacuum of the FCC-hh*. Chicago, 2016.

[60] H. Damerau et al. *LHC Injectors Upgrade, Technical Design Report, Vol. I: Protons*. Tech. rep. CERN-ACC-2014-0337. 2014.

[61] F. Burkart et al. *Conceptual design Considerations for a 1.3 TeV superconducting SPS (scSPS)*. Copenhagen, 2017.

[62] M. Benedikt and F. Zimmermann. 'Proton colliders at the energy frontier'. In: *Nucl. Instrum. Meth.* (2018), pp. 200–208. DOI: `10.1016/j.nima.2018.03.021`.

[63] G. Tonelli. *La nascita imperfetta delle cose*. Rizzoli, 2016.

[64] The CMS Collaboration. *CMS Physics: Technical Design Report Volume 1: Detector Performance and Software*. Tech. rep. CERN-LHCC-2006-001. Geneva, 2006.

[65] The CMS Collaboration. *CMS Physics: Technical Design Report Volume 2: Physics Performance*. Tech. rep. 2007. DOI: `10.1088/0954-3899/34/6/S01`.

[66] The CMS Collaboration. *CMS: letter of intent by the CMS Collaboration for a general purpose detector at LHC*. Tech. rep. CERN-LHCC-92-003. Geneva: CERN, 1992.

[67] M. Hoch and M. Brice. 'CMS experiment'. CMS Collection. 2008. URL: `https://cds.cern.ch/record/1474902`.

[68] The CMS Collaboration. *The CMS magnet project: Technical Design Report*. Tech. rep. CERN-LHCC-97-10. Geneva, 1997.

[69] The CMS Collaboration. *The CMS tracker system project: Technical Design Report*. Tech. rep. CERN-LHCC-98-006. Geneva, 1997.

[70] The CMS Collaboration. *The CMS electromagnetic calorimeter project: Technical Design Report*. Tech. rep. CERN-LHCC-97-033. Geneva, 1997.

[71] *Image of all ECAL*. 2008. URL: `http://cms-project-ecal-p5.web.cern.ch/cms-project-ECAL-P5/images/ecal_all.jpeg`.

[72] The CMS Collaboration. 'Identification and Filtering of Uncharacteristic Noise in the CMS Hadron Calorimeter'. In: *JINST* 5 (2010), T03014. DOI: `10.1088/1748-0221/5/03/t03014`.

[73] The CMS Collaboration. *The CMS hadron calorimeter project: Technical Design Report*. Tech. rep. CERN-LHCC-97-031. Geneva, 1997.

[74] The CMS Collaboration. *The CMS muon project: Technical Design Report*. Tech. rep. CERN-LHCC-97-032. Geneva, 1997.

[75] The CMS Collaboration. 'Performance of the CMS Drift-Tube Local Trigger with Cosmic Rays'. In: *JINST* 5 (2010), T03003. DOI: `10.1088/1748-0221/5/03/T03003`.

[76] *The CMS Resistive Plate Chambers (RPC) muon subsystem*. URL: `https://twiki.cern.ch/twiki/bin/view/CMS/RPComm`.

[77] The CMS Collaboration. *CMS. The TriDAS project. Technical design report, vol. 1: The trigger systems*. Tech. rep. CERN-LHCC-2000-038. 2000.

[78] The CMS Collaboration. *CMS: The TriDAS project. Technical design report, Vol. 2: Data acquisition and high-level trigger*. Tech. rep. CERN-LHCC-2002-026. 2002.

[79] The CMS Collaboration. *Technical proposal for the upgrade of the CMS detector through 2020*. Tech. rep. CERN-LHCC-2011-006. 2011.

[80] The CM Collaboration. *Technical Proposal for the Phase-II Upgrade of the CMS Detector*. Tech. rep. CERN-LHCC-2015-010. Geneva, 2015.

[81] F. Sauli. 'The gas electron multiplier (GEM): Operating principles and applications'. In: *Nucl. Instrum. Meth.* A805 (2016), pp. 2–24. DOI: `https://doi.org/10.1016/j.nima.2015.07.060`.

[82] Claudio Caputo. *Physics Studies for the CMS Muon System Upgrade with Triple-GEM detectors*. Tech. rep. CMS-CR-2014-355. 12. Geneva: CERN, 2014. DOI: `10.1088/1748-0221/9/12/C12035`.

[83] The CMS Collaboration. *The Phase-2 Upgrade of the CMS Tracker*. Tech. rep. CERN-LHCC-2017-009. Geneva: CERN, 2017.

[84] The CMS Collaboration. *The Phase-2 Upgrade of the CMS Tracker*. Tech. rep. CERN-LHCC-2017-009. Geneva: CERN, 2017.

[85] The CMS Collaboration. *The Phase-2 Upgrade of the CMS Muon Detectors*. Tech. rep. CERN-LHCC-2017-012. Geneva: CERN, 2017.

[86] The CMS Collaboration. *The Phase-2 Upgrade of the CMS Endcap Calorimeter*. Tech. rep. CERN-LHCC-2017-023. Geneva: CERN, 2017.

[87] A. M. Magnan. 'HGCAL: a High-Granularity Calorimeter for the endcaps of CMS at HL-LHC'. In: *Journal of Instrumentation* 12.01 (2017), pp. C01042–C01042. DOI: `10.1088/1748-0221/12/01/c01042`.

[88] A. Martelli. *The CMS HGCAL detector for HL-LHC upgrade. The CMS HGCAL detector for HL-LHC upgrade*. Tech. rep. arXiv:1708.08234. 2017.

[89] The CMS Collaboration. *The Phase-2 Upgrade of the CMS L1 Trigger Interim Technical Design Report*. Tech. rep. CERN-LHCC-2017-013. Geneva: CERN, 2017.

[90] The CMS Collaboration. *The Phase-2 Upgrade of the CMS DAQ Interim Technical Design Report*. Tech. rep. CERN-LHCC-2017-014. Geneva: CERN, 2017.

[91] J. Alwall et al. 'The automated computation of tree-level and next-to-leading order differential cross-sections, and their matching to parton shower simulations'. In: *Journal of High Energy Physics* 07 (2014), p. 079. DOI: `10.1007/JHEP07(2014)079`.

[92] T. Sjöstrand et al. 'An Introduction to PYTHIA 8.2'. In: *Comput. Phys. Commun.* 191 (2015), pp. 159–177. DOI: `10.1016/j.cpc.2015.01.024`.

[93] T. Stelzer and W. F. Long. 'Automatic generation of tree level helicity amplitudes'. In: *Comput. Phys. Commun.* 81 (1994), pp. 357–371. DOI: `10.1016/0010-4655(94)90084-1`.

[94] S. Frixione and B. R. Webber. 'Matching NLO QCD computations and parton shower simulations'. In: *JHEP* 06 (2002), p. 029. DOI: `10.1088/1126-6708/2002/06/029`.

[95] S. Agostinelli et al. 'GEANT4: A Simulation toolkit'. In: *Nucl. Instrum. Meth.* A506 (2003), pp. 250–303. DOI: `10.1016/S0168-9002(03)01368-8`.

[96] J. de Favereau et al. 'DELPHES 3, A modular framework for fast simulation of a generic collider experiment'. In: *Journal of High Energy Physics* 02 (2014), p. 057. DOI: `10.1007/JHEP02(2014)057`.

[97] S. Ovyn, X. Rouby, and V. Lemaitre. 'DELPHES, a framework for fast simulation of a generic collider experiment'. In: CP3-09-01 (2009).

[98] M. Cacciari, G. P. Salam, and G. Soyez. 'FastJet User Manual'. In: *Eur. Phys. J.* C72.CERN-PH-TH-2011-297 (2012), p. 1896.

[99] *Prospects on the tri-linear Higgs boson coupling with the Phase-2 upgraded CMS detector at the High-Luminosity LHC in the* $HH \rightarrow b\bar{b}ZZ(4l)$ *decay channel.* URL: `http://cms.cern.ch/iCMS/jsp/db_notes/noteInfo.jsp?cmsnoteid=CMS$%5C%$20AN-2018/229`.

[100] *SM Higgs production cross-sections at* $\sqrt{s}$ = 13, 14 *and* 27 *TeV.* URL: `https://twiki.cern.ch/twiki/bin/view/LHCPhysics/CERNHLHE2019`.

[101] *SM Higgs Branching Ratios and Total Decay Widths.* URL: `https://twiki.cern.ch/twiki/bin/view/LHCPhysics/CERNYellowReportPageBR`.

[102] *Baseline muon selections for Run-II.* URL: `https://twiki.cern.ch/twiki/bin/view/CMS/SWGuideMuonIdRun2`.

[103] D. Bertolini et al. 'Pileup per particle identification'. In: *Journal of High Energy Physics* 2014.10 (2014), p. 59. DOI: `10.1007/JHEP10(2014)059`.

[104] The CMS Collaboration. 'Performance of b tagging algorithms in proton-proton collisions at 13 TeV with Phase 1 CMS detector'. In: CMS-DP-2018-033 (2018).

[105] *Combine.* URL: `https://cms-analysis.github.io/HiggsAnalysis-CombinedLimit/`.

[106] *SM Higgs production cross-sections at* $\sqrt{s} = 13, 14$ *and 27 TeV.* URL: `https://twiki.cern.ch/twiki/bin/view/LHCPhysics/CERNHLHE2019`.

[107] *Recommendations for Systematic Uncertainties HL-LHC.* URL: `https://twiki.cern.ch/twiki/bin/view/LHCPhysics/HLHELHCCommonSystematics`.

[108] *Prospects for HH measurements at the HL-LHC.* Tech. rep. CMS-PAS-FTR-18-019. Geneva: CERN, 2018.